

AD-A146 206

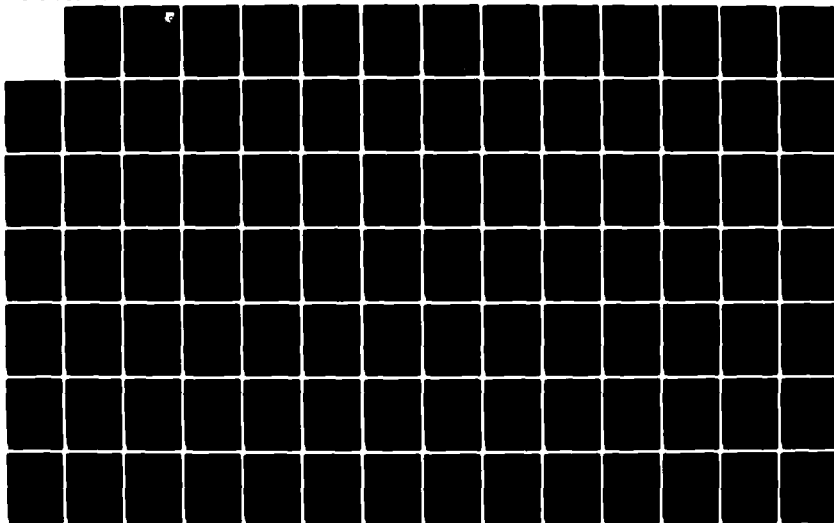
LASER VELOCIMETER MEASUREMENTS AND ANALYSIS IN
TURBULENT FLOWS WITH COMBU... (U) PURDUE UNIV LAFAYETTE
IN SCHOOL OF MECHANICAL ENGINEERING
H D THOMPSON ET AL. JUL 84

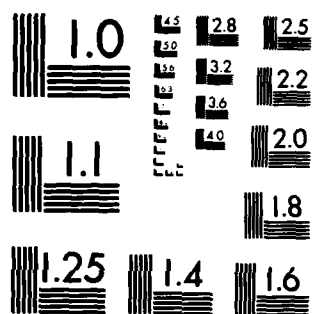
1/3

UNCLASSIFIED

F/G 20/5

NL





MICROCOPY RESOLUTION TEST CHART
NATIONAL BUREAU OF STANDARDS-1963-A

AD-A146 206

DTIC FILE COPY

AFWAL-TR-82-2076
Part III



LASER VELOCIMETER MEASUREMENTS AND ANALYSIS
IN TURBULENT FLOWS WITH COMBUSTION

Part III - A Correction Lens for Laser Doppler
Measurements in a Cylindrical Tube

H.D. THOMPSON
W.H. STEVENSON
R.P. DURRETT

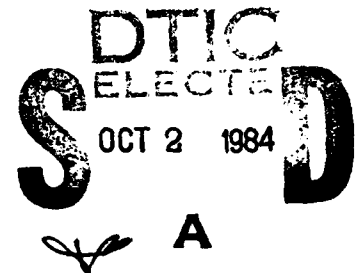
SCHOOL OF MECHANICAL ENGINEERING
PURDUE UNIVERSITY
WEST LAFAYETTE, INDIANA 47907

July 1984

Interim Report for Period January 1983 - December 1983

Approved for public release; distribution unlimited

AERO PROPULSION LABORATORY
AIR FORCE WRIGHT AERONAUTICAL LABORATORIES
AIR FORCE SYSTEMS COMMAND
WRIGHT-PATTERSON AIR FORCE BASE, OHIO 45433



84 09 25 008

NOTICE

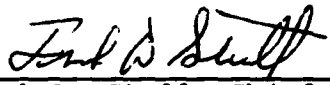
When Government drawings, specifications, or other data are used for any purpose other than in connection with a definitely related Government procurement operation, the United States Government thereby incurs no responsibility nor any obligation whatsoever; and the fact that the government may have formulated, furnished, or in any way supplied to the said drawings, specifications, or other data, is not to be regarded by implication or otherwise as in any manner licensing the holder or any other person or corporation, or conveying any rights or permission to manufacture, use, or sell any patented invention that may in any way be related thereto.

This report has been reviewed by the Office of Public Affairs (ASD/PA) and is releasable to the National Technical Information Service (NTIS). At NTIS, it will be available to the general public, including foreign nations.

This technical report has been reviewed and is approved for publication.

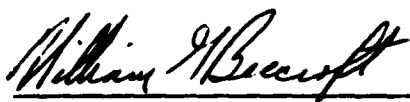


Roger R. Craig
Project Engineer



Frank D. Stull, Chief
Ramjet Technology Branch
Ramjet Engine Division

FOR THE COMMANDER



WILLIAM G. BEECROFT
Deputy Director, Ramjet Engine Division
Aero Propulsion Laboratory

If your address has changed, if you wish to be removed from our mailing list, or if the addressee is no longer employed by your organization please notify AFWAL/PORT, WPAFB, OH 45433 to help us maintain a current mailing list. Copies of this report should not be returned unless return is required by security considerations, contractual obligations, or notice on a specific document.

UNCLASSIFIED

SECURITY CLASSIFICATION OF THIS PAGE (When Data Entered)

| REPORT DOCUMENTATION PAGE | | READ INSTRUCTIONS BEFORE COMPLETING FORM |
|--|-----------------------------------|--|
| 1. REPORT NUMBER AFWAL-TR-82-2076 | 2. GOVT ACCESSION NO. Part III | 3. RECIPIENT'S CATALOG NUMBER AD-A146206 |
| 4. TITLE (and Subtitle) LASER VELOCIMETER MEASUREMENTS AND ANALYSIS IN TURBULENT FLOWS WITH COMBUSTION Part III - A Correction Lens for Laser Doppler Measurements in a Cylindrical Tube | | 5. TYPE OF REPORT & PERIOD COVERED Interim Report for Period Jan 83 - Dec 83 |
| 7. AUTHOR(s) H.D. Thompson, W.H. Stevenson, and R.P. Durrett | | 6. PERFORMING ORG. REPORT NUMBER |
| 9. PERFORMING ORGANIZATION NAME AND ADDRESS School of Mechanical Engineering Purdue University West Lafayette, Indiana 47907 | | 8. CONTRACT OR GRANT NUMBER(s) F33615-81-K-2003 |
| 11. CONTROLLING OFFICE NAME AND ADDRESS Aero Propulsion Laboratory (AFWAL/PORT) Air Force Wright Aeronautical Lab. (AFSC) Wright-Patterson Air Force Base, Ohio 45433 | | 10. PROGRAM ELEMENT, PROJECT, TASK AREA & WORK UNIT NUMBERS 2308-S1/07 |
| 14. MONITORING AGENCY NAME & ADDRESS (if different from Controlling Office) | | 12. REPORT DATE July 1984 |
| | | 13. NUMBER OF PAGES 216 |
| | | 15. SECURITY CLASS. (of this report) Unclassified |
| | | 15a. DECLASSIFICATION/DOWNGRADING SCHEDULE |
| 16. DISTRIBUTION STATEMENT (of this Report) Approved for public release; distribution unlimited | | |
| 17. DISTRIBUTION STATEMENT (of the abstract entered in Block 20, if different from Report) | | |
| 18. SUPPLEMENTARY NOTES | | |
| 19. KEY WORDS (Continue on reverse side if necessary and identify by block number) Turbulence measurements Laser velocimeter Bias errors (in laser velocimetry) Recirculating flows Numerical analysis Aberration correction | | |
| 20. ABSTRACT (Continue on reverse side if necessary and identify by block number) A lens was designed using analytical ray tracing techniques to correct aberrations caused by a cylindrical tube wall when measurements are made off the plane of symmetry with a Laser Doppler Velocimeter. The single element correction lens was found to work well and good results were obtained out to a normalized tube radius of $r/R = 0.83$. LDV measurements were made in three axisymmetric flow geometries: a turbulent flow in a straight pipe, a sudden expansion with diameter ratio 1.90:1, and a second sudden expansion with | | |

DD FORM 1 JAN 73 1473

EDITION OF 1 NOV 68 IS OBSOLETE
S/N 0102-014-6601

Unclassified

SECURITY CLASSIFICATION OF THIS PAGE (When Data Entered)

UNCLASSIFIED

SECURITY CLASSIFICATION OF THIS PAGE(When Data Entered)

diagram ratio 2.70:1. Mean velocity and turbulence intensity were measured as well as Reynolds stress and turbulence kinetic energy. Numerical predictions of the flow field using the k- ϵ turbulence model were compared to the experimental measurements in the 1.90:1 sudden expansion. In the 2.70:1 sudden expansion, the presence of a secondary recirculation zone in the corner of the step was confirmed and velocity measurements were made in this region.

Unclassified

SECURITY CLASSIFICATION OF THIS PAGE(When Data Entered)

FOREWORD

This interim technical report was submitted by the School of Mechanical Engineering of Purdue University under Contract No. F33615-81-K-2003 and covers the period 1 January 1983 - 31 December 1983. The research was sponsored by the Aero Propulsion Laboratory, Air Force Wright Aeronautical Laboratories, Wright-Patterson AFB, Ohio, under Project No. 2308 with Dr. Roger R. Craig AFWAL/PORT as Project Engineer. Warren H. Stevenson and H. Doyle Thompson of Purdue University were technically responsible for the work.

2
 INSPECTED
 DOPS
 2018

Available
 Distribution
 District
 Special

TABLE OF CONTENTS

| SECTION | PAGE |
|---|------|
| I. INTRODUCTION | 1 |
| II. LITERATURE REVIEW | 4 |
| 1. Introduction | 4 |
| 2. Axisymmetric Sudden Expansions | 4 |
| a. Past Experiments | 4 |
| b. The Sudden Expansion Flowfield | 5 |
| c. Comparison of Axisymmetric and 2-D Flows. | 10 |
| d. Reattachment Length. | 12 |
| e. Secondary Recirculation Zone | 16 |
| f. Numerical and Analytical Modeling. | 16 |
| 3. Correction of Optical Aberrations. | 20 |
| 4. LDV Measurement Accuracy | 21 |
| III. CORRECTION LENS | 25 |
| 1. Introduction | 25 |
| 2. Definition of the Problem. | 26 |
| 3. Lens Design. | 31 |
| 4. Experimental Verification. | 39 |
| IV. EXPERIMENTAL APPARATUS | 43 |
| 1. Introduction | 43 |
| 2. The Flow System. | 43 |
| 3. The LDV Optical System | 50 |
| 4. The Data Collection, Storage, and Processing System. | 54 |
| 5. The Seeding System | 56 |
| V. EXPERIMENTAL TECHNIQUE | 58 |
| 1. Introduction | 58 |
| 2. Flow System Parameters | 59 |
| 3. Optical System Parameters. | 65 |
| 4. Mean Velocity and Turbulence Parameter Measurements | 68 |
| 5. Wall Friction Velocity | 70 |
| 6. The Stream Function. | 73 |
| 7. The Mass Flow Rate | 74 |

PREVIOUS PAGE
IS BLANK

TABLE OF CONTENTS (concluded)

| SECTION | PAGE |
|--|------|
| VI. EXPERIMENTAL RESULTS | 75 |
| 1. Introduction | 75 |
| 2. Turbulent Pipe Flow Measurements | 75 |
| 3. Sudden Expansion Flowfield ($R_2/R_1 = 1.90$) | 83 |
| a. Mean Velocity Measurements | 83 |
| b. Turbulence Parameters | 102 |
| c. The Stream Function and Reattachment Length | 121 |
| d. Comparison of Numerical and Experimental Results | 123 |
| 4. Sudden Expansion Flowfield ($R_2/R_1 = 2.70$) | 127 |
| VII. CONCLUSIONS AND RECOMMENDATIONS | 140 |
| APPENDICES | 143 |
| Appendix A: Correction Lens Design Program | 144 |
| Appendix B: Correction Lens Fabrication | 160 |
| Appendix C: Uncertainty Analysis | 167 |
| Introduction | 167 |
| Random and Systematic Errors | 167 |
| Statistical Uncertainty | 169 |
| Flow System Uncertainty | 170 |
| LDV System Uncertainty | 171 |
| Uncertainty Due to Grouping of Data | 174 |
| Uncertainty in the Results | 177 |
| Appendix D: Experimental Data | 180 |
| LIST OF REFERENCES | 189 |

LIST OF ILLUSTRATIONS

| FIGURE | | PAGE |
|--------|--|------|
| 1 | Separated Flow Regions in an Axisymmetric Sudden Expansion | 7 |
| 2 | Non-Dimensionalization Parameters for Mixing Layer Region of Flow (from Ref. [23]) . . . | 19 |
| 3 | Beam Path for Axial Measurement | 27 |
| 4 | Beam Path for Radial Measurement | 28 |
| 5 | Schematic Diagram of Correction Lens Inserted in LDV System | 34 |
| 6 | Lens Position Required vs. Radial Location of Probe Volume | 36 |
| 7 | Optical Bench Setup Used to Test Correction Lenses | 41 |
| 8 | Flow System | 45 |
| 9 | Geometry of Test Section with 1.90:1 Nozzle . . | 47 |
| 10 | Geometry of Test Section with 2.70:1 Nozzle . . | 48 |
| 11 | LDV Optics Package | 51 |
| 12 | Experimental Measurement Grid for 1.90:1 Sudden Expansion | 62 |
| 13 | Experimental Measurement Grid for 2.70:1 Sudden Expansion | 64 |
| 14 | Static Pressure vs. Distance for the Turbulent Pipe Flow | 72 |
| 15 | Measured Axial Mean Velocity Profile in the Turbulent Pipe Flow | 78 |
| 16 | Measured Axial and Radial Turbulence Intensity Profiles in the Turbulent Pipe Flow | 80 |

LIST OF ILLUSTRATIONS (cont'd)

| FIGURE | | PAGE |
|--------|---|------|
| 17 | Measured Reynolds Stress Profile in the Turbulent Pipe Flow | 82 |
| 18 | Measured Axial Mean Velocity Profile at Inlet of 1.90:1 Sudden Expansion | 84 |
| 19 | Predicted and Measured Axial Mean Velocity Profile in the 1.90:1 Sudden Expansion at $x/H = 2$ | 86 |
| 20 | Predicted and Measured Axial Mean Velocity Profile in the 1.90:1 Sudden Expansion at $x/H = 4$ | 87 |
| 21 | Predicted and Measured Axial Mean Velocity Profile in the 1.90:1 Sudden Expansion at $x/H = 6$ | 88 |
| 22 | Predicted and Measured Axial Mean Velocity Profile in the 1.90:1 Sudden Expansion at $x/H = 8$ | 89 |
| 23 | Predicted and Measured Axial Mean Velocity Profile in the 1.90:1 Sudden Expansion at $x/H = 12$ | 90 |
| 24 | Predicted and Measured Axial Mean Velocity Profile in the 1.90:1 Sudden Expansion at $x/H = 20$ | 91 |
| 25 | Measured Mean Centerline Velocity Decay | 94 |
| 26 | Predicted and Measured Radial Mean Velocity Profile in the 1.90:1 Sudden Expansion at $x/H = 2$ | 96 |
| 27 | Predicted and Measured Radial Mean Velocity Profile in the 1.90:1 Sudden Expansion at $x/H = 4$ | 97 |
| 28 | Predicted and Measured Radial Mean Velocity Profile in the 1.90:1 Sudden Expansion at $x/H = 6$ | 98 |
| 29 | Predicted and Measured Radial Mean Velocity Profile in the 1.90:1 Sudden Expansion at $x/H = 8$ | 99 |

LIST OF ILLUSTRATIONS (cont'd)

| FIGURE | | PAGE |
|--------|--|------|
| 30 | Predicted and Measured Radial Mean Velocity Profile in the 1.90:1 Sudden Expansion at $x/H = 12$ | 100 |
| 31 | Predicted and Measured Radial Mean Velocity Profile in the 1.90:1 Sudden Expansion at $x/H = 20$ | 101 |
| 32 | Predicted and Measured Turbulence Kinetic Energy Profile in the 1.90:1 Sudden Expansion at $x/H = 2$ | 103 |
| 33 | Predicted and Measured Turbulence Kinetic Energy Profile in the 1.90:1 Sudden Expansion at $x/H = 4$ | 104 |
| 34 | Predicted and Measured Turbulence Kinetic Energy Profile in the 1.90:1 Sudden Expansion at $x/H = 6$ | 105 |
| 35 | Predicted and Measured Turbulence Kinetic Energy Profile in the 1.90:1 Sudden Expansion at $x/H = 8$ | 106 |
| 36 | Predicted and Measured Turbulence Kinetic Energy Profile in the 1.90:1 Sudden Expansion at $x/H = 12$ | 107 |
| 37 | Predicted and Measured Turbulence Kinetic Energy Profile in the 1.90:1 Sudden Expansion at $x/H = 20$ | 108 |
| 38 | Measured Axial and Radial Turbulence Intensity and Reynolds Stress in the 1.90:1 Sudden Expansion at $x/H = 2$ | 111 |
| 39 | Measured Axial and Radial Turbulence Intensity and Reynolds Stress in the 1.90:1 Sudden Expansion at $x/H = 4$ | 112 |
| 40 | Measured Axial and Radial Turbulence Intensity and Reynolds Stress in the 1.90:1 Sudden Expansion at $x/H = 6$ | 113 |
| 41 | Measured Axial and Radial Turbulence Intensity and Reynolds Stress in the 1.90:1 Sudden Expansion at $x/H = 8$ | 114 |

LIST OF ILLUSTRATIONS (concluded)

| FIGURE | | PAGE |
|--------|---|------|
| 42 | Measured Axial and Radial Turbulence Intensity and Reynolds Stress in the 1.90:1 Sudden Expansion at $x/H = 12$ | 115 |
| 43 | Measured Axial and Radial Turbulence Intensity and Reynolds Stress in the 1.90:1 Sudden Expansion at $x/H = 20$ | 116 |
| 44 | Normalized Stream Function Contours in the 1.90:1 Sudden Expansion | 122 |
| 45 | Axial Mean Velocity Profiles in the 1.90:1 Sudden Expansion Normalized with Similarity Parameter (from Ref. [23]) | 128 |
| 46 | Measured Axial Mean Velocity Profiles in the 2.70:1 Sudden Expansion | 129 |
| 47 | Measured Radial Mean Velocity Profiles in the 2.70:1 Sudden Expansion | 130 |
| 48 | Stream Function Contours in the 2.70:1 Sudden Expansion | 132 |
| 49 | Measured Axial Turbulence Intensity in the 2.70:1 Sudden Expansion | 134 |
| 50 | Measured Radial Turbulence Intensity in the 2.70:1 Sudden Expansion | 135 |
| 51 | Vorticity Contours in the 1.90:1 Sudden Expansion | 137 |
| 52 | Vorticity Contours in the 2.70:1 Sudden Expansion | 138 |
| A.1 | Ray Traces Performed by the Lens Design Program | 145 |
| B.1 | Cylindrical Lens Grinding and Polishing Mechanism | 162 |
| B.2 | Contour Plot for Concave Lens Surface Near the Vertex | 165 |

LIST OF TABLES

| TABLE | | PAGE |
|-------|--|------|
| 1 | Details of Previous Axisymmetric Sudden Expansion Investigations | 6 |
| 2 | Reattachment Length Results from Previous Investigations | 15 |
| 3 | Comparison of Probe Volumes With and Without the Correction Lens | 35 |
| 4 | Flow System Parameters | 60 |
| 5 | LDV System Parameter Settings | 66 |
| 6 | Integrated Mass Flux in the 1.90:1 Axisymmetric Sudden Expansion | 93 |
| D1 | Experimental Data from the Turbulent Pipe Flow | 181 |
| D2 | Experimental Data from the 1.90:1 Axisymmetric Sudden Expansion | 184 |
| D3 | Experimental Data from the 2.70:1 Axisymmetric Sudden Expansion | 187 |

SYMBOLS

| | |
|-----------|---|
| A_r | Area ratio |
| d | Thickness of lens at vertex |
| $d(x)$ | Width of potential core at x |
| D | Pipe diameter |
| D_1 | Inlet diameter of sudden expansion |
| D_m | Digital mantissa |
| f | Doppler frequency |
| f | Focal length |
| f_s | Net frequency shift |
| F_R | Fringe spacing |
| H | Step height |
| k | Turbulence kinetic energy |
| $k_{i,t}$ | Unit vector along incident and transmitted rays |
| $l_o(x)$ | Width of mixing layer region at x |
| \dot{m} | Mass flux |
| n | Number of samples |
| n | Exponent of TSI processor |
| n | Refractive index |
| N | Number of cycles/burst on TSI processor |
| P | Pressure |
| r | Radial coordinate direction |
| R | Pipe radius |
| $R_{1,2}$ | Inlet and outlet radius of sudden expansion |

SYMBOLS (cont'd)

| | |
|------------------------|--|
| $R_{1,2}$ | Radii of lens surfaces |
| Re | Reynolds number |
| u_i | Individual velocity realization |
| u_n | Unit vector normal to a surface at a point |
| u_τ | Wall friction velocity |
| u'_x, u'_r | Axial and radial velocity fluctuation |
| \bar{U}_x, \bar{U}_r | Axial and radial mean velocity |
| U_o | Reference velocity |
| $U_1(x)$ | Potential core velocity at x |
| x | Axial coordinate direction |
| x_r | Mean reattachment point |

Greek Symbols

| | |
|------------|--|
| α | Angle of rotation of probe volume |
| ϵ | Dissipation of turbulence kinetic energy |
| η | Similarity variable = $[r-d(x)]/l_o$ |
| θ | Angle between intersecting beams |
| θ | Tangential coordinate direction |
| λ | Laser light wavelength |
| ν | Fluid kinematic viscosity |
| ρ | Fluid density |
| σ | Standard deviation |
| τ_w | Wall shear stress |
| ψ | Stream function |
| ω | Measurement uncertainty |
| Ω | Vorticity |

SYMBOLS (concluded)

Math Symbols

Σ

Summation

$\frac{\partial}{\partial x}, \frac{\partial}{\partial r}$

Space derivatives

$\frac{\partial}{\partial t}$

Time derivative

SECTION I

INTRODUCTION

Sudden expansion flows are of interest in several different areas of engineering. They are perhaps the simplest kind of separating and reattaching flow because the separation point (or line) is fixed and the characteristics of the flow at separation can be easily controlled. This characteristic makes the sudden expansion flow a popular choice for analytical and numerical work when theories and models of turbulence are being tested. The sudden expansion flow is also important in direct engineering applications. The high turbulence levels in the shear layer which promote mixing, and the low velocities in the recirculation zone make this geometry useful as a flame holder for a dump combustor, for example.

It is generally accepted that in order to conduct a complete experimental study of a sudden expansion flowfield a Laser Doppler Velocimeter (LDV) is a necessary tool [1]*. The non-intrusive nature of the LDV along with its ability to measure highly turbulent flows and determine the direction of flow are desirable qualities. There are a few

* Numbers in brackets denote references listed in the List of References.

known that certain bias errors can exist, especially in highly turbulent flows [2], but if the nature of these bias errors is understood, measures can be taken to prevent or minimize their effect. Previous studies at this facility [2,3,4,5] have developed experimental techniques that have been proven to be useful in reducing LDV bias errors to an acceptable level.

The available literature contains many studies, both analytical and experimental, dealing with sudden expansion flows. The majority of these studies have dealt with 2-D flowfields because they are simpler for analytical and numerical work and are more easily accessible for experimental work. In particular, when an LDV is used to make measurements in an axisymmetric flowfield, the curved tube walls cause aberration problems which limit useful optical access to the flow. A primary objective of this study was to overcome this optical access problem through the use of a corrections lens mounted between the LDV optics and the tube wall.

Three different flow geometries were studied in this investigation. The first was a fully developed turbulent flow in a straight pipe. This flow was chosen first because it would provide a simple flowfield in which to verify the operation of the correction lens. The second flow, which comprised the main part of the experiment, was an axisymmetric sudden expansion with a diameter ratio of 1.90:1.

Axial and radial velocities and turbulence intensities were measured as well as Reynolds stresses and turbulence kinetic energy (TKE). The axial and radial mean velocities and TKE measurements were compared to numerical predictions by the code CHAMPION 2/E/FIX. The third study was done in a different axisymmetric sudden expansion, this time with a diameter ratio of 2.70:1. The purpose of this final study was to verify the existence of a weak secondary recirculation zone in the corner of the expansion and to obtain quantitative velocity measurements in this region.

SECTION II

LITERATURE REVIEW

1. INTRODUCTION

The general flow characteristics of the axisymmetric sudden expansion are of great engineering interest and have been the focus of many recent experimental and analytical investigations. This section presents a brief description of the characteristics of the axisymmetric sudden expansion flowfield and presents a review of the recent literature pertaining to these type flows. One of the main limitations of the axisymmetric sudden expansion experiments in the past has been the problem encountered in making LDV measurements through the curved duct walls. Some recent literature describing methods to account for refraction of the beams will be reviewed. Finally, a brief discussion of errors associated with LDV measurements will be presented.

2. AXISYMMETRIC SUDDEN EXPANSIONS

a. PAST EXPERIMENTS

Several studies, both experimental and computational, have been conducted to determine the effect of such parameters as inlet conditions, Reynolds number and step size on

shear layer characteristics in axisymmetric sudden expansion flows. Experimenters have used a variety of techniques to study such flows including flow visualization, hot-wire and hot film anemometry, and most recently, laser Doppler velocimetry. Air and water have both been used as working fluids with Reynolds numbers based on inlet diameter and average inlet velocity ranging from 10 to 10^7 . Both laminar and turbulent inlet flows have been investigated.

Table 1 gives a compilation of recent axisymmetric sudden expansion investigations. This is certainly not a complete list, but includes studies pertinent to this investigation. Another recent review of related problems in axisymmetric sudden expansions is given by Stevenson, et al. [5]. Reviews of two-dimensional step flow have been given by Bremmer, et al. [3], and by Eaton and Johnston [1].

b. THE SUDDEN EXPANSION FLOWFIELD

Although the sudden expansion is probably the simplest separating and reattaching flow, the flowfield is still quite complex as seen in Figure 1. The flowfield can be divided into two main regions: I) the separated mixing layer region and II) the reattached relaxation region.

The mixing layer region includes the flow from the point of separation at the step edge to the reattachment zone. This region may be further subdivided into five

Table 1. Details of Previous Axisymmetric Sudden Expansion Investigations.

| Year | Author(s) | Technique(s) | Fluid(s) | Inlet Velocity or Reynolds Number | Step Height or Area Ratio (h or A_R) |
|------|---------------------------------|--|----------|---|---|
| 1967 | Macagno and Hung [8] | numerical, aluminum powder visualization | oil | $36 \leq Re_{D_1} \leq 4500$ | $A_R = 2$ |
| 1972 | Back and Roschke [11] | dye studies | water | $20 \leq Re_{D_1} \leq 4500$ | $A_R = 2.6$ |
| 1975 | Freeman [14] | LDV (one-component) | water | $Re_{D_1} = 3 \times 10^4$ | $A_R = 2.1$ |
| 1977 | Gosman, Khali and Whitelaw [15] | numerical | air | $Re_{D_1} = 5 \times 10^4$ | $A_R = 2.6$ |
| 1977 | Moon and Rudinger [12] | numerical, LDV (one-component) | air | 40 - 90 mps | $A_R = 1.43$ |
| 1978 | Drewry [16] | pressure taps, gas-sampling, oil visualization | air | 450 - 1010 fps | $A_R = 1.28, 1.536, 1.92$ |
| 1979 | Kangovi and Page [13] | pressure taps, pitot tube, hot wire | air | $0.12 \leq M \leq 0.95$ | $h = 0.6, 1.3, 1.9, 2.5 \text{ cm}$ |
| 1982 | Stevenson, et al. [17] | numerical, LDV (one-component) | air | $Re_{D_1} = 4.1 \times 10^4$ | $A_R = 3.52$ |
| 1983 | Stevenson, et al. [5] | numerical, LDV (one-component) | air | $Re_h = 5.5 \times 10^4$ | $A_R = 4.0$ |

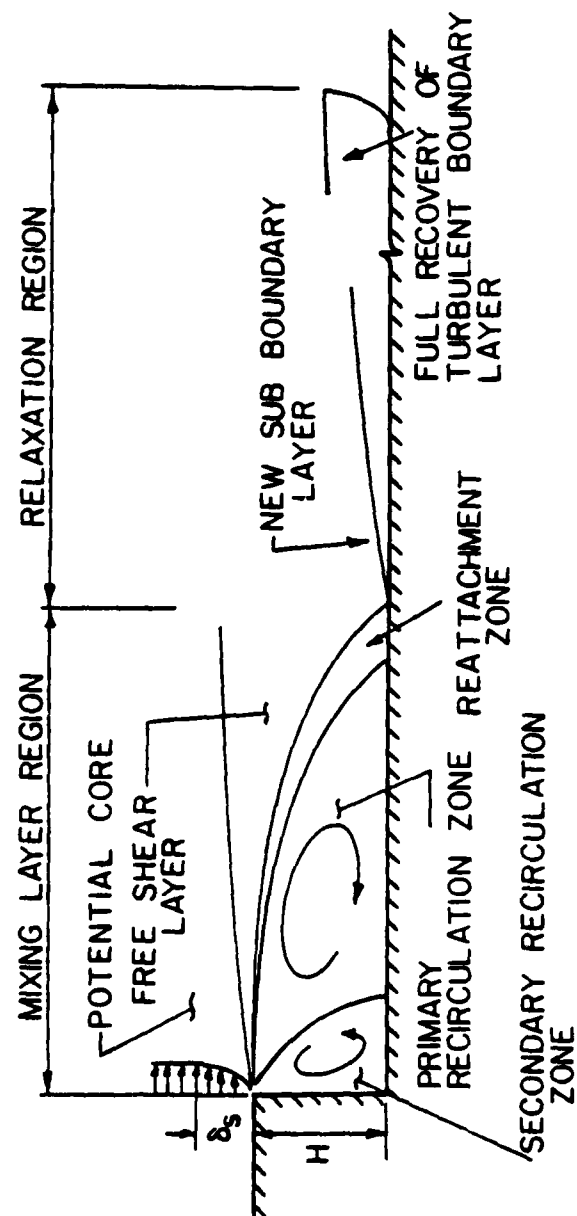


Figure 1. Separated Flow Regions in an Axisymmetric Sudden Expansion

smaller more distinct flow regions as follows:

1. A potential core region which continually diminishes in width in the downstream direction and is characterized by low turbulence levels and negligibly small cross stream gradients.
2. A free shear layer continually spreading downstream until wall interference occurs and characterized by large cross stream variations, high turbulence levels, and large intermittent eddies that promote mixing.
3. A primary recirculation zone of low negative velocities which transports fluid upstream.
4. A secondary recirculation zone, driven by the primary recirculation zone, that is confined to within one step height of the step.
5. The reattachment zone where bifurcation of the shear layer occurs.

Within the separated mixing layer region, the mean velocity gradient is nearly constant across the shear layer, similar to a free mixing layer. The location of the maximum turbulence energy coincides with the dividing streamline, i.e. the streamline that passes through the point of bifurcation at reattachment. As reattachment is approached, the location of maximum turbulent energy moves out away from the wall and remains there through reattachment and redevelopment of the boundary layer.

The reattached relaxation region begins at the reattachment zone and continues downstream until full recovery of the turbulent flow profile is achieved. Throughout this region, the inner part of the profile (the core) relaxes rather quickly while the outer part near the wall relaxes

more slowly. Bradshaw and Wong [6] pointed out that this slow return to equilibrium was probably a result of the turbulent length scales in the region being larger than those predicted by the local equilibrium form of the mixing length formula. Kim, Kline, and Johnston [7] add that this is understandable because part of the separated shear layer, which has longer mixing lengths than an attached boundary layer, comes very close to the wall as the flow proceeds through reattachment. Thus the turbulent length scales can be very large close to the wall resulting in longer relaxation times.

For an axisymmetric sudden expansion there is only a single annular separation region and axial symmetry in the flow would be expected. Any asymmetry in the flow would cause a local change in pressure distribution in the separation region which would be offset by a redistribution of pressure within this region leading to a symmetric flow-field. Macagno and Hung [8] showed that, for a flow with a laminar boundary layer at separation, symmetric flow patterns are maintained over a wide range of Reynolds numbers. Zemmanic and Dougall [9] did observe asymmetric flow patterns in a flow with a turbulent boundary layer at separation. The extent of the asymmetry was small, however, and this was the only reference found that noted any asymmetry in an axisymmetric sudden expansion flow.

c. COMPARISON OF AXISYMMETRIC AND 2-D FLOWS

Most of the work on separation and reattachment has been done with two-dimensional backward facing step flows. This test section geometry has been popular for several reasons. A two-dimensional step can be easily added to the floor of an existing wind tunnel; a two-dimensional flowfield is easier to model analytically or numerically; and, if an LDV is being used, there are fewer optical problems with the plane walls of a two-dimensional channel than with the curved walls of an axisymmetric duct.

For the purpose of this investigation, flow measurements in 2-D sudden expansions are important. The reason for this is that very few measurements of higher order turbulence parameters in axisymmetric expansions are in the existing literature. This lack is in some part due to the difficulty involved in making radial velocity measurements in a cylindrical geometry with an LDV. On the other hand, there are several 2-D sudden expansion studies for which cross stream velocity information and higher order turbulence correlations have been reported. Since the 2-D and axisymmetric flowfields share many characteristics, this cross stream information will be useful for comparison to axisymmetric expansion measurements.

The general features and structure of the two-dimensional and axisymmetric sudden expansion flowfields are

the same. All of the different flow regions that were described for the axisymmetric expansion are also present in 2-D flows. The main differences in the two flowfields come about due to the fact that for a given ratio of upstream duct height to downstream duct height, the area ratio for an axisymmetric expansion is larger than for a 2-D expansion. This larger area ratio indicates that the reattachment length may be longer due to the higher pressure gradient and the extent of the different flow regions will therefore be changed. These differences are minor though, and there is much to be gained by comparing 2-D and axisymmetric sudden expansion flow data.

A detailed review of 2-D sudden expansion flow research is given by Bremner, et al. [3]. Two other investigations of interest are those by Kim, Kline and Johnston [7] and by Driver and Seegmiller [10]. Eaton and Johnston [1] made a detailed review of existing literature for subsonic, turbulent studies in 2-D sudden expansions and selected the data of Kim, Kline and Johnston [7] to be among the best in existence at that time. Their selection was primarily based on the fact that the facility was well designed and the entire experiment was well documented. The test section had an inlet height of 7.62 cm, a step height of 3.81 cm and a width of 60.96 cm. Measurements were taken with a hot-wire anemometer, except for some mean velocity data which was obtained with a pitot probe. The data include measurements

of axial mean velocity, axial and cross-stream turbulence intensity and Reynolds stresses.

Driver and Seegmiller [10] performed an in depth investigation of 2-D step flow using a two-component LDV. Their test section had an inlet height of 10.1 cm, a 1.27 cm step height and a width of 15.1 cm. Measurements were made to a downstream distance of 32 step heights and included axial velocities, turbulent kinetic energies, Reynolds stresses and turbulent triple products. No bias corrections were made to the LDV data because the researchers concluded that the effect of bias was negligible. This data set was not available at the time of Eaton and Johnston's review.

d. REATTACHMENT LENGTH

The reattachment length is frequently used to characterize a sudden expansion flow. Reattachment length is defined as the axial distance between the point of separation (the step edge) and the mean reattachment point. The flow near reattachment is unsteady and the instantaneous reattachment point moves around within a range. Because of this unsteadiness, a reattachment "zone" is generally referred to in the literature rather than a reattachment point.

Back and Roschke [11] carried out an in depth study of reattachment length as a function of inlet Reynolds number.

Their results showed that the reattachment length varied significantly over the Reynolds number range that they studied ($20 < Re_{D_1} < 4500$). At $Re_{D_1} = 20$ the reattachment length was approximately two step heights and it increased steadily to a maximum value of approximately 25 step heights at $Re_{D_1} = 290$ where the inlet boundary layer was still laminar. For Reynolds numbers greater than 290, laminar instabilities became visible in the inlet boundary layer and the reattachment length decreased very rapidly to approximately seven step heights at $Re_{D_1} = 1000$. The reattachment length then slowly increased to a nearly constant value of about nine step heights for Reynolds numbers greater than 3000.

Moon and Rudinger [12] studied the reattachment length in a turbulent axisymmetric sudden expansion and found it to be between eight and nine step heights and practically independent of Reynolds number over the range 10^3 to 10^6 . They located the reattachment point by two means: 1) by interpolating mean velocity profiles obtained with an LDV at several axial locations and 2) by injecting a small amount of water into the duct upstream of the expansion and observing the water droplets on the wall downstream of the expansion to locate the stagnation point. Kangovi and Page [13] also used this water injection technique to confirm the location of a secondary stagnation point at about one step height downstream of the expansion.

The reattachment length findings of Back and Roschke and those of Moon and Rudinger as well as several others are summarized in Table 2. The results in this table show that the reattachment length for axisymmetric sudden expansions varies between 7 and 10 step heights for turbulent inlet flow conditions. Eaton, Johnston, and Jeans [18] commented on this discrepancy of reattachment length by suggesting that part of the variation may be the result of the recirculation zone slowly growing and shrinking. The entrainment rate balances the backflow rate only in the mean, not instantaneously. Limited observations suggest that these oscillations have a relatively low frequency, on the order of 50 Hz; however, this phenomenon has not been investigated in much detail.

Keuhn [19] observed that for 2-D sudden expansion data in the literature, there was a strong correlation between the observed reattachment length and the ratio of the channel height downstream of the expansion to the channel height upstream of the expansion. From this he postulated that the reattachment length variations may be due to variations in the pressure gradient. This was confirmed in a 2-D expansion in which the opposite wall could be varied to change the pressure gradient imposed on the flow field. Driver and Seegmiller [10] also showed that the pressure gradient exerted a large influence on the reattachment length in a 2-D sudden expansion.

Table 2. Reattachment Length Results from Previous Investigations.

| <u>Author(s)</u> | <u>Expansion Type</u> | <u>Techniques</u> | <u>Reattachment Length</u> |
|----------------------------|-----------------------|--|--|
| Back and Roschke [11] | axisymmetric | dye (flow visualization) | $x_r \approx 2$ @ $Re = 20$ steadily increases to $x_r \approx 25$ @ $Re = 290$ drops sharply to $x_r \approx 7$ @ $Re = 1000$ levels off at $x_r \approx 8-9$ @ $Re = 3000$ |
| Freeman [14] | axisymmetric | experimental stream function contours | $x_r \approx 8.7$ |
| Moon and Rudinger [12] | axisymmetric | experimental contours and flow visualization | $x_r \approx 8-9$ |
| Drewry [16] | axisymmetric | flow visualization | $x_r \approx 7.9-9.2$ |
| Kangovi and Page [13] | axisymmetric | flow visualization | $x_r \approx 8$ |
| Keuhn [19] | 2-D | experimental contours | $x_r = 5-20$ depending on pressure gradient |
| Stevenson, et al. [17] | axisymmetric | experimental stream function contours | $x_r \approx 7.9$ |
| Driver and Seegmiller [10] | 2-D | flow visualization | $x_r = 6-10$ depending on pressure gradient |
| Stevenson, et al. [5] | axisymmetric | experimental stream function contour | $x_r \approx 8.6$ |

e. SECONDARY RECIRCULATION ZONE

The existence of a secondary recirculation zone, or corner eddy, located within the first step height downstream from the sudden expansion has been theoretically predicted for sudden expansion flows. The secondary recirculation zone rotates in the opposite sense from the main recirculation zone and is driven by it.

The presence of such a secondary recirculation zone has been confirmed in a few studies. Kangovi and Page [13] used water injection and observed the behavior of the water film on the tube wall to determine the locations where the skin friction was zero. These zero skin friction locations correspond to the reattachment point and the point that separates the primary and secondary recirculation zones. Driver and Seegmiller [10] and de Brederode and Bradshaw [20] performed similar studies with an oil film on the wall of a 2-D expansion. All three studies showed the presence of a weak corner eddy within about one step height. No publications have been found that present actual velocity measurements in the secondary recirculation zone.

f. NUMERICAL AND ANALYTICAL MODELING

The understanding of sudden expansion flows has direct engineering applications as well as providing a basic flow situation that theories and models of turbulence may be

tested against. Most numerical and analytical models have been aimed at obtaining mean velocity and turbulence kinetic energy predictions throughout the flow field.

The most popular numerical prediction code in use today employs the two equation $k-\epsilon$ model originally developed by Harlow and Nakayama [21] and Launder, et al. [22]. Moon and Rudinger [12], and Stevenson, et al. [5,17] have used this turbulence model to predict the behavior of axisymmetric sudden expansion flows. The predictions developed in [17] were for the same experimental setup that is being used in the present investigation and these same predictions will be compared to data obtained in this study.

In the computer code using the two equation model, the two-dimensional, time averaged, conservation equations in elliptic form were solved using refined finite difference techniques. The two equation turbulence model employed requires "turbulence" coefficients which usually become "universal" based on experimental verification. Moon and Rudinger demonstrated that these coefficients were not universal, at least not for recirculating flows. Gosman, Khali, and Whitelaw [15] found that although the $k-\epsilon$ model was adequate for engineering purposes, it did not yield a precise representation of the flowfield. They felt that the dissipation (ϵ) equation caused at least part of the deficiency of the model. More complex models (Reynolds stress), however, apparently do not result in any better

representation of the flowfield [15]. It should be remembered that information is lost in time averaging the Navier-Stokes equations and the resulting equations are certain to be less than exact.

Lokrou and Shen [23] used a similarity analysis to try and describe the mixing layer region of a sudden expansion flowfield. The flow analysis was based on similarity arguments which assume a self preserving flow in the mixing layer region. The results give an average normalized profile that is invariant with respect to the axial location. The normalization was accomplished by using the width of the mixing layer, l_0 in Figure 2 as a length scale and by choosing a velocity scale proportional to the axial velocity in the potential core region, $U_1(x)$. The resulting similarity equation was solved analytically by linearizing the equation and also by numerical integration. Both a constant eddy viscosity model and a variable mixing length model were used. The constant eddy viscosity model gave better results for the axisymmetric case but the two models yielded similar results for a 2-D case. The predictions were in fairly good agreement with experimental results, considering the simplicity of the model. It should be noted that this similarity analysis only applies in the mixing layer region of the flow, i.e., it becomes invalid in the vicinity of a solid wall.

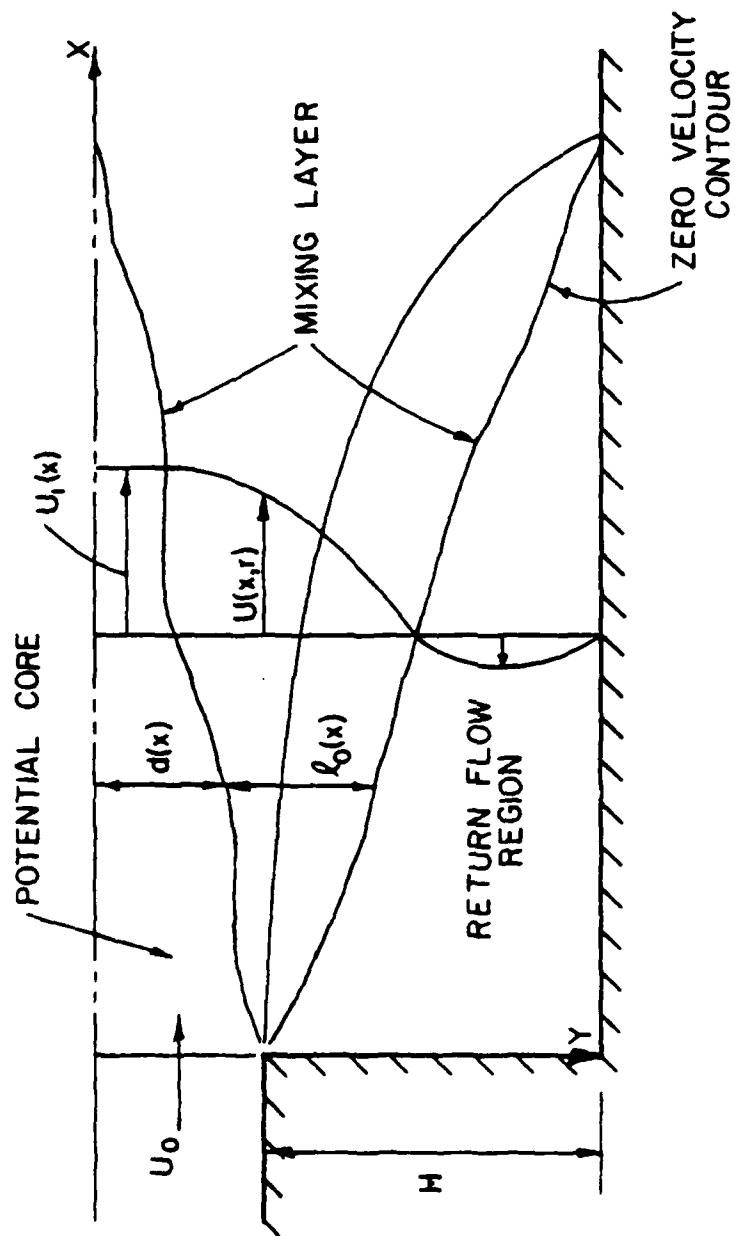


Figure 2. Non-Dimensionalization Parameters for Mixing Layer Region of Flow (from Ref. [23])

3. CORRECTION OF OPTICAL ABERRATIONS

Very little information can be found in the LDV literature concerning methods to correct or account for the optical aberration caused when laser beams pass through a curved duct wall. In past investigations, the problems associated with a curved duct were usually dealt with either by choosing a different flow geometry that used flat walls (such as a square duct) or by making measurements only on the axis of symmetry in a cylindrical duct [12,17]. Other remedies to the problem have been to drill small holes in the curved walls to allow the laser beams to pass untouched through the wall, to install flat windows in the curved wall and finally, to make the duct wall as thin as possible and neglect the effect of the refraction [12,24].

Equations have been derived to account for the effects of the refraction at the duct wall by Boadway and Karahan [25] and by Bicen [26]. Boadway and Karahan derived equations for the actual location of the probe volume for the three orientations that are required to measure the axial, tangential and radial velocity components. Axial velocity measurements are only considered in the plane parallel to the optical axis and containing the tube axis. The problems associated with making axial velocity measurements off this plane are not addressed. For the beam orientation necessary to measure the radial velocity component, they state that the position calculation is much more complex than for the

axial or tangential measurements, and the calculation is best done using a computer algorithm. Finally, Boadway and Karahan note that because of the refraction of the beams, the measured velocity contains a small component of the tangential velocity which must be accounted for.

Bicen [26] gives a more complete derivation of the equations required to determine the actual location of the probe volume and the actual half angle at the intersection. The equations obtained for the axial measurement in the plane of the optical axis and for the tangential measurement are the same as were derived in Boadway and Karahan. Bicen, however, also gives equations for the location and orientation of the probe volume for axial measurements in the plane perpendicular to the optical axis, and for the radial velocity measurement in this same plane. Unlike Boadway and Karahan, this paper states that the measured velocity when the beams are oriented to measure a radial velocity, is actually a radial velocity (or very close). The orientation of the probe volume is rotated and moved off of the vertical axis, but the bisector of the refracted beams is still at a right angle to a radius of the tube.

4. LDV MEASUREMENT ACCURACY

The LDV has many desirable qualities which make it a useful diagnostic tool in highly turbulent flows. Eaton and

Johnston [1] state that a frequency shifted LDV is necessary for a complete study including velocity, turbulence and shear stress measurements in a sudden expansion type flow. One of the advantages of an LDV system is that it requires no calibration. The final results are obtained through calculations involving quantities that are either known, such as the laser light wavelength, or that can be directly measured, such as beam intersection angle and Doppler frequency. Another advantage of the LDV, although not important in this investigation, is that extreme temperatures and contaminations in the flow do not affect the measurements as with hot-wires or pitot probes.

There are also disadvantages associated with an LDV system. The optical path to and from the probe volume must remain unobstructed and unchanged while measurements are being made. The finite size of the probe volume and the fact that the measured velocity is actually the velocity of a small seeding particle as opposed to the true gas velocity can present potential problems. Also, the requirements of statistical averaging of the data ensemble, especially in highly turbulent flow, may introduce errors into the measurements.

Several sources of error have been discovered which are inherent in LDV measurements. These errors or biases can result from particle seeding effects, probe volume effects, the data sampling method used and signal processor operating

characteristics. Several past studies at this facility [2,3,4,5] on the subject of LDV bias errors have shown that for the measurements of interest to this study, only two sources of bias error need to be considered; incomplete signal bias and velocity bias. As shown in [2] incomplete signal bias is easily eliminated by appropriate frequency shifting.

Velocity bias error is slightly more complex and difficult to correct. McLaughlin and Tiederman [27] first proposed in 1973 that measurements with an individual realization LDV would contain a bias commonly referred to as velocity or sampling bias. This bias is present due to the fact that if the average number of seed particles per unit volume is constant, then the average number of realizations acquired in a small time will be proportional to the magnitude of the velocity vector during that time. Because of this, the probability density distribution of the individual realizations will be biased and the mean velocity and turbulence intensity calculated from an ensemble of samples will not represent the characteristics of the flow. Several analytical studies have proposed correction schemes for velocity bias. A more detailed description is given by Stevenson, et al. [5]. These analytical correction schemes have met with limited success.

Stevenson, et al. [5] and Bremmer, et al. [3] have shown that velocity bias can be reduced to insignificant

levels by seeding the flow heavily and sampling data at a relatively slow rate. This technique was demonstrated by Roesler, et al. and a complete description of the technique is given in [2]. These investigations have shown that if the flow is seeded such that the LDV processor has a free running data rate¹ of at least 20,000 validated realizations per second and data is sampled at 50 Hz, velocity bias can be eliminated. Another advantage of sampling data at 50 Hz for this study is that the time required to collect a 4500 point ensemble (90 seconds) is long enough to satisfy the criteria set forth by Eaton and Johnston [1] stating that the sampling duration should be at least 2000-5000 through flow times² in order to insure measuring over all the large time scales.

1. Data rate is defined as the rate at which the LDV processor validates velocity realizations with no external restraint on the processor. When data is sampled, the computer limits the processor to a sampling rate prescribed by the computer.

2. Through flow time = reattachment length/inlet velocity

SECTION III

CORRECTION LENS

1. INTRODUCTION

When a laser velocimeter is used to make velocity measurements in cylindrical tubes, severe optical aberrations caused by the tube wall curvature can be present. When the optical axis of the LDV does not coincide with a diametral plane of the tube, these aberrations result in a distortion and enlargement of the probe volume and a shift in its position and orientation.

Equations have been derived [25,26] to find the actual location of the LDV probe volume and its angular orientation for different situations. These are of limited practical usefulness, however, for several reasons. In the case of a one component LDV operating in the forward scatter mode, the receiving optics will require major realignment for each change of measurement location. Additionally the probe volume image at the pinhole may be distorted. For a two component system the situation will be even worse, because the two probe volumes may be spatially separated.

The problems described may be attacked in two ways. One method is for the incoming laser beams and the detection

optics to be realigned for each different system position. This realignment however, will require adjustments that may not be possible on most LDV systems. Furthermore, this does not solve the problem of signal degradation due to distortion of the probe volume image on the pinhole. The other approach is to use some type of correction element to compensate for the optical effects caused by the tube. This element must reduce to an acceptable level the effects described so that reliable measurements can be made.

2. DEFINITION OF THE PROBLEM

The common LDV input beam geometries used to measure axial and radial velocities in a circular duct are shown in Figures 3 and 4. These two measurements may be made simultaneously if a two component LDV is used, or one at a time with a one component system. The beam geometries shown are applicable to a four beam, two component system. For a three beam two component system, one of the beams will be used for both components, but similar problems will be encountered with alignment. Measurements off the horizontal diametral plane (x axis in Figures 3 and 4) require some type of correction for the aberrations introduced by the curved duct wall. (Aberrations still exist when measurements are made on the horizontal diametral plane, but these are usually of less significance due to the symmetry involved.)

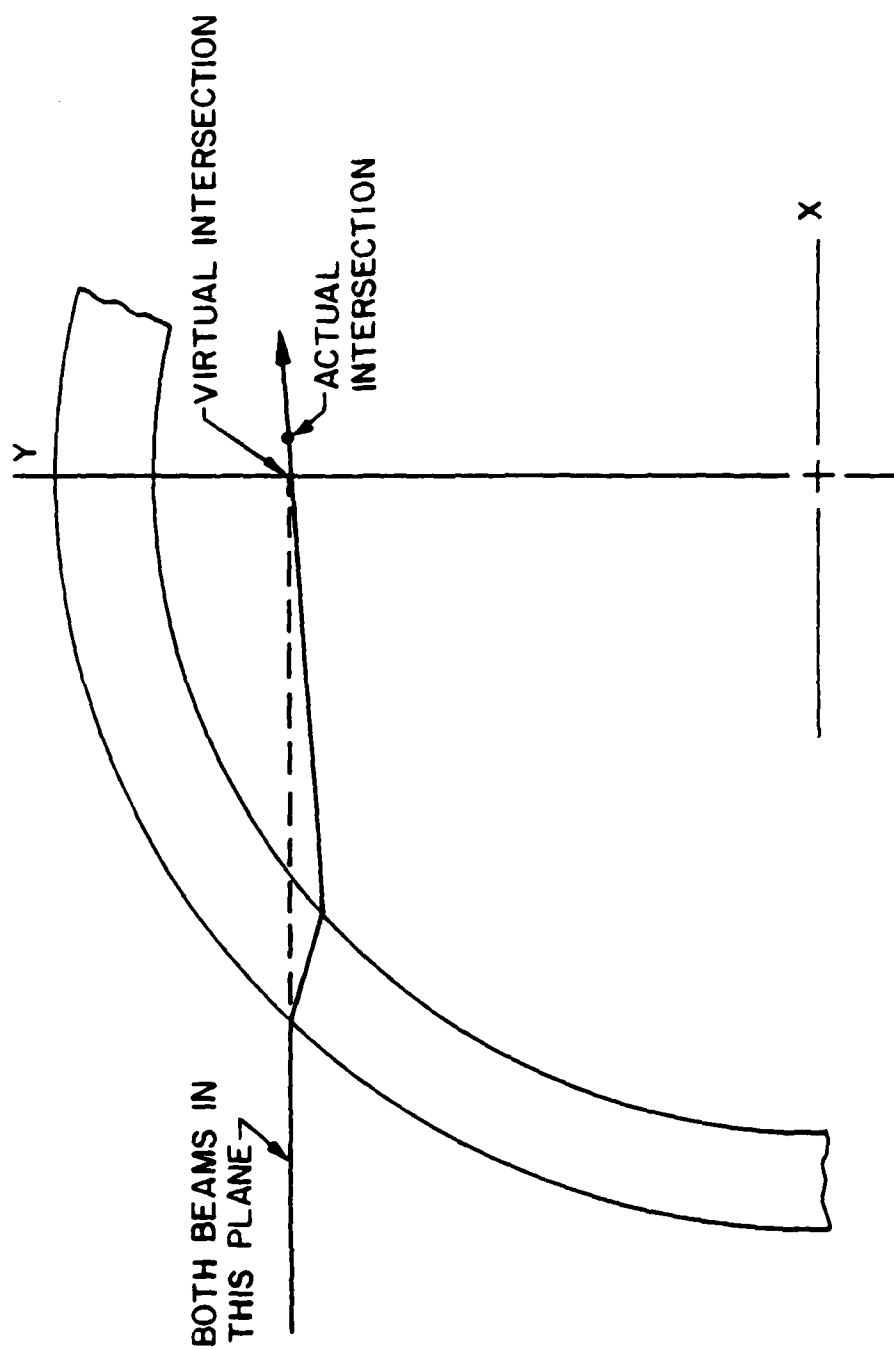


Figure 3. Beam Path for Axial Measurement

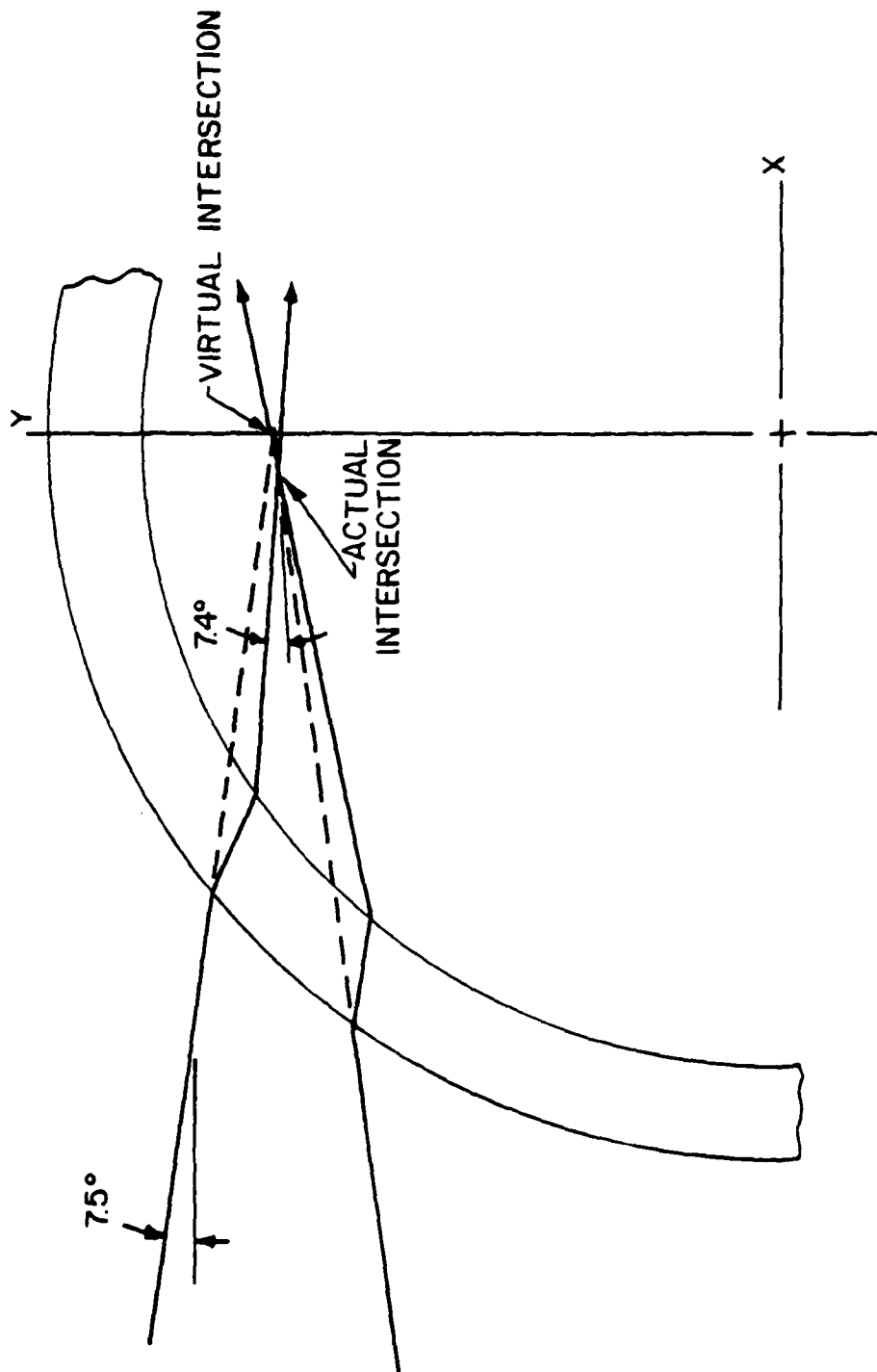


Figure 4. Beam Path for Radial Measurement

Figure 3 illustrates the beam paths when one attempts to measure the axial velocity component (normal to the figure) at a dimensionless radius of $r/R = 0.8$. In this example an acrylic plastic tube ($n = 1.49$) with a wall thickness 15% of the inside radius and air as the medium on both sides of the tube is shown. The incoming beams are aligned so that the virtual intersection point is on the vertical (y) axis and the beam intersection half-angle is 7.5 degrees. For this case, the probe volume is displaced so that the actual measurement point is as shown. The probe volume is also rotated about the axial direction, but a true axial component is still being measured. When forward scatter receiving optics are used, a cumbersome adjustment of both the transmitting and receiving optics is required for each consecutive measurement point on the y axis.

The beam paths for a radial velocity measurement at the same point are shown in Figure 4. In this case, the probe volume is more severely displaced, also the beam intersection angle is altered, the beam intersection is on the opposite side of the y axis from that of Figure 3, and the orientation of the probe volume is changed due to the angular rotation of the beam bisector. Probe volume orientation is here defined by the normal to the fringe planes in the probe volume which will also be perpendicular to the bisector of the intersecting beams. In this case the combined rotation and translation of the probe volume mean that a

true radial component is not measured, but the two effects tend to counteract each other and the error would be small unless a significant tangential velocity existed. Obviously, however, it would not be possible to measure correlated axial and radial components simultaneously with a four beam system, since the probe volumes for the two components would be separated in the x direction by a substantial amount.

When measuring either an axial or a radial component, these are the only significant effects as far as the input beams are concerned. However, if the input beams lie in some other plane, the possibility also exists that they will no longer cross or, if they do, that they may be oriented at some different angle. Measurements at other beam orientation angles are sometimes necessary to determine higher order quantities such as turbulent shear stress and turbulence kinetic energy. For example, with the input beam plane at 45 degrees with respect to the tube axis in the above system, the beams fail to cross. At their closest point, the beams are separated by a distance that is much larger than the beam diameter.

When the receiving optics are considered the situation is somewhat different. The function of the receiving optics is to collect light scattered from particles in the probe volume and focus this light within the aperture (pinhole) in front of the detector. Essentially this is the classical

problem of imaging a point source, complicated in the present case by the presence of the curved tube wall in the optical path. From the standpoint of geometrical optics the problem is one of bringing to intersection within an acceptably small region all light rays leaving the particle which fall within the aperture of the receiving lens. This is not a trivial problem, particularly when the axis of the receiving optics does not coincide with the tube axis and in fact must move with respect to the tube axis to permit the desired measurements.

3. LENS DESIGN

The most important design criterion for the correction lens is that the beam intersections must be very near the same location for all input beam orientations relative to the tube axis. The different beam orientations would be due to a rotation of the beams in a one component system or the two different beam pairs present in a two component system. The location of the probe volume is of secondary importance as long as it remains stationary with beam plane rotation. The actual location can be easily calculated.

The concept of analytical ray tracing, the method used in the design of the lens, is straightforward. An incoming ray is directed at the first surface of the optical system and the ray intersection point at the surface is calculated.

The refraction equation:

$$n_i [k_i \times u_n] = n_t [k_t \times u_n] \quad (1)$$

is then applied to determine the new direction of the transmitted ray. The intersection of the transmitted ray and the second surface is then calculated and the refraction equation applied again. This process is repeated as necessary. After all appropriate rays have been traced through the system the point at which the rays intersect can be calculated. In the case of the input beams this involves finding the intersection of pairs of rays lying in planes at various angles to the tube axis which represent the different input beam pairs required to measure different velocity components. The optimum correction lens design is the one which causes all of these ray pairs to intersect within desired tolerances. A more detailed description of the computer code used for the ray trace is given in Appendix A.

The tolerances chosen were that the beam intersection point remain stationary within ± 0.1 mm in the direction along the bisector of the two beams and within ± 0.025 mm in a direction perpendicular to that axis. These tolerances are approximately 10 percent of the corresponding dimensions of a typical LDV probe volume. Several workable lens types were found which used various combinations of cylindrical

and planar surfaces. The lens design finally selected was a cylindrical planar-concave configuration. A radius of curvature of 1195 mm (47 in) on the concave surface was determined to be optimum for the 101.6 mm (4 in) O.D., 3.2 mm (1/8 in) wall acrylic tube used in the present study. This lens satisfied the design requirements out to a non-dimensional radius of $r/R = 0.8$. At larger r/R values, the angle between the incoming beams and the tube wall is very shallow and the aberrations caused by the tube are much harder to correct. A schematic diagram of the LDV system with the correction lenses is shown in Figure 5.

Table 3 illustrates computed values for important probe volume parameters with and without the correction lens present. In both cases the beam intersection point for the axial component measurement was on the tube centerline at $r/R = 0$. At increasing values of r/R the coordinates of the actual beam intersection are as shown when the LDV optics are traversed in the y direction. In order to meet the design tolerances it was necessary to adjust the correction lenses when the measurement point was moved to a different y location. The relationship between the probe volume position and the lens position is given in Figure 6. The probe volume in this case is formed at points within ± 0.75 mm (0.03 in) of the vertical diametral line. The two lenses are moved simultaneously and are always symmetrically placed relative to the tube. A lens design which did not require

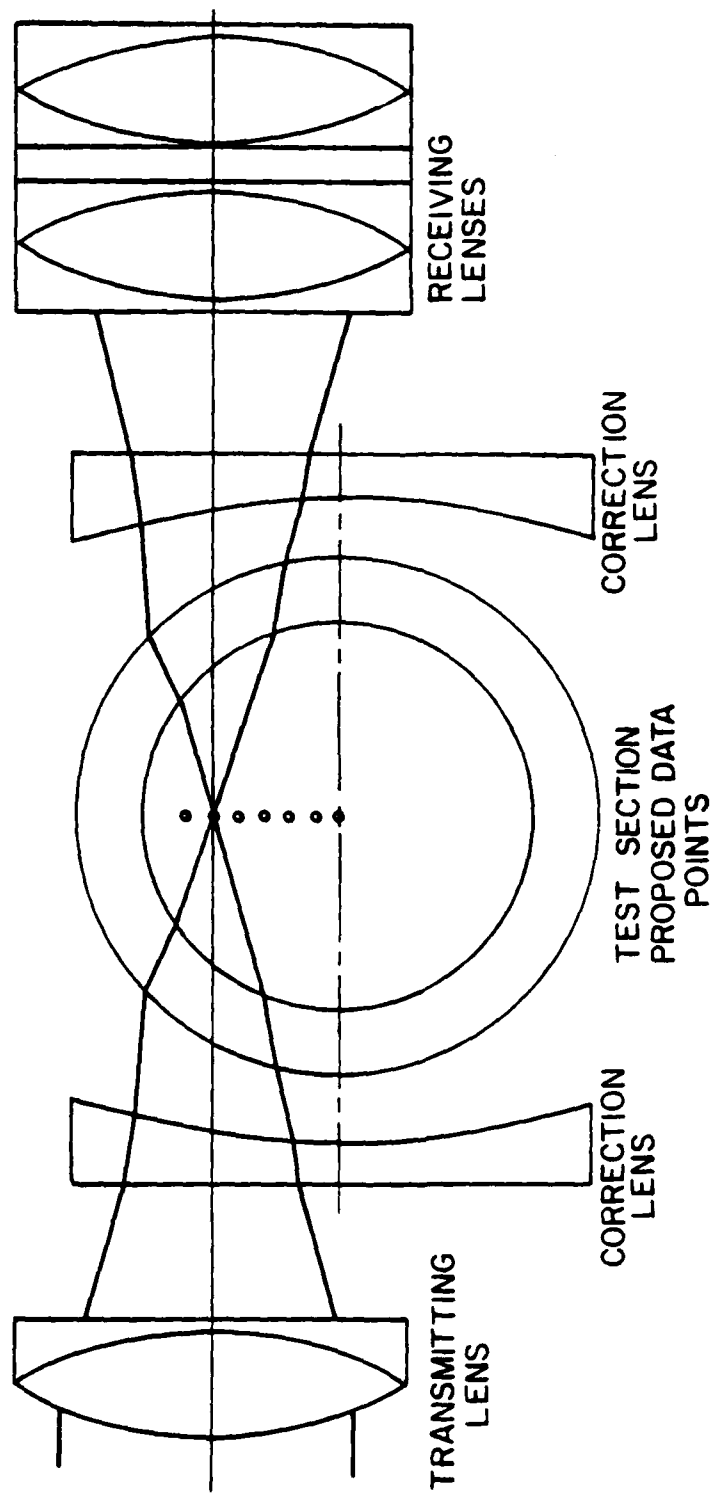


Figure 5. Schematic Diagram of Correction Lens
Inserted in LDV System

Table 3. Comparison of Probe Volumes With and Without the Correction Lens

| | $r = 13 \text{ mm}$ $r/R = 0.27$ | | $r = 26 \text{ mm}$ $r/R = 0.55$ | | $r = 38 \text{ mm}$ $r/R = 0.80$ | | |
|--|-------------------------------------|--------------|-------------------------------------|--------------|-------------------------------------|--------------|-------|
| | without lens | with lens | without lens | with lens | without lens | with lens | |
| Location of Probe Volume for Axial Measurement | X(mm) | 0.01 | 0.03 | 0.05 | 0.15 | 0.11 | 0.32 |
| | Y(mm) | 13.00 | 13.28 | 26.00 | 26.67 | 38.03 | 39.40 |
| Location of Probe Volume for Radial Measurement | X(mm) | -1.13 | 0.02 | -1.46 | 0.13 | -2.54 | 0.29 |
| | Y(mm) | 12.99 | 13.29 | 25.98 | 26.68 | 37.93 | 39.41 |
| Actual Half Angle for Radial Measurement (deg) | | 3.49 | 3.41 | 3.49 | 3.40 | 3.50 | 3.46 |
| Probe Volume Orientation (deg) | | 0.35 | 0.66 | 0.90 | 1.56 | 2.26 | 3.47 |

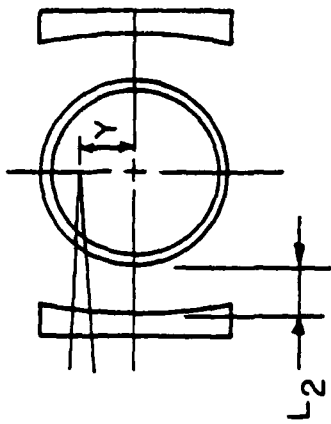
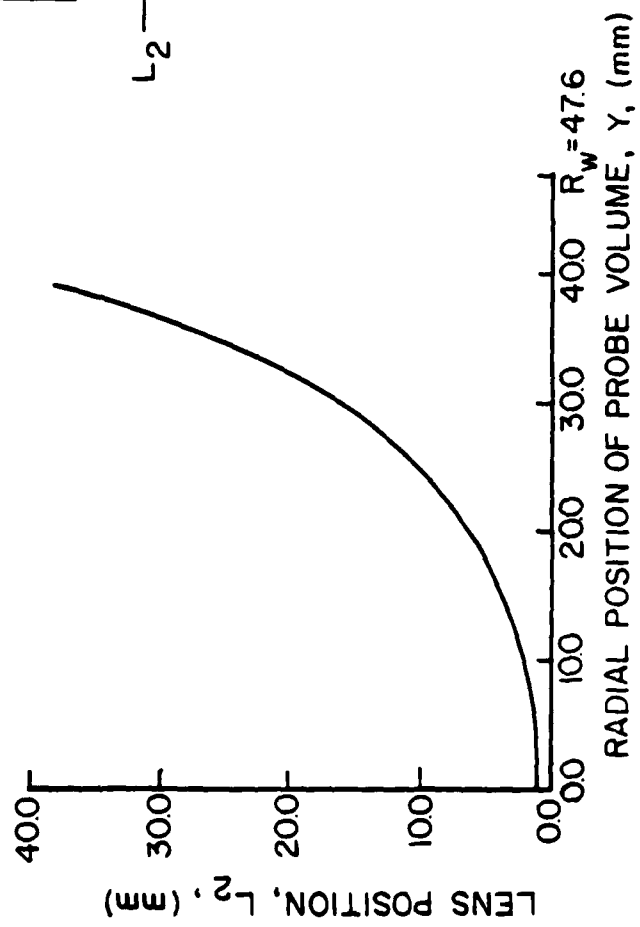


Figure 6. Lens Position Required vs. Radial Location of Probe Volume

this change in lens position was found to be impractical. Note that the probe volumes for the axial and radial measurements coincide within 0.001 inch (0.025 mm) when the correction lens is present. The beam intersection angle for the radial measurements does change somewhat, but this is easily accounted for in the data reduction.

The lens does not correct for the rotation of the probe volume about the axial direction due to the slight angular deviation of the beam bisector which occurs when the probe volume is above or below the tube axis. In fact this affect is larger when the correction lens is used. As mentioned before, this rotation causes no errors in measurements made in the axial direction, but for measurements in the radial direction a small component of any tangential flow will be introduced. In most cases this will cause no problems, but in a flow where a large swirl relative to the radial velocity is present this effect could cause large errors in the radial velocity measurements.

Design of the correction lens for the receiving optics side of the system can be simplified by limiting measurements to the vertical diameter of the tube (the y axis in Figure 3). If a correction lens identical to that on the input beam side is symmetrically placed on the receiving optics side of the tube, then light rays in a cone defined by the input beam and originating at the input beam intersection "point" can be collected and focused to a common

intersection to the same order of accuracy as that achieved for the input beams. It should also be true, at least to a first approximation, that rays at angles somewhat larger and smaller intersect in the same vicinity. Figure 5 illustrates this geometry. Such a system requires only one correction lens design which has an obvious cost advantage. This basic design approach was adopted for the correction lens system.

An interesting property of the correction lens was discovered after a few lens configurations were found that were workable. When the thick lens equation from geometrical optics [28]:

$$\frac{1}{f} = (n_1 - 1) \left[\frac{1}{R_1} - \frac{1}{R_2} + \frac{(n_1 - 1)d}{n_1 R_1 R_2} \right] \quad (2)$$

is applied to the tube wall, the effective focal length that is obtained is approximately the same as the effective focal length of a workable correction lens based on the same equation. This is an unexpected result because the thick lens equation is derived using paraxial theory and a small angle assumption which is violated for the tube wall. Various cylindrical lens configurations were checked as well as other sizes and thicknesses of tubing and the same result was found in each case, i.e., a workable correction lens has

approximately the same effective focal length as the tube wall when the wall thickness is less than 20% of the inside radius. This empirical rule can be used as a starting point when designing correction lenses for new tube dimensions.

4. EXPERIMENTAL VERIFICATION

The correction lens was relatively easy to fabricate, since it only had one cylindrical surface. A more detailed description of the lens grinding and polishing process is given in Appendix B. A pair of lenses were ground and polished from acrylic plastic blocks, and were tested on an optical bench to confirm that their performance would match that predicted by the ray tracing routine. A half section of the tube was mounted on the bench with one of the correction lenses located in front of it. A microscope objective mounted on a three dimensional position indicator was used to locate the actual beam intersection point in the tube for various beam orientations, radial locations, and correction lens positions. The measured intersection points agreed well with the ray trace predictions. The maximum deviation was approximately 0.05 mm (0.002 in) perpendicular to the bisector and 0.15 mm (0.006 in) along the bisector. When the plane of the input beams was rotated, the probe volume location remained stationary within the specified tolerances (0.1mm along the bisector, 0.025 mm perpendicular to it) for all radial locations out to $r/R = 0.83$ (the actual probe

volume location for a virtual location of $r/R = 0.8$). At larger radii the probe volume movement exceeded the specified tolerances when the beam orientation was rotated, but these movements were still as predicted by the ray tracing program. The lens was also effective in minimizing probe volume distortion and enlargement.

Next a full tube section was mounted on the bench with both a transmitting and receiving correction lens in place. The setup was used to check the receiving optics and is illustrated in Figure 7. The location of the probe volume image was measured for various radial locations and with rotation of the input beams to insure that the LDV receiving optics would not require any major readjustment. The location of the probe volume image (where the photomultiplier tube pinhole would be located) remained stationary within approximately 0.38 mm in the x direction and 0.1 mm in the y direction. Thus only minor readjustment of the pinhole location is needed to optimize signal quality after the system is moved to a new measurement position or rotated. It has been our experience that to maximize signal quality minor adjustments of the same magnitude are required when repositioning in a plane walled channel.

It is worthwhile to note that the beams exiting the tube are not symmetrical with the beams entering the tube because of the previously noted angular deviation of the input beam bisector. This caused no apparent optical

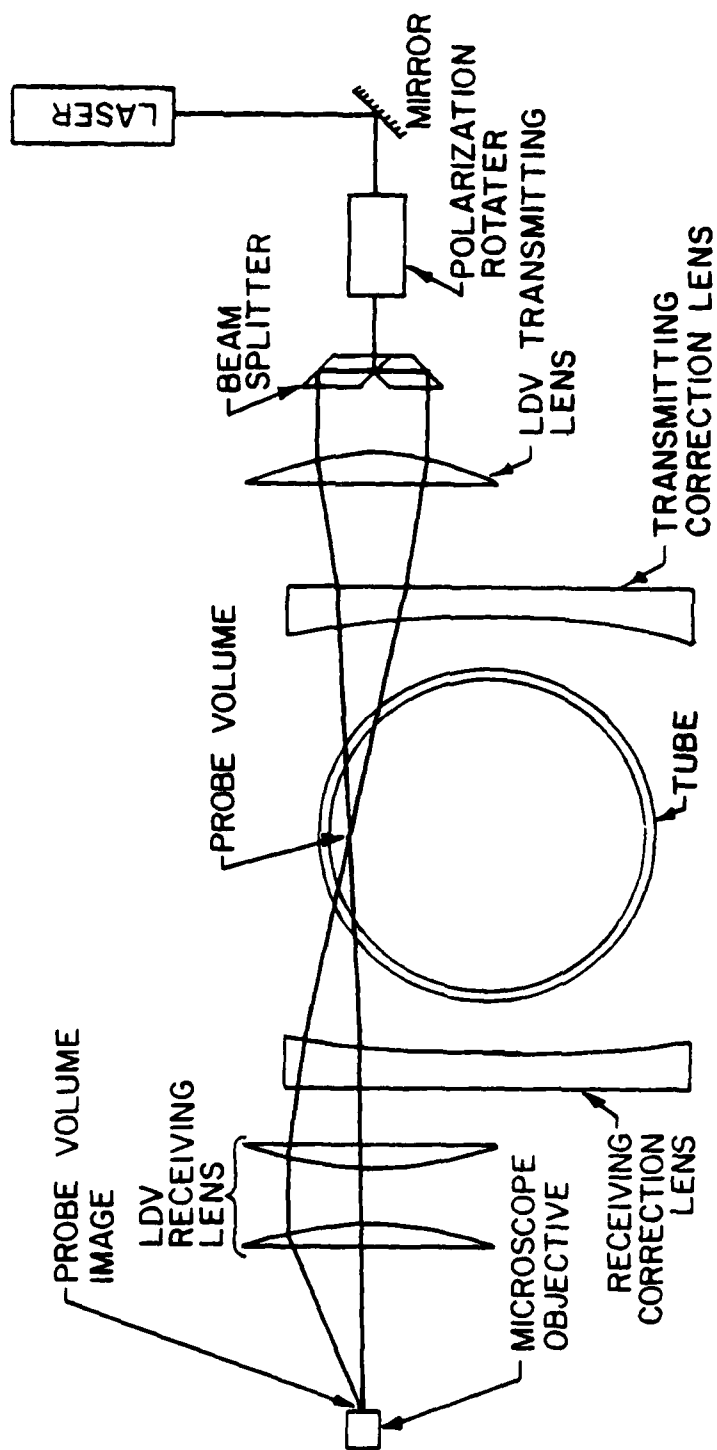


Figure 7. Optical Bench Setup Used to Test Correction Lenses

problems however, and the exiting beams were still focused at the proper location, even though the transmitting and receiving optics remained in the same relative position at all times. The separation of the correction lenses was changed for different measurement points along the tube radius as noted earlier, but no other adjustment of the optical elements was necessary.

Although the design program only employed ray traces in planes parallel and perpendicular to the tube axis, the lens was found to work satisfactorily for all angular orientations of the input beam plane. This was expected because the vector refraction equation, Eq. (1), can be decomposed into three independent orthogonal scalar refraction equations. The scalar equations are independent and at each surface a skew ray can be resolved into orthogonal components and one equation applied to each component. If the angle between the beams is small the difference between the traces of the skew beams and the beams in the plane will be small.

SECTION IV

EXPERIMENTAL APPARATUS

1. INTRODUCTION

The mapping of the experimental flow field in the axisymmetric sudden expansion required several types of instrumentation and hardware. The LDV used with this experiment was designed specifically for the investigation of the effects of data acquisition methods and system parameters on measurements in highly turbulent flows. The system allowed for variation in LDV optical parameters, seeding particle density and data sampling conditions. This section describes the experimental apparatus which may be divided into four major subsystems:

1. The flow system
2. The LDV optical system
3. The data collection, storage, and processing system.
4. The seeding system.

2. THE FLOW SYSTEM

The flow system used in this experiment was designed to provide a flexible system which has easy optical access.

The test section geometry was an axisymmetric sudden expansion following a two-dimensional converging nozzle. The flow system used was the same system that was used for a previous experiment [17], with the addition of a plenum chamber and slight modifications to the flow conditioning section. As shown in Figure 8 the flow system consisted of six parts:

1. A radial vane blower
2. A plenum chamber
3. A flow conditioning section
4. A connecting duct
5. A test section
6. An extension duct

The radial vane blower was a Peerless model PWB14GA driven by a variable speed direct current motor. The maximum flow capacity of this unit was approximately 1100 cfm.

The plenum chamber consisted of a 610 x 915 x 1229 mm (2 x 3 x 4 foot) box constructed of 9.5 mm (3/8 inch) plywood on an angle iron frame. The chamber was mounted on a stand directly above the blower and the flow entered the plenum via a simple square-edged inlet. This inlet was located in the center of the base of the chamber to minimize swirl in the chamber and thus minimize swirl in the test section. A bell shaped nozzle with an area ratio of 4:1 was employed for the outlet of the plenum chamber.

The flow conditioning section consisted of a set of flow straighteners with 95.2 mm (3 3/4 inches) inside diameter and 178 mm (7 inches) in length and was attached

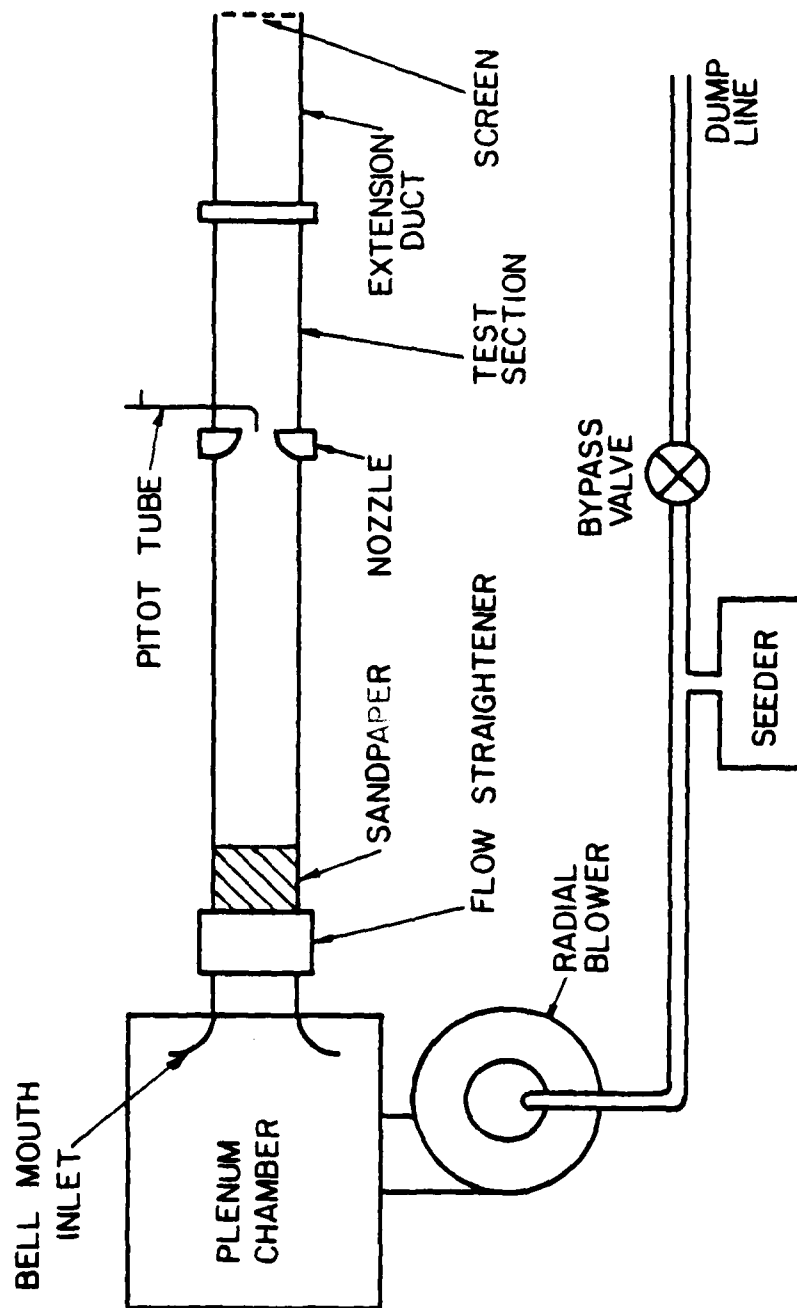


Figure 8. Flow System

directly to the outlet bell of the plenum chamber. The elements of this section included three screens spaced 50.8 mm (2 inches) apart. For the experiments in the axisymmetric sudden expansion, 18 mesh window screen was used for the straightener, but for the straight pipe tests, 100 mesh screens were found to give better results. The honeycomb section that was used in previous experiments was found to be unnecessary.

The connecting duct was constructed of two sections of Plexiglass tubing with an inside diameter of 95.2 mm (3 3/4 inches) and a wall thickness of 3.2 mm (1/8 inch). The total length of the connecting duct was approximately 32 pipe diameters. For the experiments with the straight pipe test section, the first 279 mm (11 inches) of the connecting duct was artificially roughened with #320 grit sandpaper in order to accelerate boundary layer development. The sandpaper was not used for the sudden expansion tests.

The test section consisted of two parts, a duct section and a nozzle, as shown in Figures 9 and 10, both fabricated from commercial grade clear Plexiglas. The duct section had an inside diameter of 95.2 mm (3 3/4 inches), a wall thickness of 3.2 mm (1/8 inch) and was 610 mm (24 inches) in length. A 25.4 mm (1 inch) thick flange was used on each end of the duct to join it to the adjacent sections. The flanges were also used to mount the support rods for the correction lenses which will be described later. Two

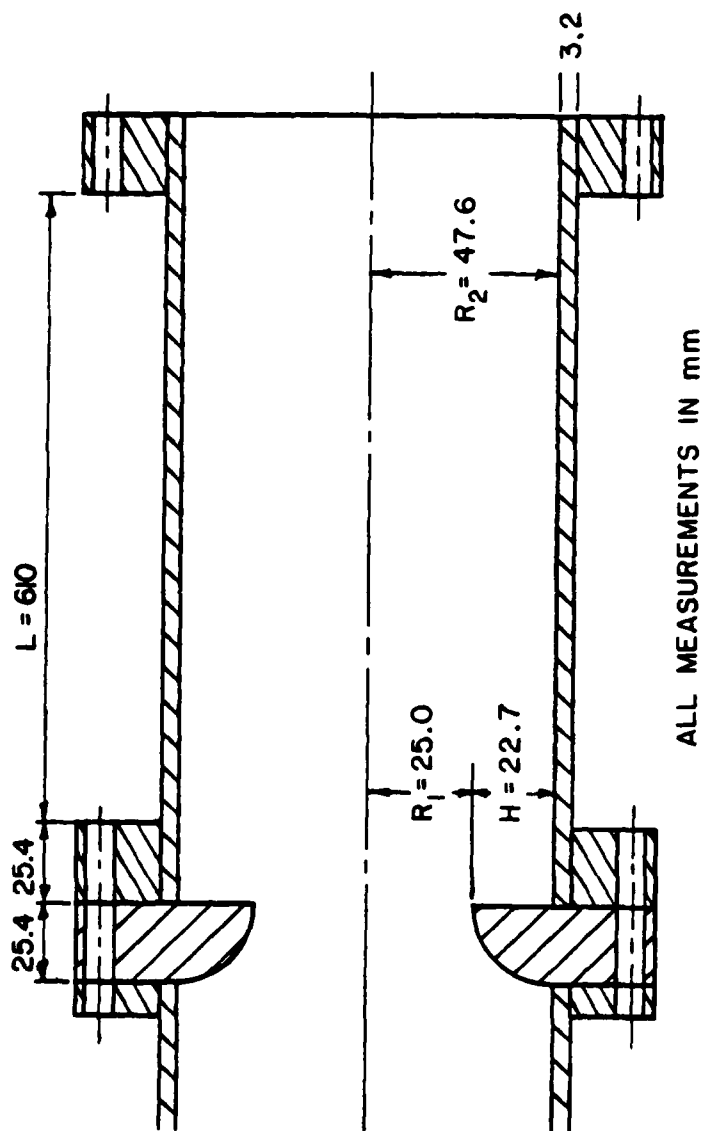


Figure 9. Geometry of Test Section with 1.90:1 Nozzle

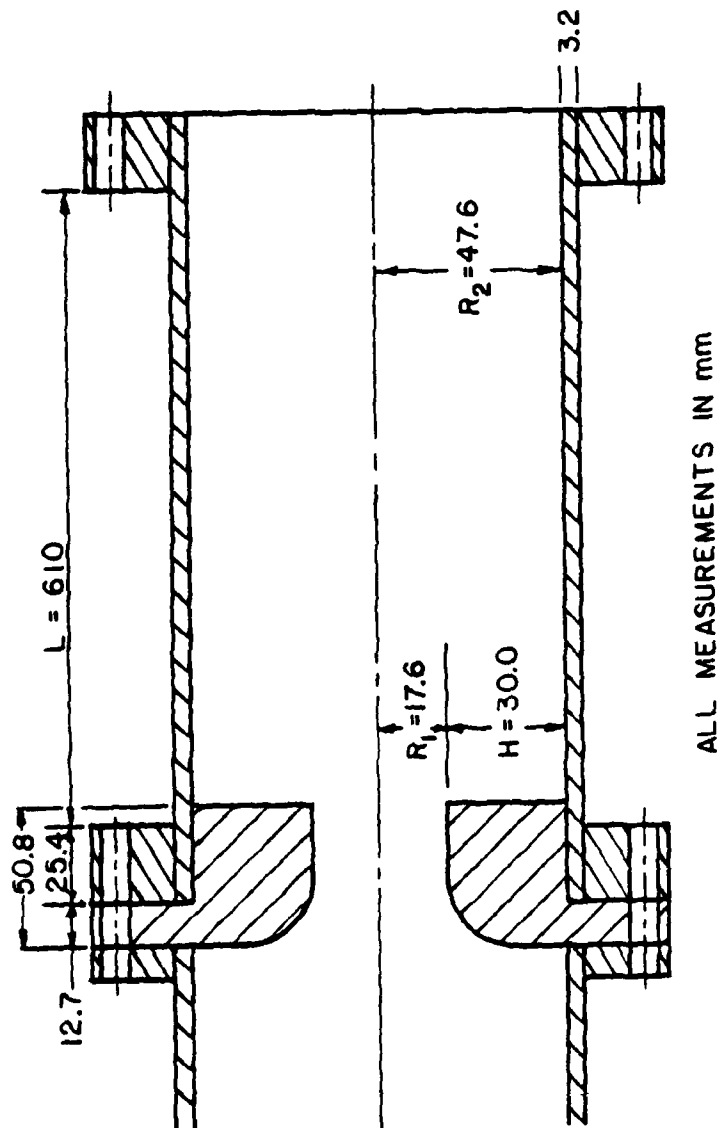


Figure 10. Geometry of Test Section with 2.70:1 Nozzle

different nozzles were used for the sudden expansion tests. The majority of the tests (all tests for $x/H > 2$) were made with a nozzle 25.4 mm (1 inch) long with a throat 50 mm (1.97 inches) in diameter and a diameter ratio of 1.90:1. The combination of a 50 mm diameter nozzle exhausting into a 95.2 mm diameter duct created the sudden expansion effect. Because of the interference of the flange on the front end of the test section, measurements could not be closer than approximately $x/H = 1.75$ to the nozzle.

A second nozzle was fabricated in order to study the flowfield very close to the expansion. As shown in Figure 10, this nozzle was designed so that the flange would not interfere with measurements. The throat diameter was 35.2 mm and the diameter ratio was approximately 2.70:1. Since a new nozzle had to be fabricated for this experiment, this smaller throat diameter was chosen so that the annular recirculation zone would be larger and stronger. Measurements were made with this nozzle in the range $0.1 < x/H < 1.5$.

The test section exhausted into a 1700 mm (67 inch) long extension duct which in turn exhausted into the room. The end of the extension duct was covered with 18 mesh window screen. This screen was found to make the flow more stable, especially for the straight pipe flow case, and less susceptible to outside interference.

THE LDV OPTICAL SYSTEM

The LDV used was a one component system operating in the dual beam forward scatter mode. The system has the capability of changing probe volume size, fringe spacing, and angular orientation. Frequency shifting one or both beams and traversing the probe volume in three-dimensional space are also possible. The general layout of the LDV is shown in Figure 11.

Laser light for the system is provided by a five watt Coherent Radiation Model 52 argon ion laser normally operated on the green line ($0.5145 \mu\text{m}$). Upon exiting the laser, the beam enters a polarization rotator (Spectra-Physics, Model 310-21) which insures that the plane of polarization of the laser beam remains perpendicular to the plane of the beam dividing prism as the upper optics package is rotated. Maximum fringe contrast is produced in the probe volume when the two beams are of equal intensity. After the polarization rotator, the beam passes through a beam expander telescope consisting of a 44 mm focal length lens and a 68 mm lens. Traversing the second lens over a 7.5 mm range varies the beam waist diameter from 60 to $500 \mu\text{m}$.

Following the telescope, two broadband all-dielectric mirrors (Newport Research Corp.) direct the beam to the upper optics package where it enters the beam splitter (TSI, Model #916-1). The beam splitter divides the entering beam

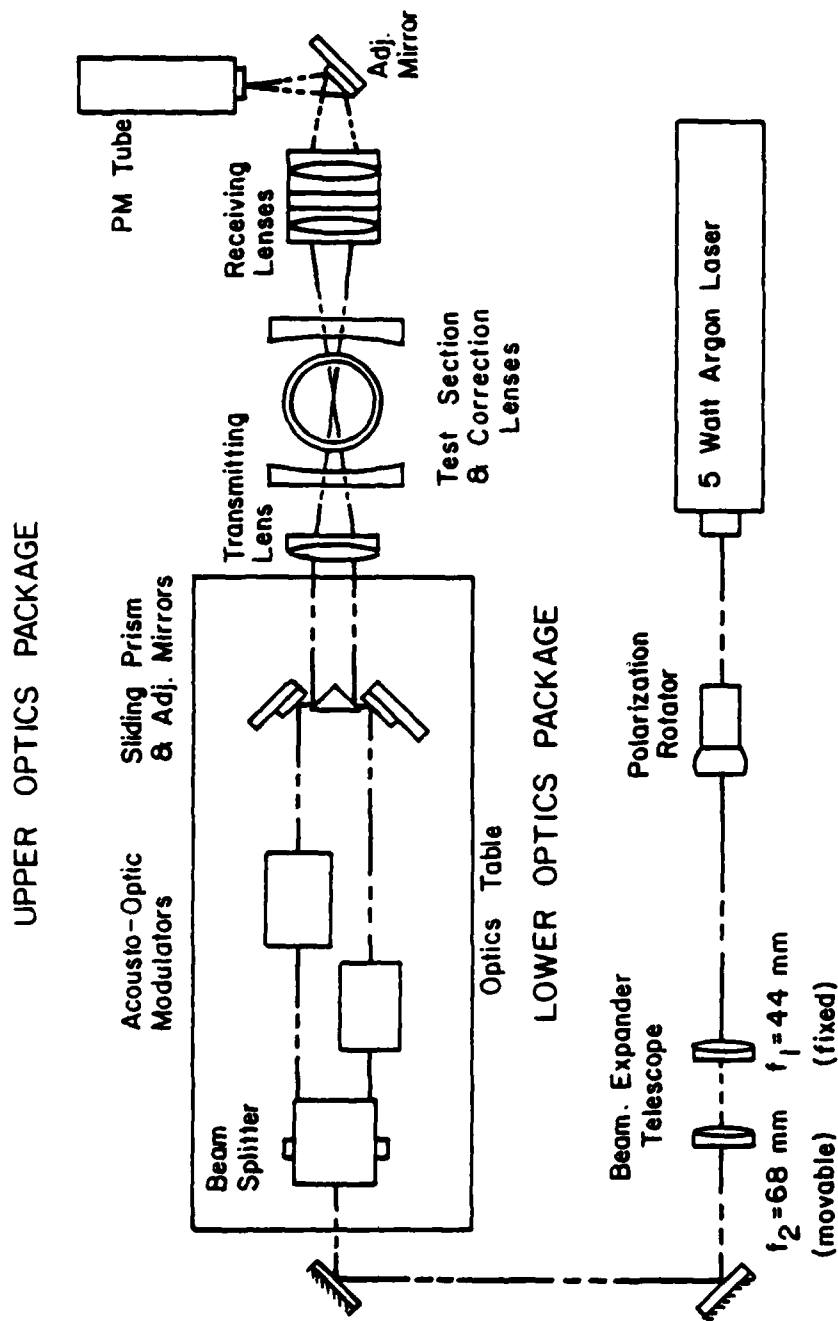


Figure 11. LDV Optics Package

into two parallel beams of equal intensity separated by 50 mm. These beams enter two acousto-optic modulators (Intra-Action Corp. Model #ADM-40) which shift the frequency of the incoming beam by an amount equal to the frequency of the driver. Each driver can shift the frequency of the beam either up or down, allowing for a wide range of net frequency shifts between the beams. For the present study a net frequency shift of 10 MHz was used. This provided an offset of approximately 40 m/s allowing unambiguous measurement of positive and negative velocities.

After leaving the modulators the beams are reflected by adjustable mirrors (Newport Research Corporation, Model #600-2) to a sliding prism. The prism, which has a reflective coating on two faces, controls the separation of the beams as they pass through the transmitting lens. The transmitting lens (TSI, Model #918) has a focal length of 250 mm. By making adjustments to the beam expander telescope, the adjustable mirrors, and the sliding prism, the operator can vary the fringe spacing and number of fringes in the probe volume and insure that the probe volume is formed at the waists of the beams and on the axis of rotation of the upper optical table.

Scattered light from particles passing through the probe volume is collected, collimated, and then focused by a pair of receiving lenses (both TSI, Model #918) both with a focal length of 250 mm and mounted several centimeters

apart. The focused light is reflected by a mirror mounted on an adjustable fixture (Newport Research Corporation, Model #600-2). This adjustable mirror allows fine lateral adjustment of the focused spot insuring that it is located on the 200 μm pinhole. The pinhole is part of a pinhole-lens combination that is threaded into the front of the photomultiplier tube (RCA, Model #8575) and allows fine axial adjustment of the focused spot. The small positive lens collimates the light passing through the pinhole for improved performance of the PM tube. No optical filter was used on the PM tube since it was found to be unnecessary and degraded the performance of the system. The entire receiving optics package may be moved along the optical axis for coarse adjustment of the probe volume image on the pinhole. Beam stops on the first receiving lens block the direct laser beams and any stray light reflections allowing only scattered light to pass into the PM tube.

The upper transmitting optics table is mounted on bearings that allow angular rotation about the optical axis and thus permit any velocity component in a perpendicular plane to be measured. The entire LDV optical system is mounted on a milling machine bed which can be translated in any of the three cartesian directions by three Bodine D.C. gearmotors with variable speed controls. Linear potentiometers (New England Instrument) are used to obtain a readout of the position of the bed directly in millimeters to an accuracy

of ± 0.1 mm. A more detailed description of the LDV system is given by McVey [29].

4. THE DATA COLLECTION, STORAGE, AND PROCESSING SYSTEM

The photomultiplier tube output was connected to a Tektronix Model 454A oscilloscope and a TSI Model 1980 LDV signal processor [30]. The oscilloscope was used to check the output from the PM tube and the filtered output from the signal processor to insure that signal quality was good. The LDV signal processor features a 250 MHz clock with two nano-second resolution and capability for either digital or analog output. Only the digital output was used in this investigation. In the absence of external control of the processor, the data rate (number of validated velocity realizations per second) depends on the rate at which seeding particles enter the probe volume, the processor gain setting (which effectively sets the trigger level), the laser power, the PM tube supply voltage, and the required number of cycles per Doppler burst. For this study, data rates of approximately 20,000 realizations per second were obtained for all runs. The rate at which particles enter the test section was controlled by the seeder output rate and by a bypass valve between the seeder and a dump tube.

Data acquisition and short term storage were performed by an IMSAI 8080 microcomputer and Micropolis floppy disk

system. Data could be sampled by microcomputer control from rates as low as 0.1 sample per second to approximately 4800 samples per second. The microcomputer had the capability of storing 15,600 data points in its memory. After sampling, the data were written onto a floppy disk for temporary storage. Each disk is capable of storing 100,000 data points. The microcomputer also interfaced with Purdue University's CDC 6500 and 6600 computers, which were used for all data reduction.

The microcomputer and TSI processor were also interfaced so that the velocity sampling was jointly controlled by the processor and the microcomputer. When the TSI processor has a data point ready, it transmits a data ready pulse to the microcomputer. Upon reception of the data ready pulse the microcomputer returns a data inhibit pulse to the TSI processor. The inhibit stops the processor from accepting more data and causes it to hold the present data until it can be read. The microcomputer waits a fixed amount of time, chosen by the operator, before reading the data point. After the data is read the data inhibit is removed by the microcomputer and the cycle continues until the desired number of samples has been taken. The rate at which data is actually taken is therefore controlled by the slower of the two instruments. When seeding density is high and the sampling time interval is long relative to the particle arrival rate, the data will be acquired at essen-

tially equal time intervals and an unbiased velocity distribution will result [2,4].

5. THE SEEDING SYSTEM

The seeder used for this study was one which is commercially built by TSI. It consisted of a Model 3074 air supply, a Model 3076 liquid atomizer and a Model 3072 evaporation-condensation monodisperse aerosol generator. This system produced seeding particles approximately one micron or less in diameter using a solution of 100% Dioctyl Phthalate (DOP). The quantity of seeding particles introduced into the flow system was controlled by two methods. First, the air pressure supplied to the atomizer was varied between 20 and 40 psi which controlled the amount of seed produced by the seeder. Second, a bypass valve was installed in the seeder supply line which allowed a portion of the seed particles to be dumped outside. Operation in this manner allowed the seeding density in the test section to be varied so that there was sufficient seeding available to maintain a data rate in excess of 20,000, but not so much that the DOP accumulating on the test section wall degraded the optical performance of the system. The system could typically be run from 4-5 hours before the DOP accumulation was severe enough to cause a problem.

The seeding particles were introduced into the flow system in one of two ways, depending on the type of screen used in the flow conditioning section. The 100 mesh screen that was used for the straight pipe flow test would slowly become clogged with DOP. As the DOP built up on the screen it was impossible to maintain a steady flow rate. Thus, for these tests, the seeding particles were injected just downstream of the flow conditioning screens. The particles were injected through the static pressure ports of a pitot probe inserted into the flow. For the axisymmetric sudden expansion runs, the 18 mesh screen did not exhibit the same clogging problems and the seeding particles were injected into the inlet of the blower.

SECTION V
EXPERIMENTAL TECHNIQUE

1. INTRODUCTION

The experimental mapping of both the fully developed pipe flow and the axisymmetric sudden expansion flow fields consisted of both direct measurements and indirect calculations of quantities obtained from these measurements. This section presents the techniques used to obtain the following flow field parameters:

1. Mean velocities, \bar{u}_x , \bar{u}_r
2. Turbulence parameters, $\overline{u'^2_x}$, $\overline{u'^2_r}$,

$$\overline{u'_x u'_r}, \left[\overline{u'^2_x} + \overline{u'^2_r} \right]$$

3. Wall friction velocity, u_τ
4. Stream function, ψ
5. Integrated mass flow rate

Also included in this section are the values of the various LDV system and flow system parameters used in this study.

2. FLOW SYSTEM PARAMETERS

As noted previously, three different test section configurations were used; a simple straight pipe test section, a sudden expansion with a diameter ratio of 1.90 and a sudden expansion with a diameter ratio of 2.70. For each of the three configurations, all flow conditions were maintained at near constant values throughout the testing procedure. The flow system parameters are summarized in Table 4.

The first tests were done in fully developed turbulent pipe flow. The nozzle shown in Figure 8 was removed for this phase of the study. This particular flow was chosen for the first tests of the correction lenses because of the simplicity of the flow field and because there is much data in the literature for comparison. In particular, the data of Laufer [31] is widely accepted. While turbulent flow was easily obtained in the test section, tedious and time consuming modifications had to be made to obtain axial symmetry. The task was probably made more difficult by the fact that the flowrate had to be kept relatively low in order for the seeding density to be high enough to maintain the required LDV data rate of 20,000 validations per second. The straight pipe tests were made with a centerline velocity of 8.3 ± 0.1 m/s corresponding to a Reynolds number $Re_D = 48,000$. Axial and radial mean velocities and turbulence intensities were measured along a vertical diameter

Table 4. Flow System Parameters

a.) Fully developed turbulent pipe flow

U_0 (centerline velocity): $8.3 \text{ m/s} \pm 0.1 \text{ m/s}$

Re_D (based on centerline velocity): 48,000

R : 47.6 mm

b.) Axisymmetric sudden expansion, $R_2/R_1 = 1.90$

U_0 : $27.9 \text{ m/s} \pm 0.1 \text{ m/s}$

Re_{D_1} (based on nozzle exit diameter): 84,000

H (step height): 22.6 mm

R_1 (inlet radius): 25.0 mm

R_2 (outlet radius): 47.6 mm

c.) Axisymmetric sudden expansion, $R_2/R_1 = 2.70$

U_0 : $39.5 \text{ m/s} \pm 0.5 \text{ m/s}$

Re_{D_1} : 83,500

H : 30 mm

R_1 : 17.6 mm

R_2 : 47.6 mm

(perpendicular to the LDV optical axis) using the correction lens. Reynolds stresses and turbulence kinetic energies were calculated from measurements made at +45 and -45 degrees with respect to the tube axis. Axial and tangential mean velocities and turbulence intensities were measured along a horizontal diameter (parallel to the LDV optical axis) without the lens.

The majority of the tests were made in the axisymmetric sudden expansion with a diameter ratio of 1.90:1. This test section geometry was used in a previous investigation [17] so there was some data available for comparison of the axial velocity measurements. The centerline velocity at the nozzle exit was $27.9 \text{ m/s} \pm 0.3 \text{ m/s}$ corresponding to a Reynolds number based on inlet centerline velocity and nozzle exit diameter of 84,000. Measurements were made at 6 axial locations corresponding to $x/H = 2, 4, 6, 8, 12, \text{ and } 20$ as shown in Figure 12. The radial locations chosen for measurements depended on the axial location of the grid line. Nine radial locations were standard for each grid line; $r/R = 0.0, 0.15, 0.3, 0.4, 0.5, 0.6, 0.7, 0.8, \text{ and } 0.9$. In addition the first four axial locations, which were in the recirculation zone, had two additional measurement points added to give more information in the shear layer. It should be noted that the radial locations listed above represent the movement of the LDV system with respect to the flow system and are the virtual probe volume locations. The

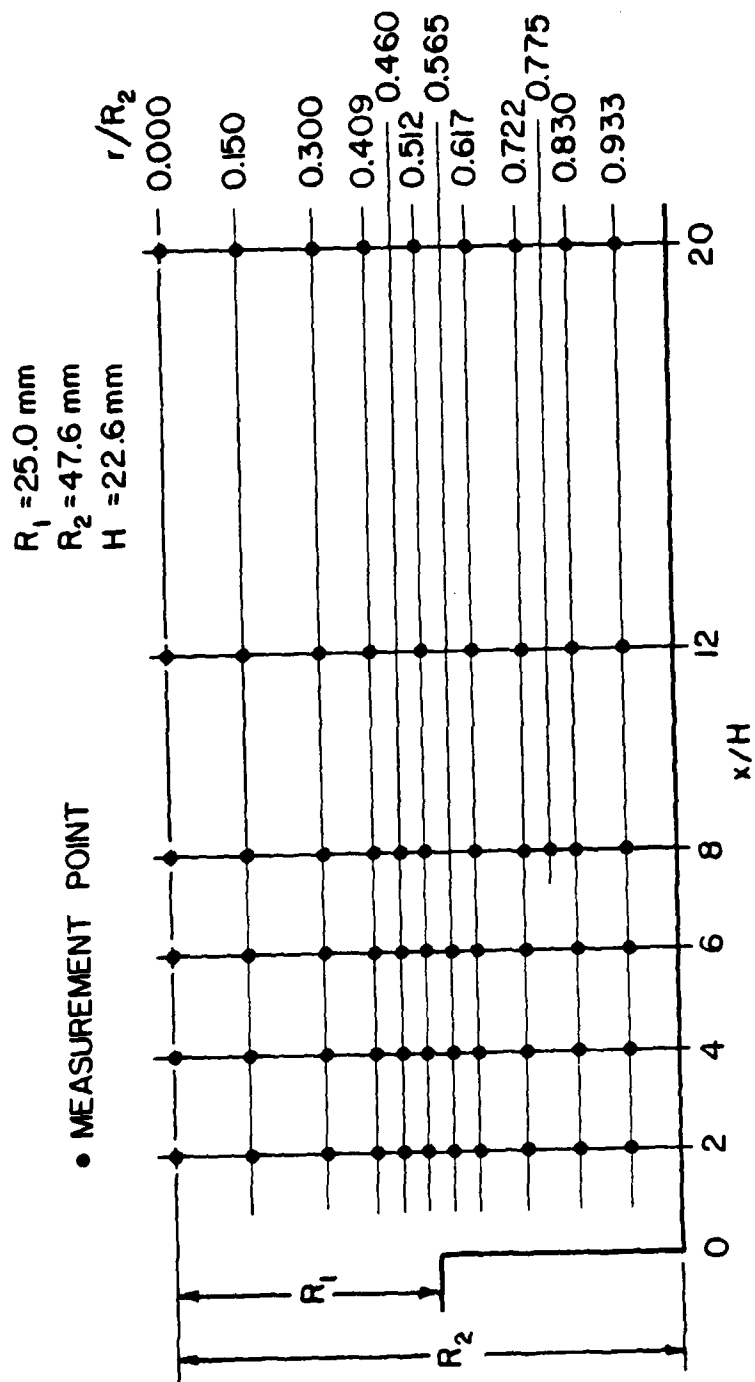


Figure 12. Experimental Measurement Grid for 1.90:1 Sudden Expansion

radial locations shown in Figure 12 represent the actual location of the probe volume due to refraction by the correction lens and the tube wall. Axial and radial mean velocities and turbulence intensities were measured at each point. Reynolds stresses and turbulence kinetic energy were then calculated from turbulence intensity measurements.

The final series of tests were made in the sudden expansion with a diameter ratio of 2.70. The purpose of this test was to investigate the flow in the region very close to the expansion in an attempt to detect the secondary recirculation zone driven by the primary recirculation zone. The centerline velocity at the nozzle exit was $39.5 \text{ m/s} \pm 0.5 \text{ m/s}$ corresponding to a Reynolds number based on nozzle diameter of 83,500, approximately the same as for the previous sudden expansion geometry. Measurements were made at seven axial and six radial locations as shown in Figure 13. Only axial and radial mean velocities and turbulence intensities were measured.

Although the system geometries were all axially symmetric, measurements made to test the flow symmetry showed a high degree of asymmetry in the original straight pipe flow setup. Only after adding a large plenum chamber downstream of the blower and making tedious adjustments to the flow straightener was a reasonable degree of flow symmetry achieved. For the sudden expansion configurations, symmetry was checked by making a few selected measurements of the

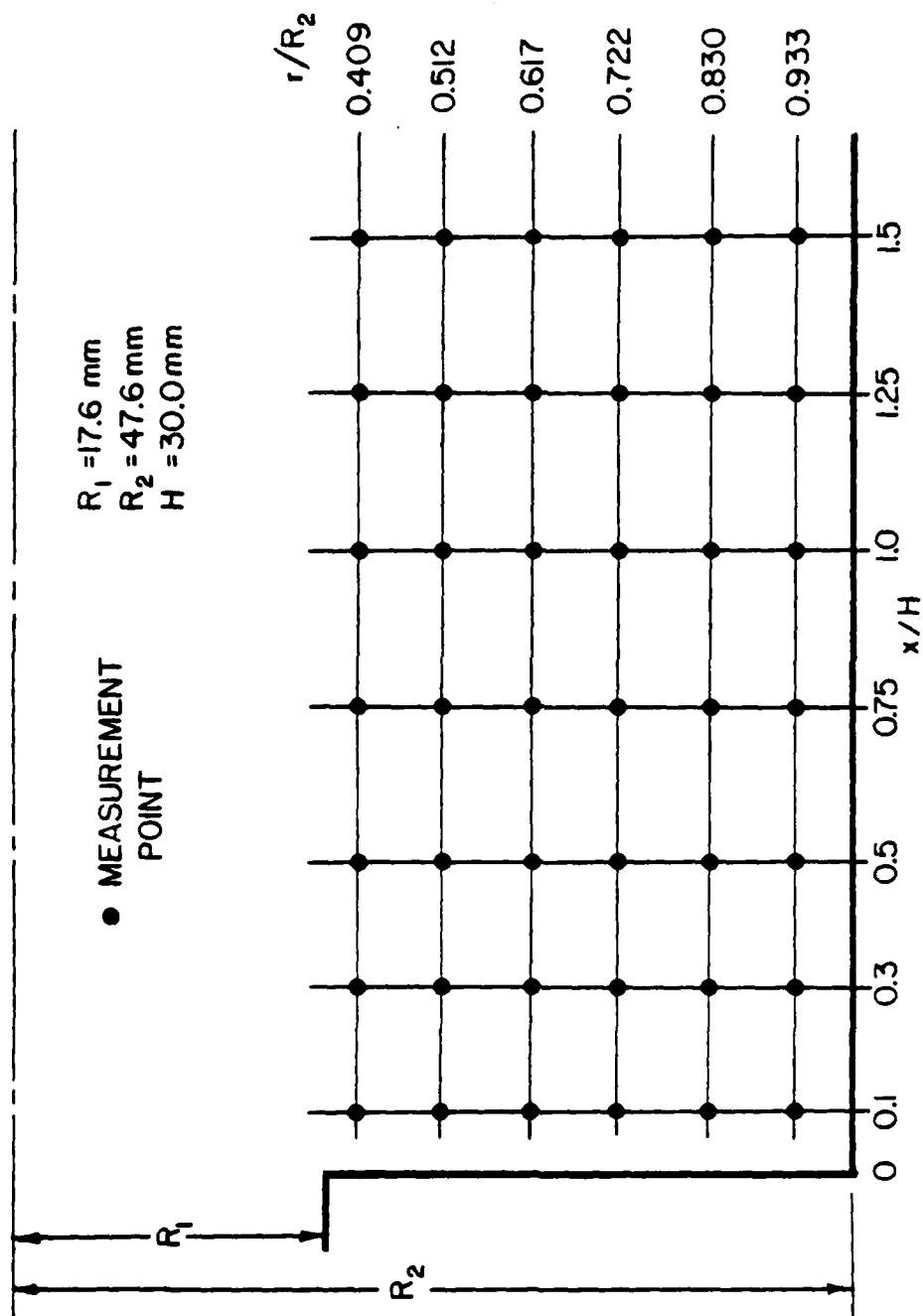


Figure 13. Experimental Measurement Grid for 2.70:1 Sudden Expansion

axial velocity on a horizontal diameter. These measurements were in excellent agreement with the measurements that were made on the vertical diameter for both sudden expansion configurations and confirmed that the flow was, in fact, axially symmetric.

3. OPTICAL SYSTEM PARAMETERS

The mean velocities and turbulence parameters were calculated from LDV measurements at various grid points in the flow field. The alignment of the optical system was regularly checked to insure continuity of technique and minimize sources of error. Table 5 lists the system parameters used throughout the experiment.

The techniques employed to obtain the beam waist diameter and position can be found in Ref. [29]. The beam intersection half angle, $\theta/2$, was 3.55 ± 0.07 degrees. Corresponding fringe spacing, F_R , was $4.15 \pm 0.10 \mu\text{m}$ which was determined from the relationship:

$$F_R = \frac{\lambda_0}{2 \sin(\frac{\theta}{2})} \quad (3)$$

The seed particle diameter was approximately $1 \mu\text{m}$.

Table 5. LDV System Parameter Settings

Optical System Settings

λ_0 (laser frequency): 0.5145 μm
 $\theta/2$ (beam intersection half angle): $2.44^\circ \pm 0.03^\circ$
 F_R (fringe spacing): $4.15 \mu\text{m} \pm 0.4 \mu\text{m}$
Probe volume size (waist diameter): $130 \mu\text{m} \pm 5 \mu\text{m}$
 f_s (frequency shift): $10 \text{ MHz} \pm 1 \text{ KHz}$

Data Collection Settings

Electronic filter settings: 30 MHz (low pass)
3 MHz (high pass)
N (number of fringes/signal): 16
Comparator: 3 (3.1%)
n (exponent): floating
Sample size: 4500 samples
Data rate: > 20,000 particles/sec
Sample rate: 50 particles/sec
Seed particles: dioctyl phthalate - DOP

The net frequency shift employed, f_g , was 10 MHz \pm 1 KHz. As shown in Appendix C, the uncertainty in the frequency shift is negligible. The positive frequency shift indicates that the fringes are moving upstream against the mean flow direction, in this case with an "apparent velocity" of 41.5 m/s. This was adequate for the identification of negative velocities at all points in the the flow field.

The output signal of the photomultiplier tube was filtered to remove the low frequency "pedestal" and any high frequency noise. A 30 MHz low pass filter and a 3 MHz high pass filter were used. The LDV processor was operated in the N cycle mode with the number of cycles per burst set at $N = 16$. A 16 to 8 fringe count comparison was used with the accuracy of this comparison set at 3.1% (comparator = 3). This means that the time for a particle to cross 16 fringes is compared with twice the time for the particle to cross the first 8 of the 16. An error in the comparison of more than 3.1 percent results in the measurement being rejected. These LDV processor parameters have been used for past investigations at this facility with excellent results.

Each sampled output of the TSI processor consisted of three digital numbers, namely N (cycles/burst), n (exponent) and D_m (digital mantissa). The value of the exponent (n) was allowed to float so that the maximum number of significant figures would be included in the mantissa. This data was converted into a frequency, f , and then a velocity, u_1 ,

with the following equations [30];

$$f = \frac{N \times 10^8}{D_m \times 2^{n-2}} \quad (4)$$

and

$$u_i = [f - f_s] F_R \quad (5)$$

where f_s is the frequency shift and F_R is the fringe spacing.

4. MEAN VELOCITY AND TURBULENCE PARAMETER MEASUREMENTS

The mean velocities and turbulence parameters were calculated from the ensemble of LDV measurements at each grid point in the flowfield. The mean, \bar{U} , and variance, $\overline{u'^2}$, at each point were obtained from the following equations;

$$\bar{U} = \frac{1}{N} \sum_{i=1}^N u_i \quad (6)$$

$$\overline{u'^2} = \frac{1}{N} \sum_{i=1}^N [u_i - \bar{U}]^2 \quad (7)$$

When computing values from Equations (6) and (7) all individual measurements which were more than ± 3 standard deviations from the mean were discarded as noise. The number of discarded points was typically between 10 and 75 points out of the 4500 depending on the location of the point in the tube. Measurements made near the wall generally had more points discarded. This was probably due to the stray light reflections caused by the LDV beams intersecting the tube wall at a shallow angle.

Since a one component LDV was used, the Reynolds stress and turbulence kinetic energy, could not be calculated directly but instead were deduced from non-simultaneous measurements using the method of Logan [32]. This method uses the time averaging properties of turbulence to extract the turbulence parameters from turbulence intensities measured at various angles. For a steady flow, it can be shown that at some angle α with respect to the x axis;

$$\overline{u'^2_\alpha} = \overline{u'^2_x} \cos^2 \alpha + 2 \sin \alpha \cos \alpha \overline{u'_x u'_r} + \overline{u'^2_r} \sin^2 \alpha \quad (8)$$

By setting $\alpha = +45^\circ$ and $\alpha = -45^\circ$ in this equation and then subtracting $\overline{u'^2_{-45}}$ from $\overline{u'^2_{+45}}$ a relationship for the shear stress;

$$2 \overline{u'_x u'_r} = \overline{u'^2_{+45}} - \overline{u'^2_{-45}} \quad (9)$$

is obtained. By adding the two equations a relationship is found for the turbulence kinetic energy;

$$\overline{u'^2_x} + \overline{u'^2_r} = \overline{u'^2_{+45}} + \overline{u'^2_{-45}} \quad (10)$$

Since all four of the measurements in Equation (10) were actually made, that relationship provided a check on the consistency of the turbulence data.

5. WALL FRICTION VELOCITY

For a fully developed turbulent pipe flow, the Reynolds stress varies linearly from zero at the centerline to the square of the friction velocity at the wall. The wall shear stress, τ_w , and thus the friction velocity;

$$u_\tau^2 = \left[\frac{\tau_w}{\rho} \right] \quad (11)$$

can be determined in several ways. For this investigation, the easiest and most accurate method is to determine the

tube pressure gradient which defines the average wall shear stress. A simple control volume analysis for a round pipe with constant area gives for the average wall shear;

$$\left[\tau_w \right]_{\text{avg}} = \left[\frac{D}{4} \right] \frac{dP}{dx} \quad (12)$$

The pressure gradient was estimated from static pressure measurements made at the following five locations along the length of the pipe (see Figure 8):

1. the end of the extension duct
2. the front of the extension duct (42.8" from 1)
3. the front of the test section (67.5" from 1)
4. the end of first pipe section (146.8" from 1)
5. the front of first pipe section (188.3" from 1)

As mentioned previously, the nozzle shown in Figure 8 was removed for this phase of the study. The pressure vs distance data are plotted in Figure 14. A least squares fit method was used to determine an average pressure gradient which was found to be $dP/dx = 0.0460 \text{ lbf/ft}^3$. The wall friction velocity was then calculated as;

$$u_{\tau}^2 = 1.56 \frac{\text{ft}^2}{\text{sec}^2}$$

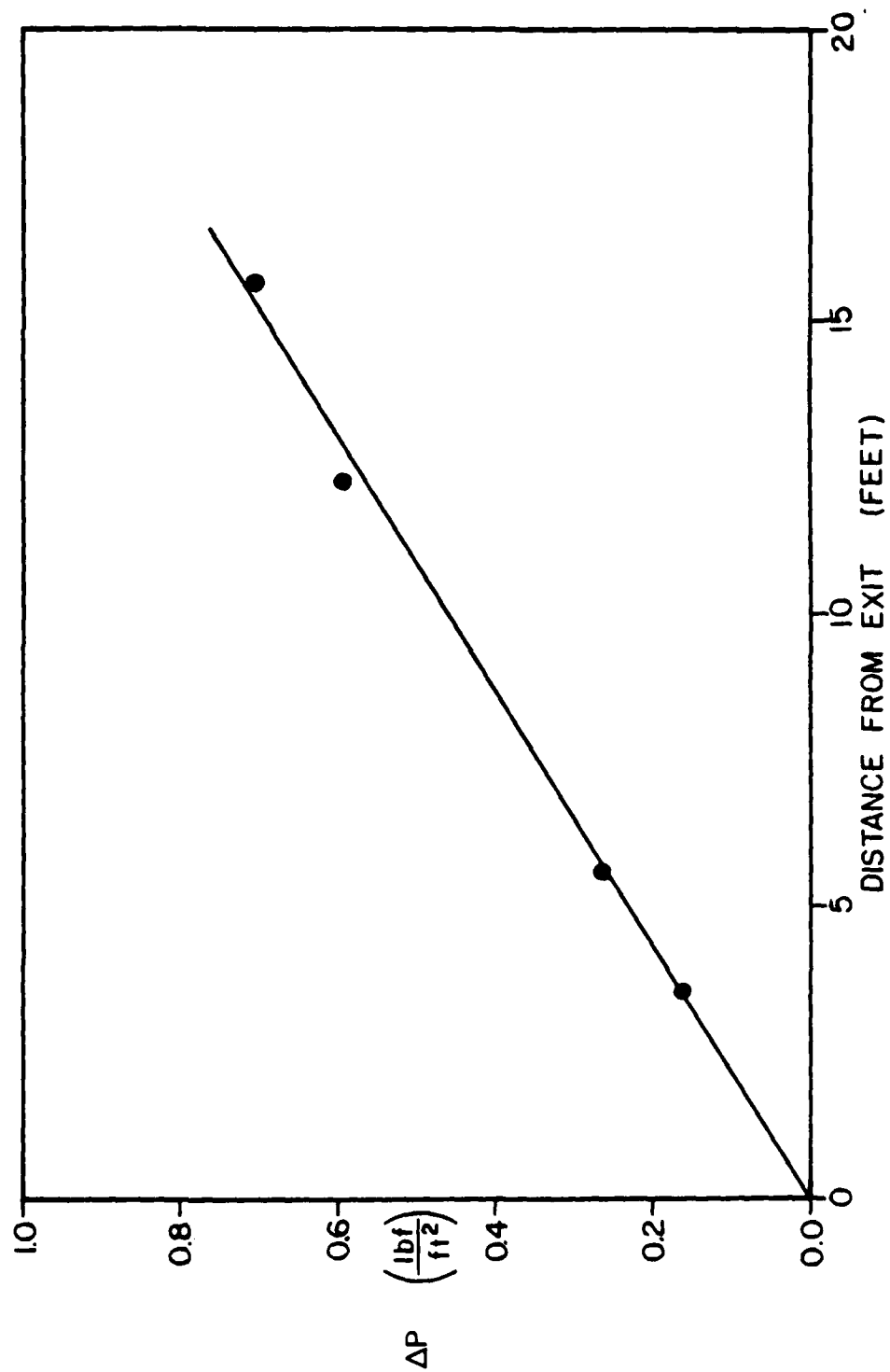


Figure 14. Static Pressure vs. Distance for the Turbulent Pipe Flow

6. THE STREAM FUNCTION

The stream function, ψ , for an axisymmetric incompressible flow is defined by

$$\overline{U}_x = \frac{1}{r} \frac{\partial(r\psi)}{\partial r}, \quad \overline{U}_r = -\frac{\partial\psi}{\partial x} \quad (13)$$

By using the above definitions, the stream function satisfies the continuity equation exactly and it can be shown that the stream function is constant along a streamline. A consequence of this is that at any axial location in an axisymmetric flow field, stream functions can be calculated by integrating the mass flux at that location. The mass flux at each axial location was numerically calculated by piecewise fitting a second degree polynomial to each three points and integrating. From this mass flux calculation, values of the stream function could be determined and contours of the stream function plotted.

7. THE MASS FLOW RATE

As previously discussed, for constant density axisymmetric flow fields, it is possible to compute the mass flux at each axial measurement plane from the measured mean velocity profiles. This permits a check on the accuracy of the axial velocity measurements. The mass flux at each grid line was normalized with the calculated inlet mass flux.

SECTION VI

EXPERIMENTAL RESULTS

1. INTRODUCTION

In this section the results of the LDV velocity measurements are presented for the three flow configurations that have been described. Representative plots of mean velocity and turbulence intensity normalized with the inlet centerline velocity are shown for both the axial and radial directions. Reynolds stress and turbulence kinetic energy profiles are also presented for the 1.90:1 sudden expansion. Flow streamlines, reattachment lengths and integrated mass flux are derived from the experimental data. The reduced experimental velocity data is tabulated in Appendix D and includes mean velocity and standard deviation at each location.

2. TURBULENT PIPE FLOW MEASUREMENTS

As pointed out in the Introduction, the LDV measurements in the fully developed pipe flow were not intended as a complete analysis of this flow. The principal aim of this investigation was to use the correction lenses to make LDV measurement in an actual flow situation. Fully developed

pipe flow was chosen because it was believed to be a relatively simple flow for which there is much data in the literature for comparison. A second reason that this flow was chosen was because the total shear stress in a fully developed turbulent flow increase linearly with radial location. The primary purpose for developing the lens was to make it easier to measure different flow components at a single location and hence measure turbulence correlations.

The "exact" total shear stress profile was easily calculated by measuring the wall shear stress as described in Section V. As shown by Laufer [31], the total shear stress for turbulent flow is the sum of the viscous shear and the Reynolds stress. Thus the Reynolds stress can be expressed as:

$$\overline{u'x'u'r} = \nu \frac{dU}{dr}x + \frac{r}{R} u_{\tau}^2 \quad (14)$$

Since both the mean velocity distribution and the wall friction velocity are known, Equation 14 provides a method of checking the accuracy of the LDV Reynolds stress measurements.

Unfortunately, the uncertainty in the measurements and the relatively low turbulence level in this flow caused the data obtained in this study to be somewhat inconclusive from

the standpoint of fluid mechanics. On the other hand, this series of measurement did show that the correction lenses worked very well in actual experimental application. The adjustments required to the receiving optics when the probe volume was moved from one location to the next was no more than that required for measurements in a flat wall duct. Obtaining the required LDV data rate for velocity bias elimination (20,000) was never a problem either. The data rate criterion was a prime concern in this study because the testing of the correction lens for the receiving optics consisted of only measuring the point at which the two transmitted laser beams intersected after passing through the receiving optics as shown in Figure 7. In the actual LDV application, these two beams are blocked and scattered light from the probe volume travelling along different paths must be correctly imaged on the PMT pinhole. In other words, the transmitting optics must only insure that the two transmitted beams intersect at the probe volume, but the receiving optics must image an entire "cone" of light (or a significant part of it) correctly.

Figure 15 shows the normalized axial mean velocity, measured in the fully developed turbulent pipe flow. Two velocity profiles were measured: one along a diameter parallel to the optical axis (horizontal axis) and the other along a diameter perpendicular to this axis (vertical axis). It is easy to see that some asymmetry still exists in the

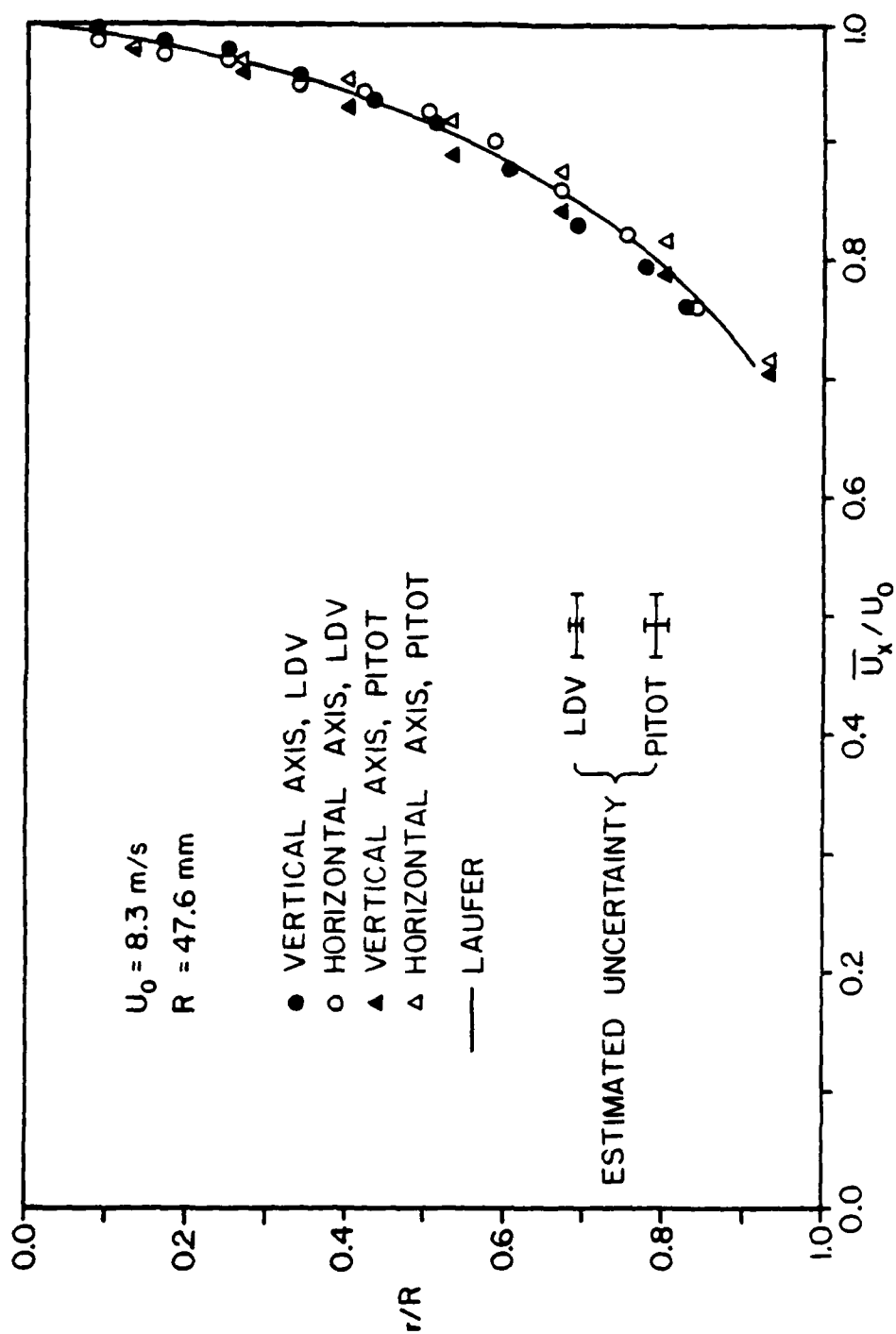


Figure 15. Measured Axial Mean Velocity Profile in the Turbulent Pipe Flow

fully developed flow field, but this profile is much improved over the profile before modifications were made to improve the symmetry. Another observation that can be made is that the radius limit of the lens prevents measurements near the pipe wall.

Figure 15 also shows pitot probe measurements of the axial mean velocity profile along a horizontal and a vertical axis. These measurements were made in the same flow as the LDV measurements and the two data sets are in agreement within the estimated uncertainties. Both sets of measurements can be represented by a $1/7$ power law profile. This is in agreement with the measurements of Nikuradse in [33] for turbulent flow profiles in a smooth walled pipe. The mean velocity data of Laufer [31] ($Re_D = 50000$) are seen to be in good agreement with the present data.

Normalized turbulence intensities for the axial and radial directions are shown in Figure 16 along with the turbulence intensity data of Laufer and that of Barbin and Jones [34]. The grouped sample correction described in Appendix C was applied to all the data. The correction scheme lowered the normalized turbulence intensity values by approximately one half of one percent of U_0 . The trends of the turbulence intensities for the present data are close to the trends of the data of Laufer, but the value of the LDV data is 1 to 1 1/2 percent of U_0 higher, even with the correction for grouping. This remaining difference in

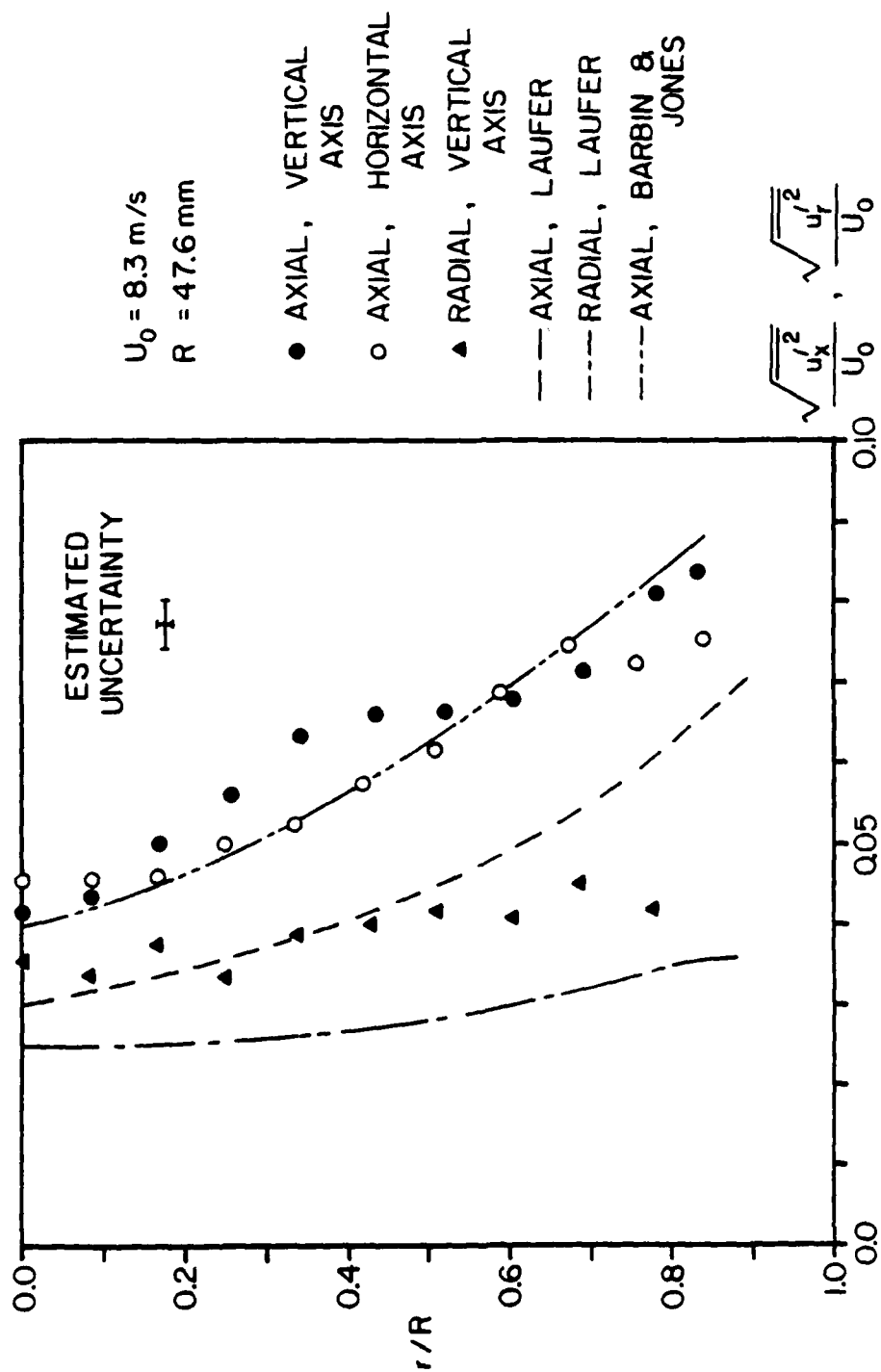


Figure 16. Measured Axial and Radial Turbulence Intensity Profiles in the Turbulent Pipe Flow

turbulence intensities is due partly to the higher level of turbulence present in the inlet flow and partly due to the fact that this flow is not as fully developed as Laufer's. Barbin and Jones [34] measured the development of turbulent flow in a smooth pipe and at the same distance downstream from the inlet ($x/D = 40$) obtained similar results to the present study as shown in Figure 16. Their axial turbulence intensity profile was approximately one percent of U_0 higher than Laufer across the entire profile. This is an interesting result because Laufer's flow was fully developed at $x/H = 30$.

Figure 17 shows Reynolds stress measurements in the flow obtained by the method of Logan from turbulence intensity measurements made in directions oriented at $+45$ and -45 degrees with respect to the axial direction. The solid line represents the Reynolds stress distribution calculated with Equation 14. A $1/7$ power law profile was assumed for the mean velocity distribution. Because of the large amount of scatter in relation to the theoretical shear stress distribution, the experiment was repeated several times. Data sets 1 and 2, represented by the closed and open triangular symbols, were taken at different times before the addition of the plenum chamber between the blower and pipe inlet. Data sets 3 and 4, represented by the circular symbols, were taken on different days after the addition of the plenum chamber. The four data sets agree with one another within

AD-A146 206

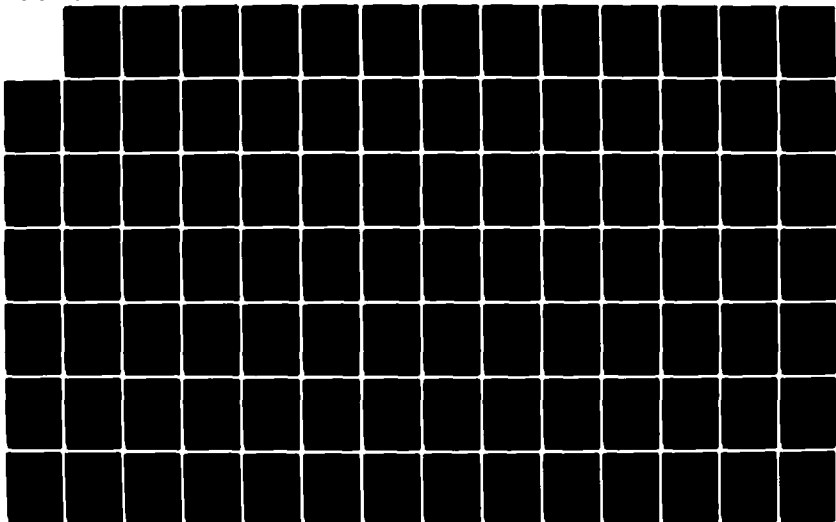
LASER VELOCIMETER MEASUREMENTS AND ANALYSIS IN
TURBULENT FLOWS WITH COMBU..(U) PURDUE UNIV LAFAYETTE
IN SCHOOL OF MECHANICAL ENGINEERING
H D THOMPSON ET AL. JUL 84

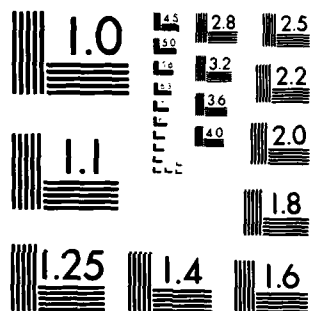
2/3

UNCLASSIFIED

F/G 20/5

NL





MICROCOPY RESOLUTION TEST CHART
NATIONAL BUREAU OF STANDARDS-1963-A

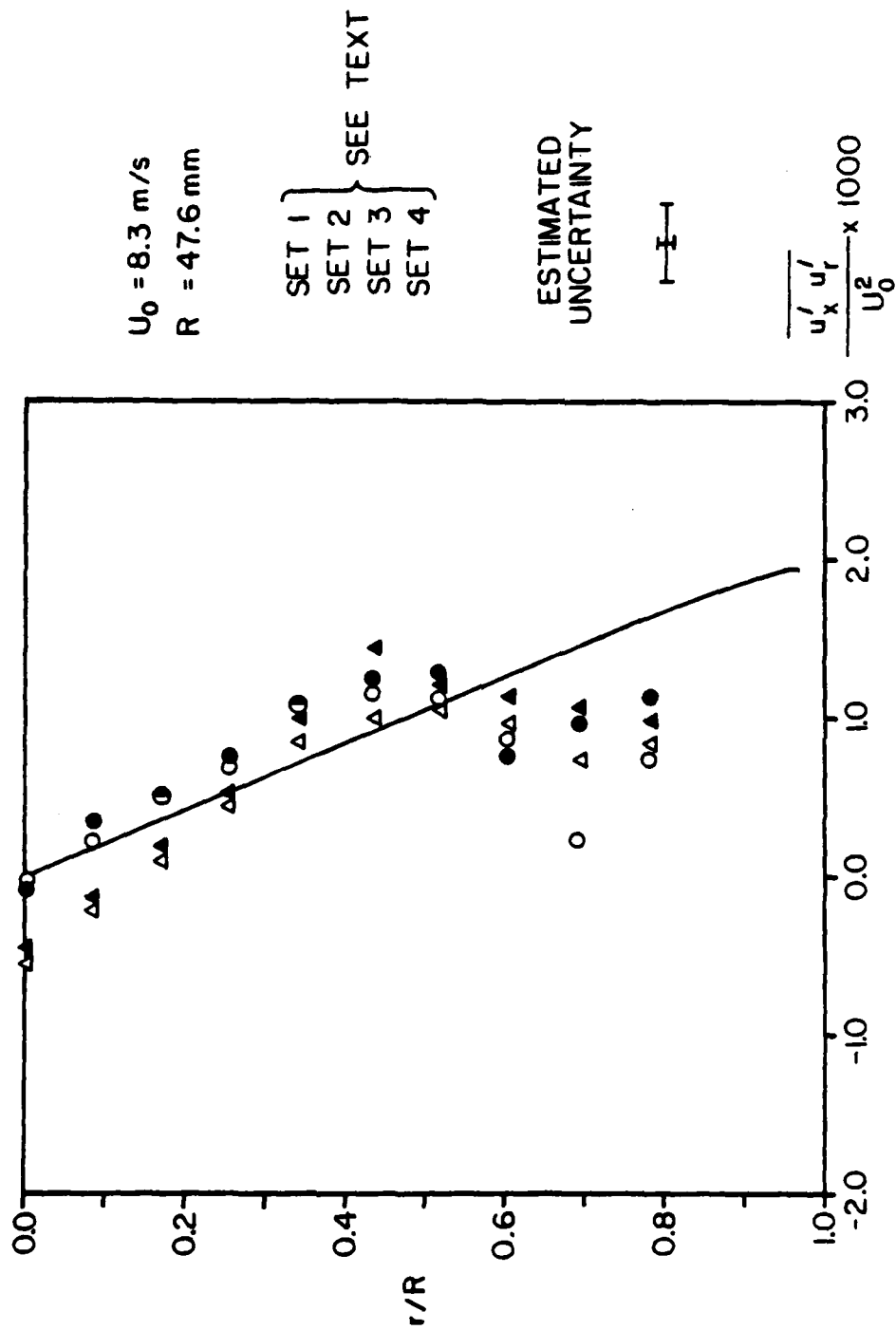


Figure 17. Measured Reynolds Stress Profile in the Turbulent Pipe Flow

the estimated uncertainty of the measurements, and all four sets follow a similar trend in their disagreement with the theoretical distribution. Barbin and Jones [34] showed in their measurements that the shear stress profile was not fully developed at $x/D = 40$; instead the Reynolds stresses near the wall were higher than the steady state values and those near the center of the pipe were lower. The present data do not show these trends and the reason for this difference is unknown.

3. SUDDEN EXPANSION FLOWFIELD ($R_2/R_1=1.90$)

As mentioned previously, the majority of the data taken for this investigation were obtained in the axisymmetric sudden expansion flow geometry with a diameter ratio of 1.90:1. This geometry was chosen because it had been used in a previous investigation at this facility and the nozzle was available.

a. MEAN VELOCITY MEASUREMENTS

Because the test section flange prevented optical access for the first 1.75 step heights beyond the nozzle outlet, the inlet velocity profile at the nozzle exit was measured with a pitot probe. Figure 18 shows the inlet velocity profile. The profile is flat across the width of the nozzle with a boundary layer that is approximately 1.2

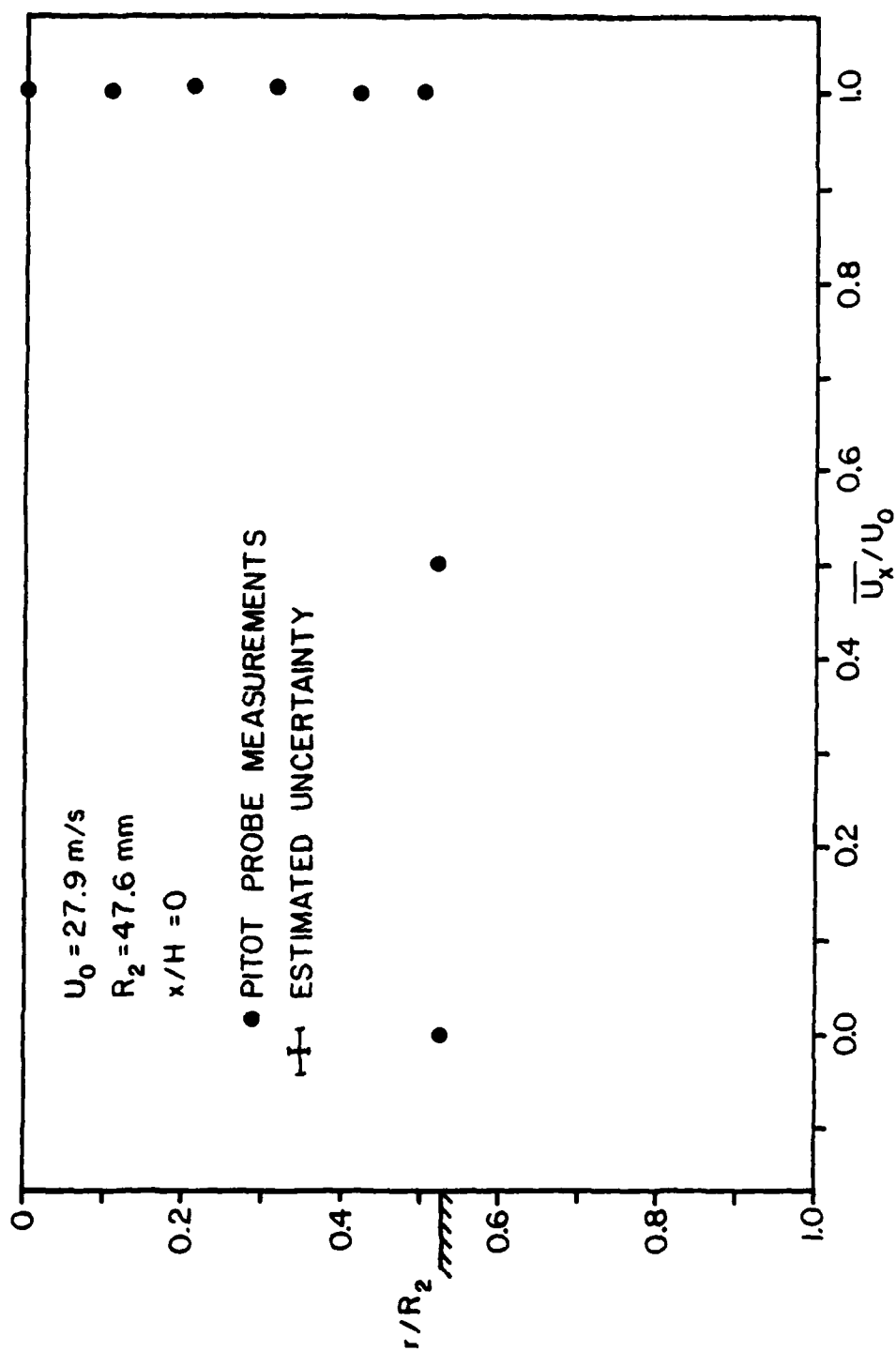


Figure 18. Measured Axial Mean Velocity Profile at Inlet of 1.90:1 Sudden Expansion

mm thick. This allowed the inlet mass flow rate to be easily calculated. This flat or "slug" flow profile was also used as an inlet boundary condition for the numerical prediction code to be described later.

Figures 19 through 24 show the axial mean velocity profiles measured with the LDV at 2, 4, 6, 8, 12, and 20 step heights downstream of the nozzle exit. The estimated uncertainty in the experimental data is shown in the figures. A discussion of how this uncertainty estimate was obtained is given in Appendix C. Also shown in each figure for comparison are the velocities predicted by the CHAMPION 2/E/FIX computer code of Pun and Spalding [35]. The comparison of the experimental and numerical profiles will be discussed later.

The profiles at 2, 4, and 6 step heights show the flat velocity profile across the potential core region. The width of the core region continually diminishes in the axial direction and has disappeared at the 8th step height.

In the recirculation zone, the maximum measured recirculation velocity was -3.4 m/s (12% of the inlet velocity) at 4 step heights and a radius of 45.0 mm (2.6 mm from the wall). That result is in good agreement with most other work. [5,12,13,17]

For the profile at $x/h = 20$, Figure 24, a $1/7$ power law curve scaled to match the inlet mass flux is shown to give

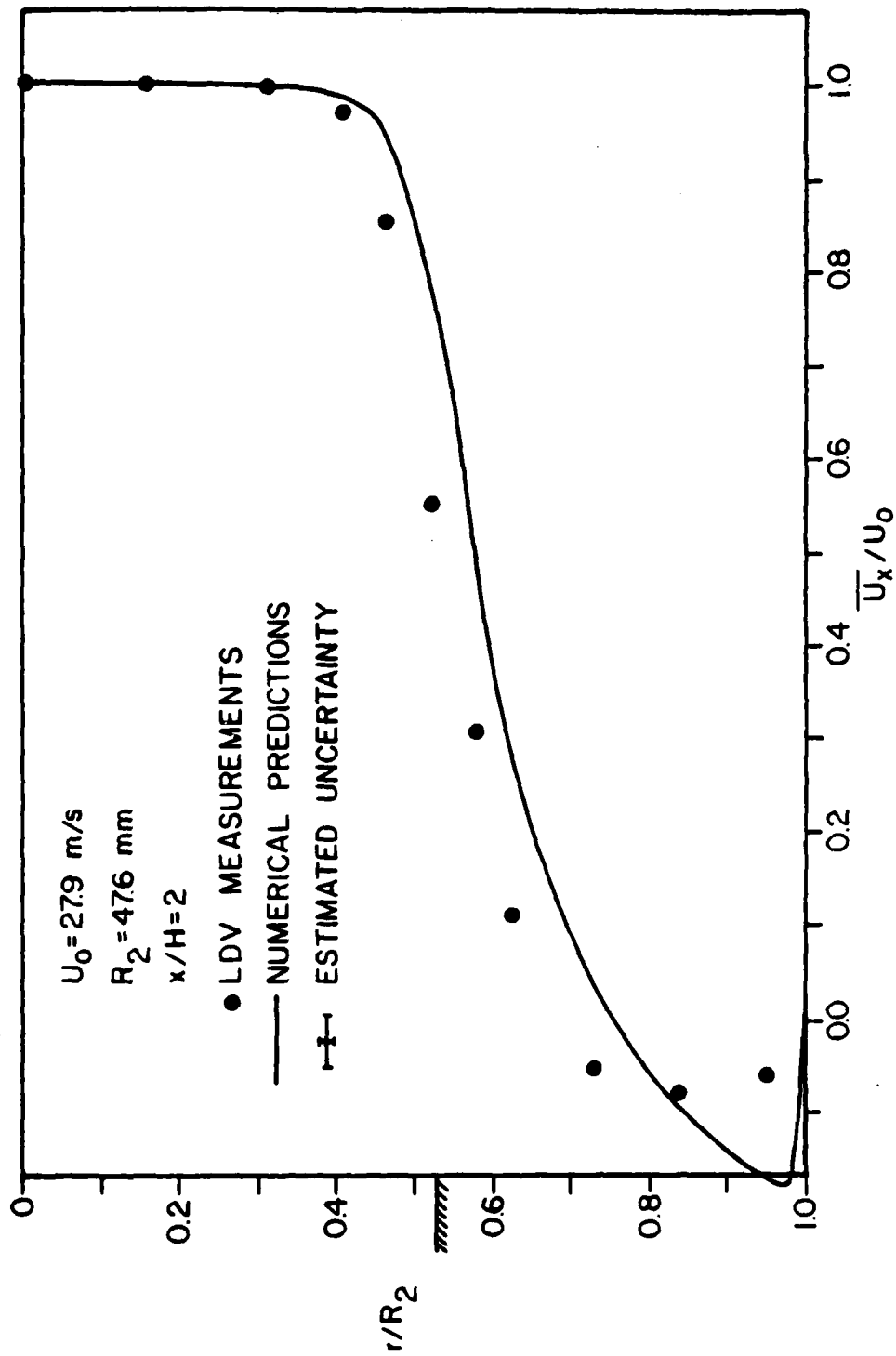


Figure 19. Predicted and Measured Axial Mean Velocity Profile in the 1.90:1 Sudden Expansion at $x/H = 2$

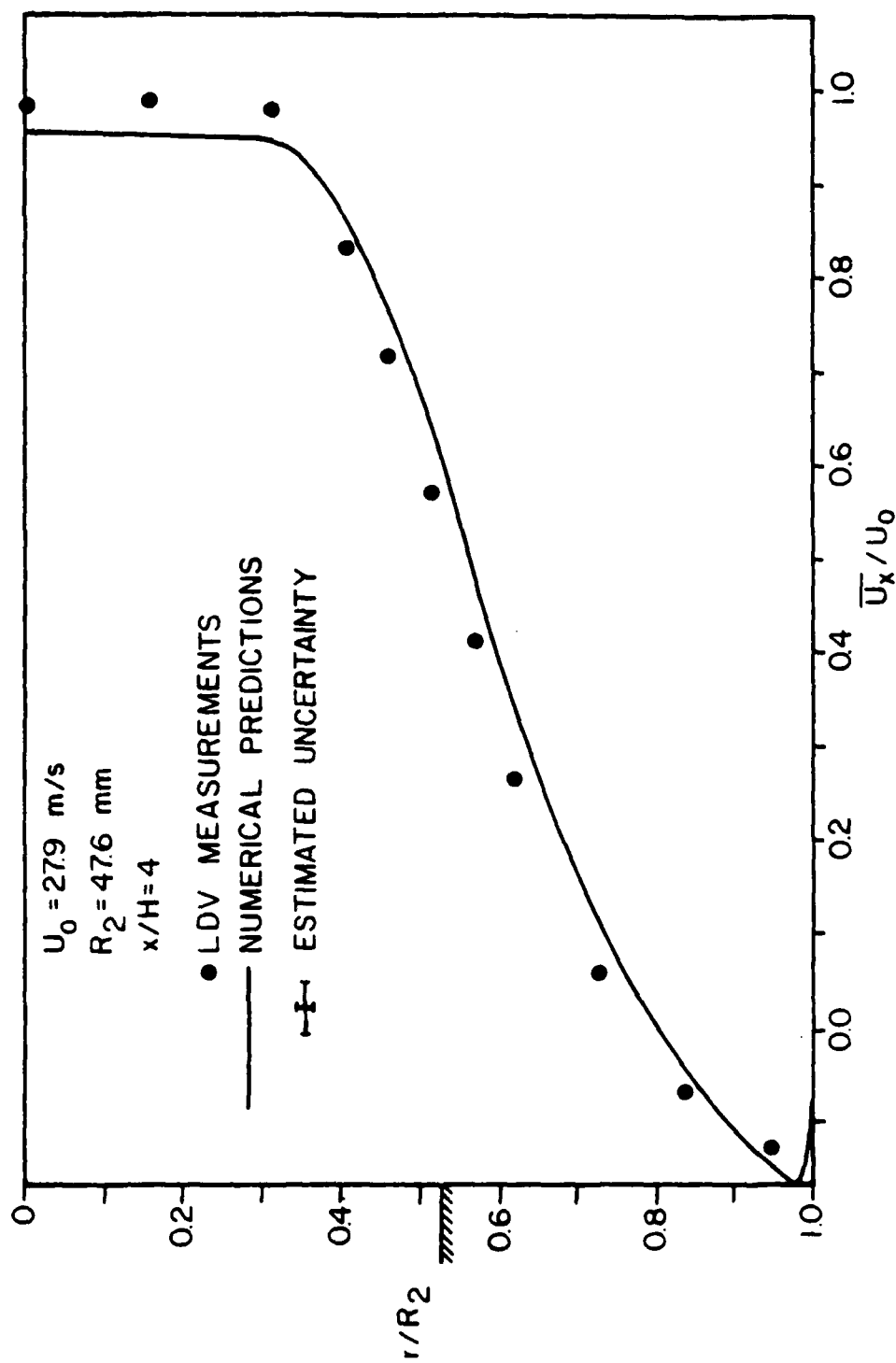


Figure 20. Predicted and Measured Axial Mean Velocity Profile in the 1.90:1 Sudden Expansion at $x/H = 4$

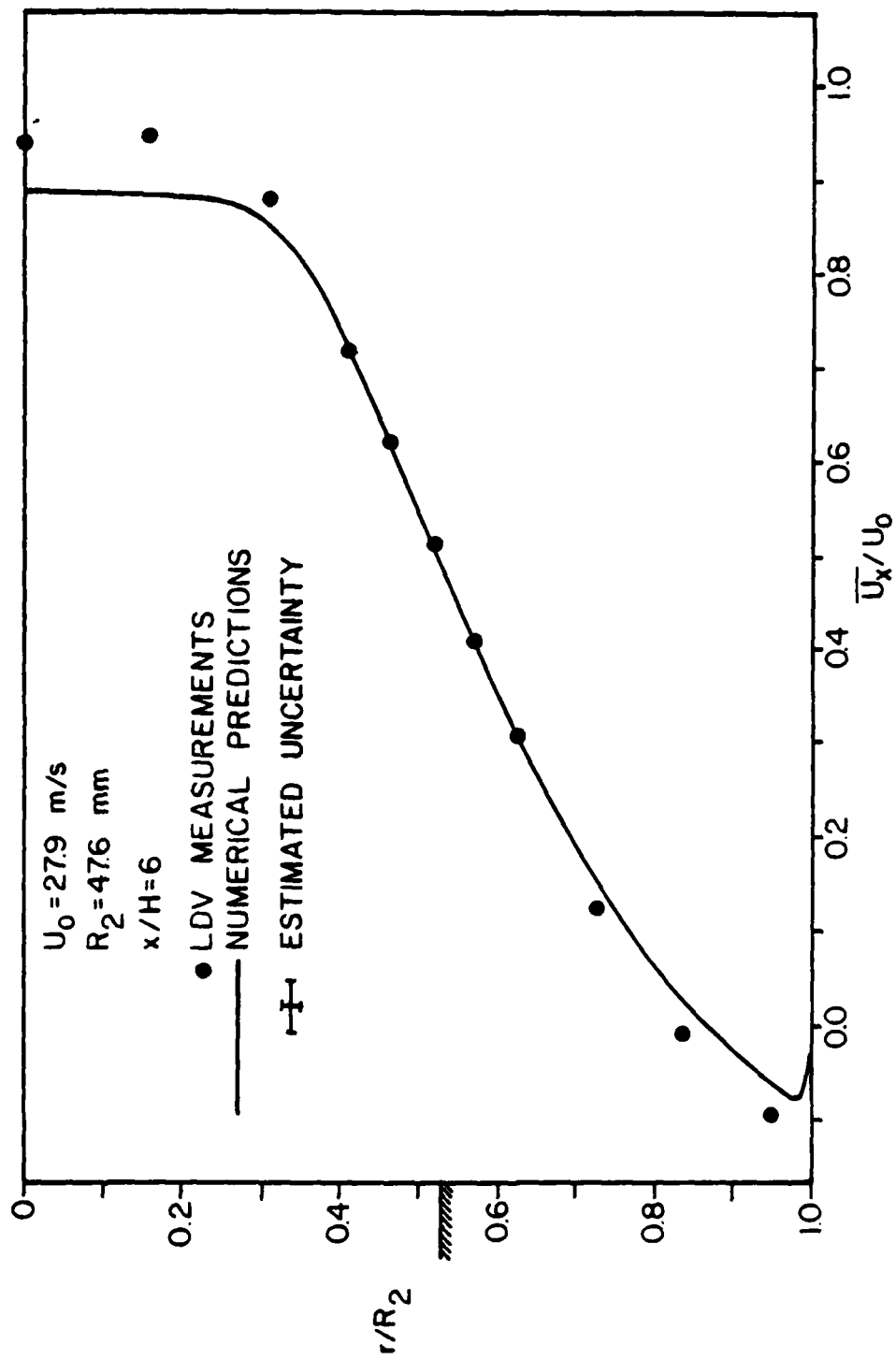


Figure 21. Predicted and Measured Axial Mean Velocity Profile in the 1.90:1 Sudden Expansion at $x/H = 6$

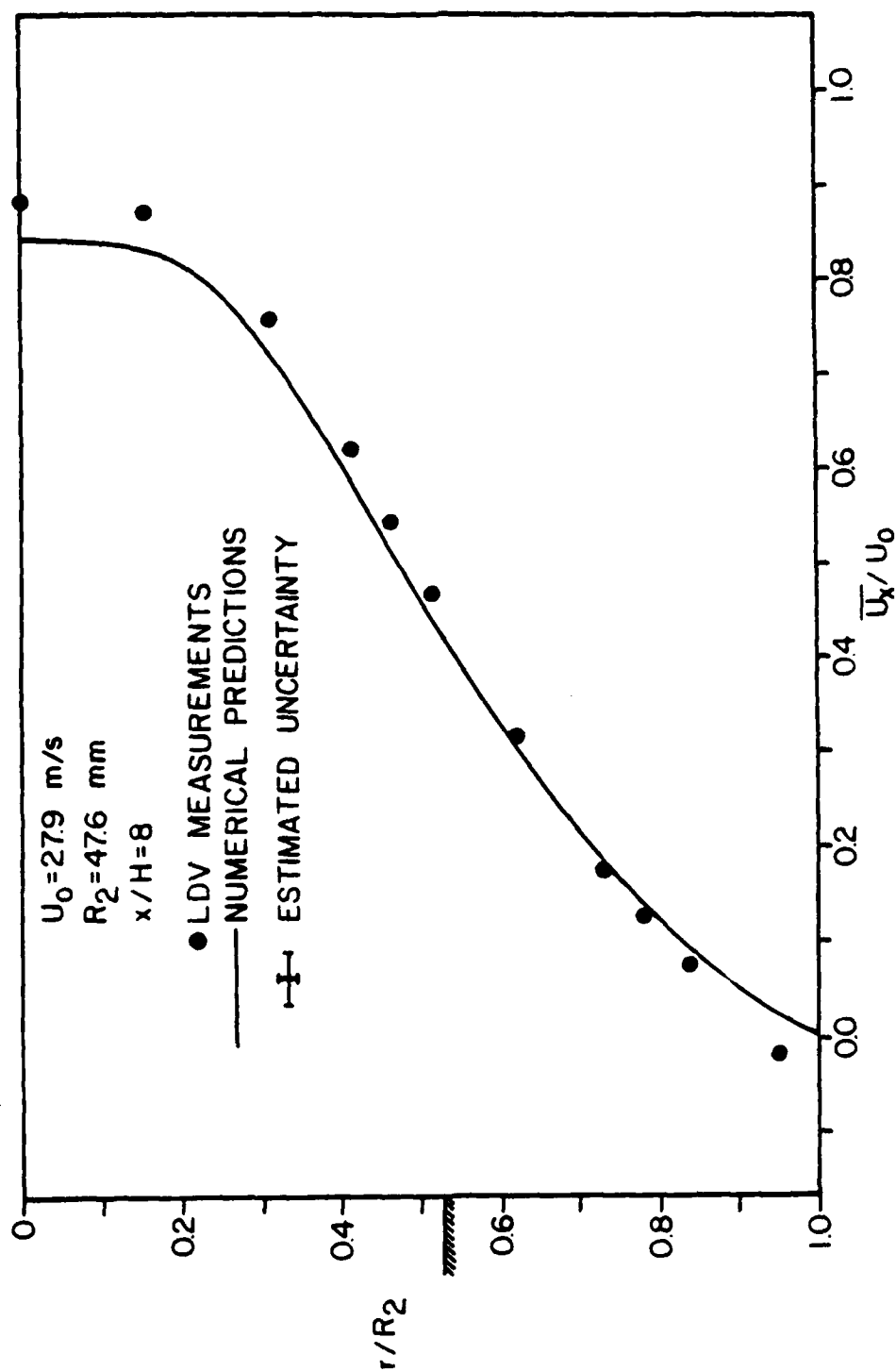


Figure 22. Predicted and Measured Axial Mean Velocity Profile in the 1.90:1 Sudden Expansion at $x/H = 8$

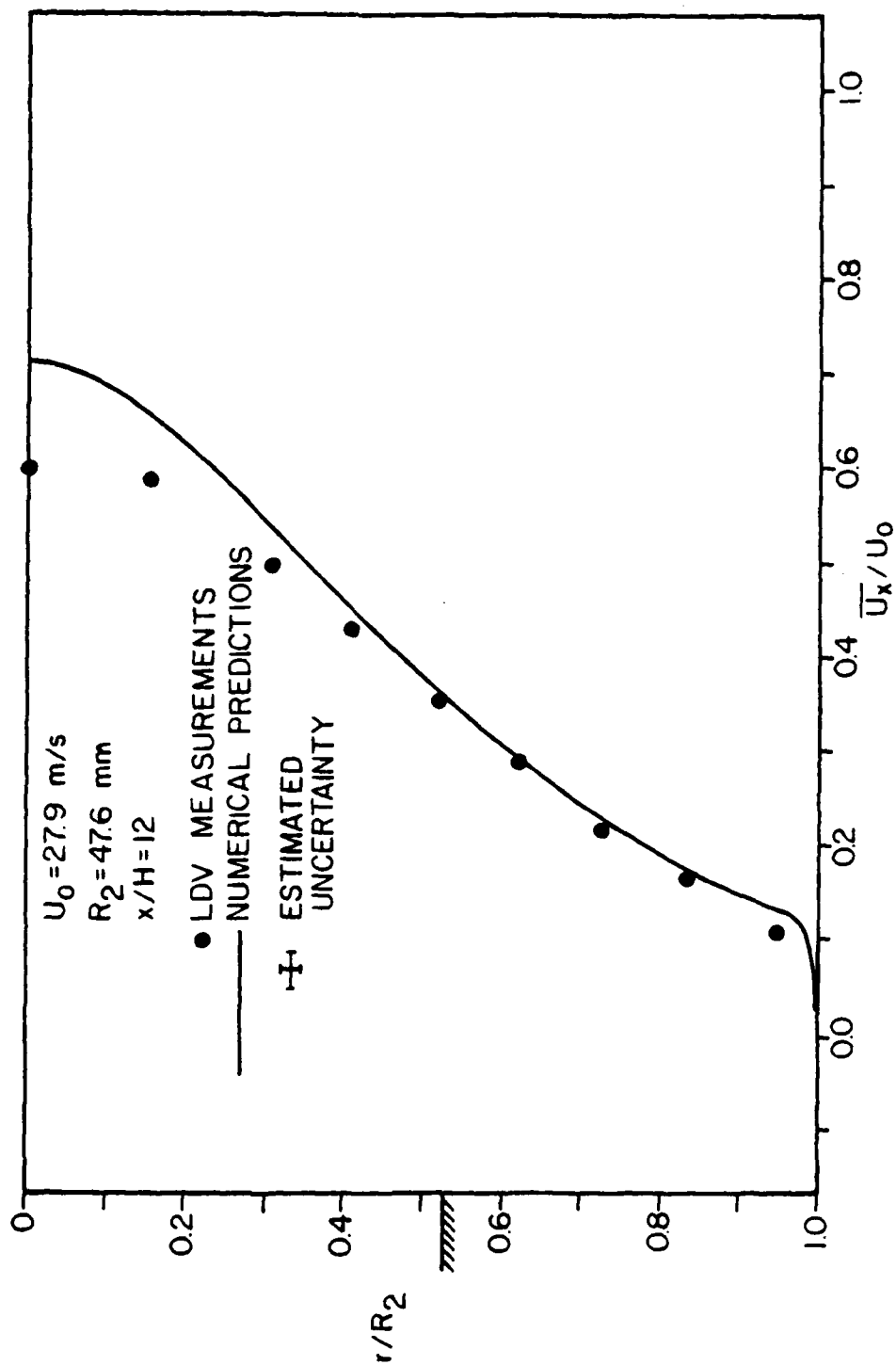


Figure 23. Predicted and Measured Axial Mean Velocity Profile in the 1.90:1 Sudden Expansion at $x/H = 12$

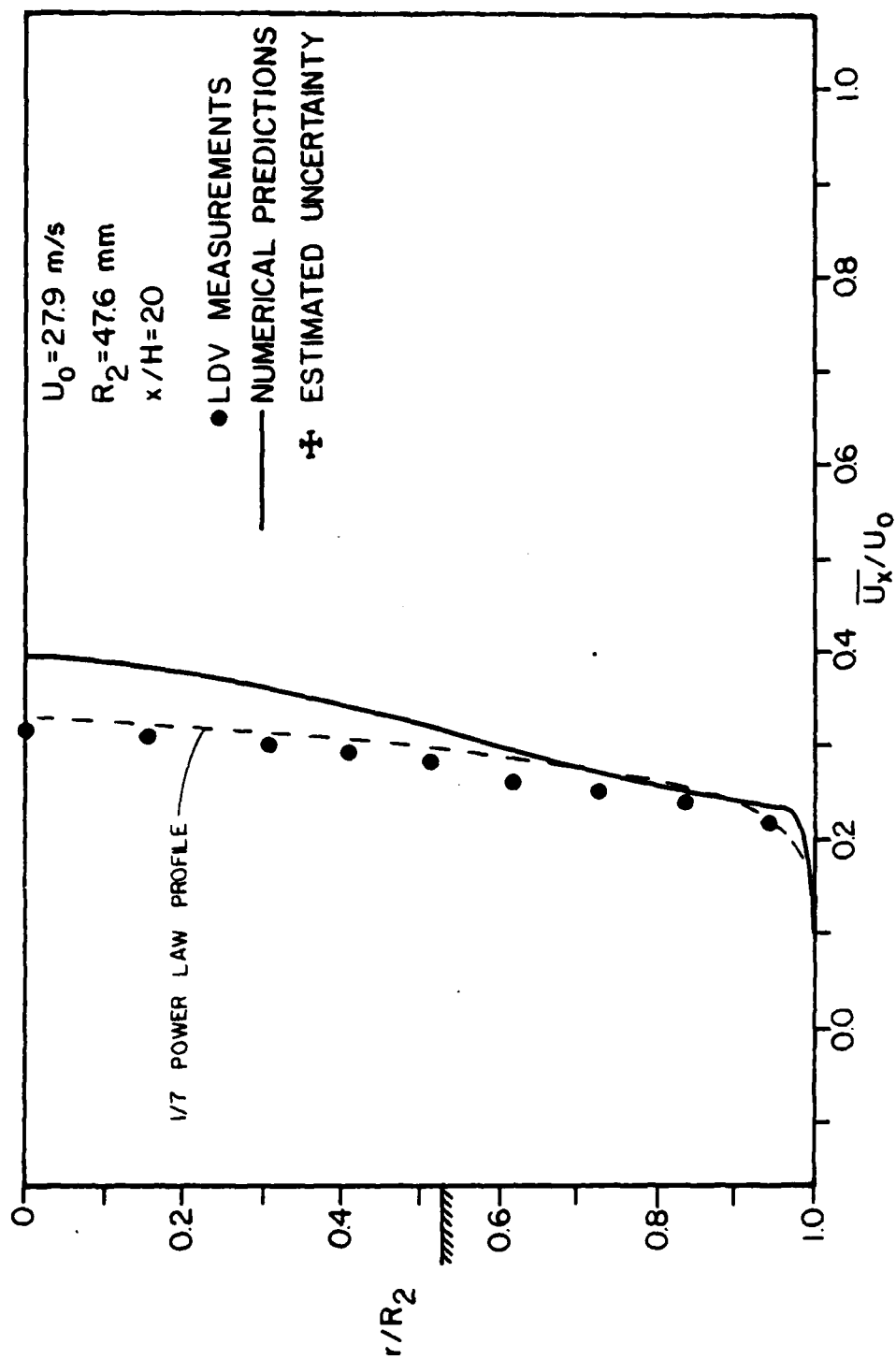


Figure 24. Predicted and Measured Axial Mean Velocity Profile in the 1.90:1 Sudden Expansion at $x/H = 20$

an idea of how close the flow is to redevelopment. By comparing the profiles at 8, 12, and 20 step heights, it is seen that the flow relaxes rather quickly through this region. After 20 step heights, the relaxation is probably much slower; Eaton & Johnston [36] predict that the flow will not be fully redeveloped until at least 50 step heights downstream of the expansion.

As an accuracy check, the measured velocity profiles were used to calculate the mass flow rate at each axial location. Table 6 shows the integrated mass flux at each location normalized with the inlet mass flux. Mass flow is conserved at all locations to within $\pm 3\%$. This agreement is similar to that obtained by Stevenson, et al. [5] for unbiased data and is probably as good as can be expected since the discrepancies in the mass flux are the same as the uncertainty in the mean velocity measurements.

The centerline velocity decay measured in this study is shown in Figure 25 along with the data of Stevenson, et al. [17], Moon & Rudinger [12], and Freeman [14]. The data shows very good agreement with all of the previous data when plotted as a function of downstream distance normalized with step height. This agreement is in spite of the fact that the expansion (diameter) ratios differed by as much as a factor of two and the inlet velocity profiles differed. This figure also shows the rapid relaxation of the flow through the region between 8 and 20 step heights, and that

TABLE 6. Integrated Mass Flux in the
Axisymmetric Sudden Expansion

| x/H | \dot{m}/\dot{m}_{ref} |
|-------|-------------------------|
| 0 | 1.00* |
| 2 | 0.98 |
| 4 | 1.04 |
| 6 | 1.04 |
| 8 | 1.00 |
| 12 | 1.03 |
| 20 | 0.98 |

* \dot{m}_{ref} based on inlet velocity profile at $x/H = 0$

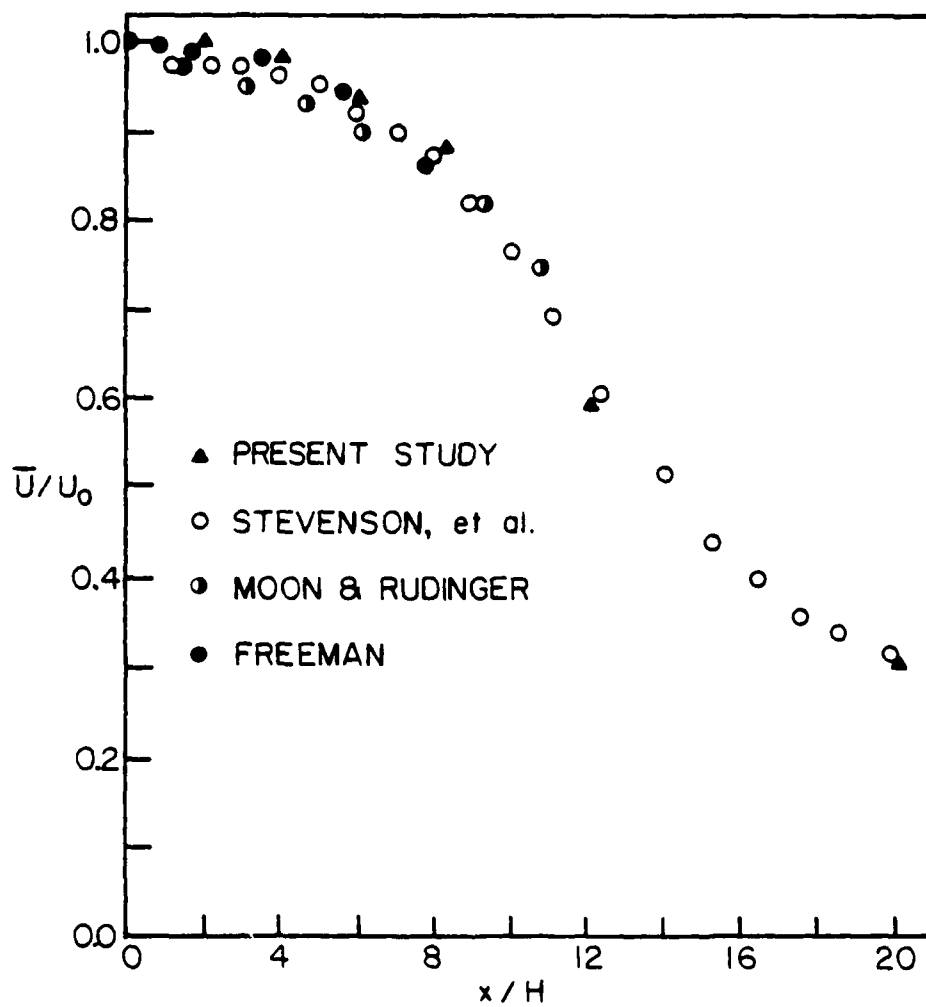


Figure 25. Measured Mean Centerline Velocity Decay

the rate of relaxation has tapered off at 20 step heights.

Figures 26 through 31 show the radial mean velocity profiles measured at $x/H = 2, 4, 6, 8, 12,$ and 20 . The numerical predictions from the 2/E/FIX code are also shown for comparison. It is immediately evident in these plots that the relative uncertainty is higher in the radial velocity measurements. This scatter is mainly due to the relatively low values of the radial mean velocity in relation to the radial fluctuation velocity. For nearly all of these measurements, the local radial turbulence intensity, i.e.,

$\overline{u_r'^2}/\overline{U_r}$, is several hundred percent. Another factor that was of importance in these measurements, especially in the potential core region of the flow, is that the axial velocity is much greater than the radial velocity. When this is the case, any small misalignment of the probe volume orientation with respect to the axis of the tube will introduce a component of the axial velocity into the measurement. Since the radial velocities are very low, this component of the axial velocity can easily be of the same order as the radial velocity. This misalignment is probably the main reason that the centerline radial velocities at 2, 4, 6, and 8 step heights are not zero. Because of the limits of the correction lens that were previously discussed, radial velocity measurements were not possible as close to the walls as axial measurements were. However, in the region near the wall, the radial velocities are probably small.

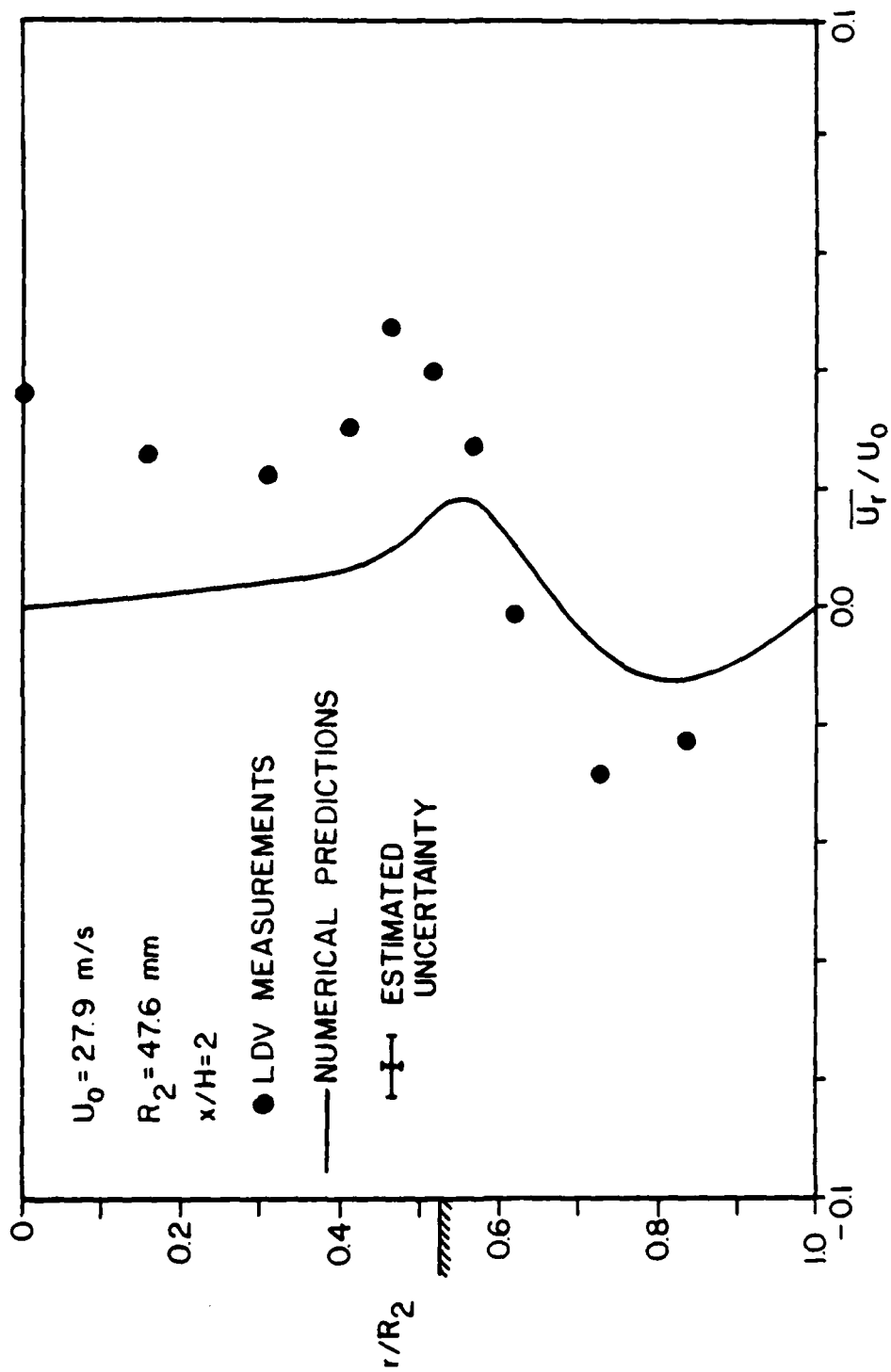


Figure 26. Predicted and Measured Radial Mean Velocity Profile in the 1.90:1 Sudden Expansion at $x/H = 2$

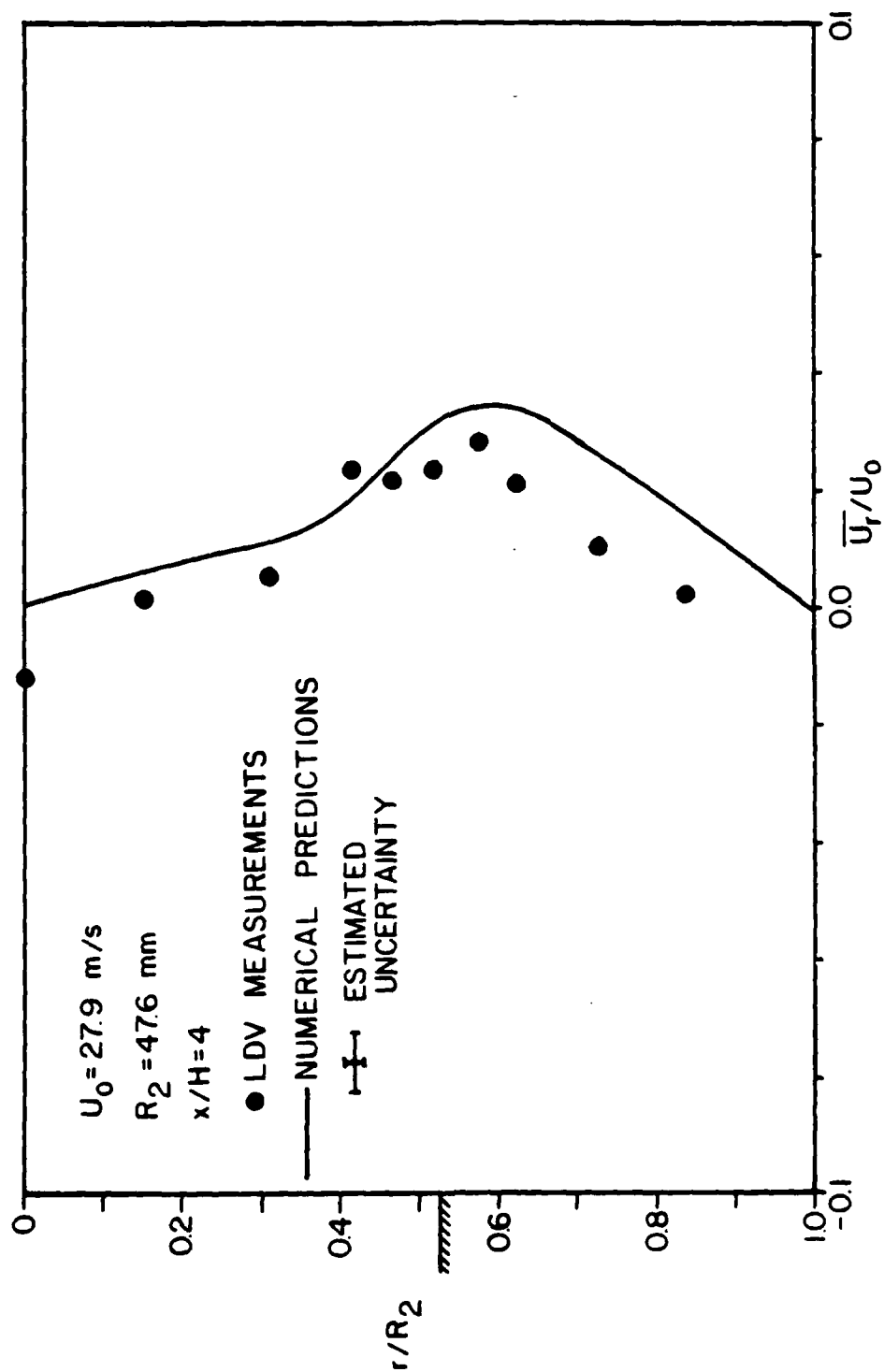


Figure 27. Predicted and Measured Radial Mean Velocity Profile in the 1.90:1 Sudden Expansion at $x/H = 4$

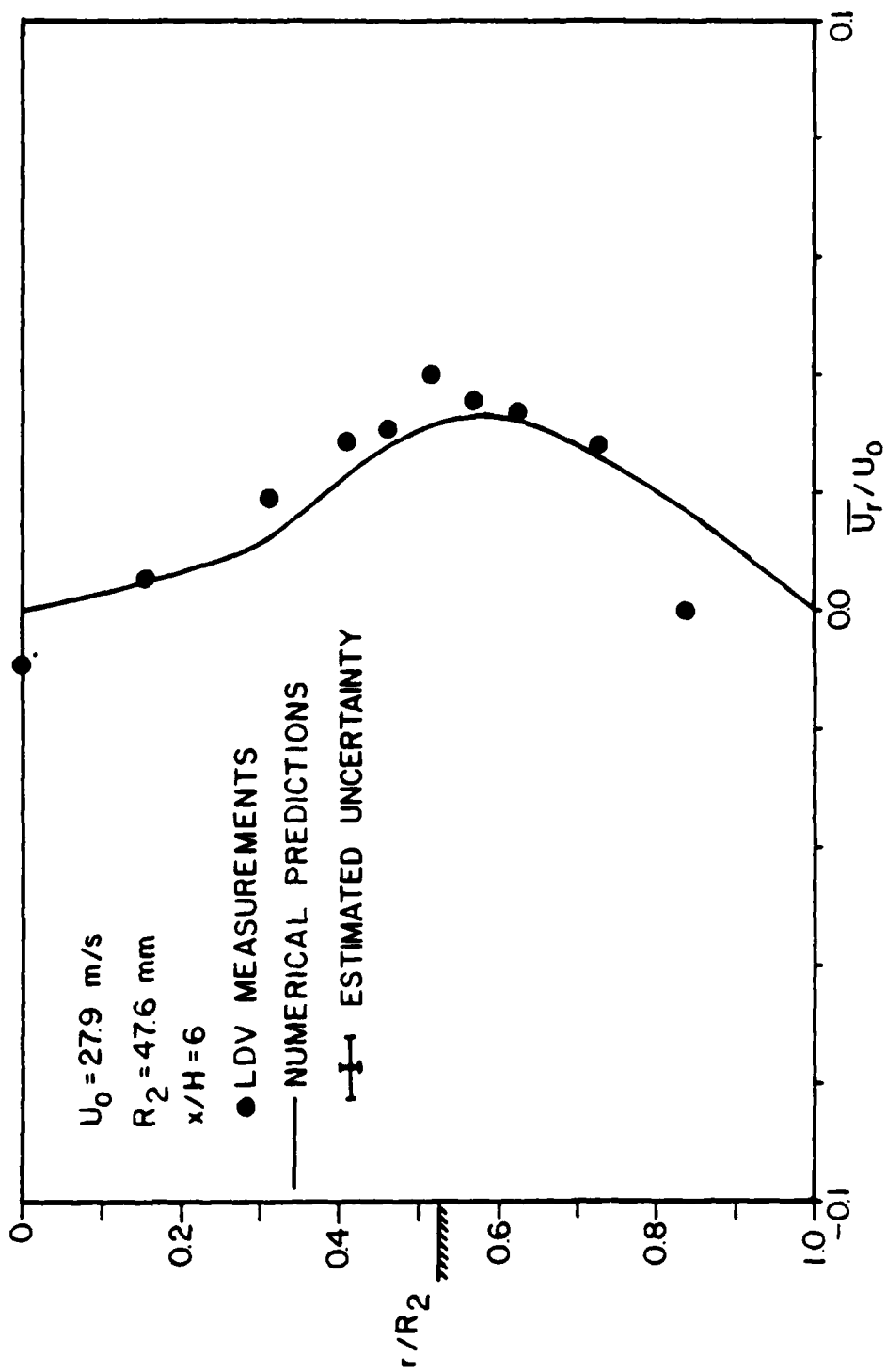


Figure 28. Predicted and Measured Radial Mean Velocity Profile in the 1.90:1 Sudden Expansion at $x/H = 6$

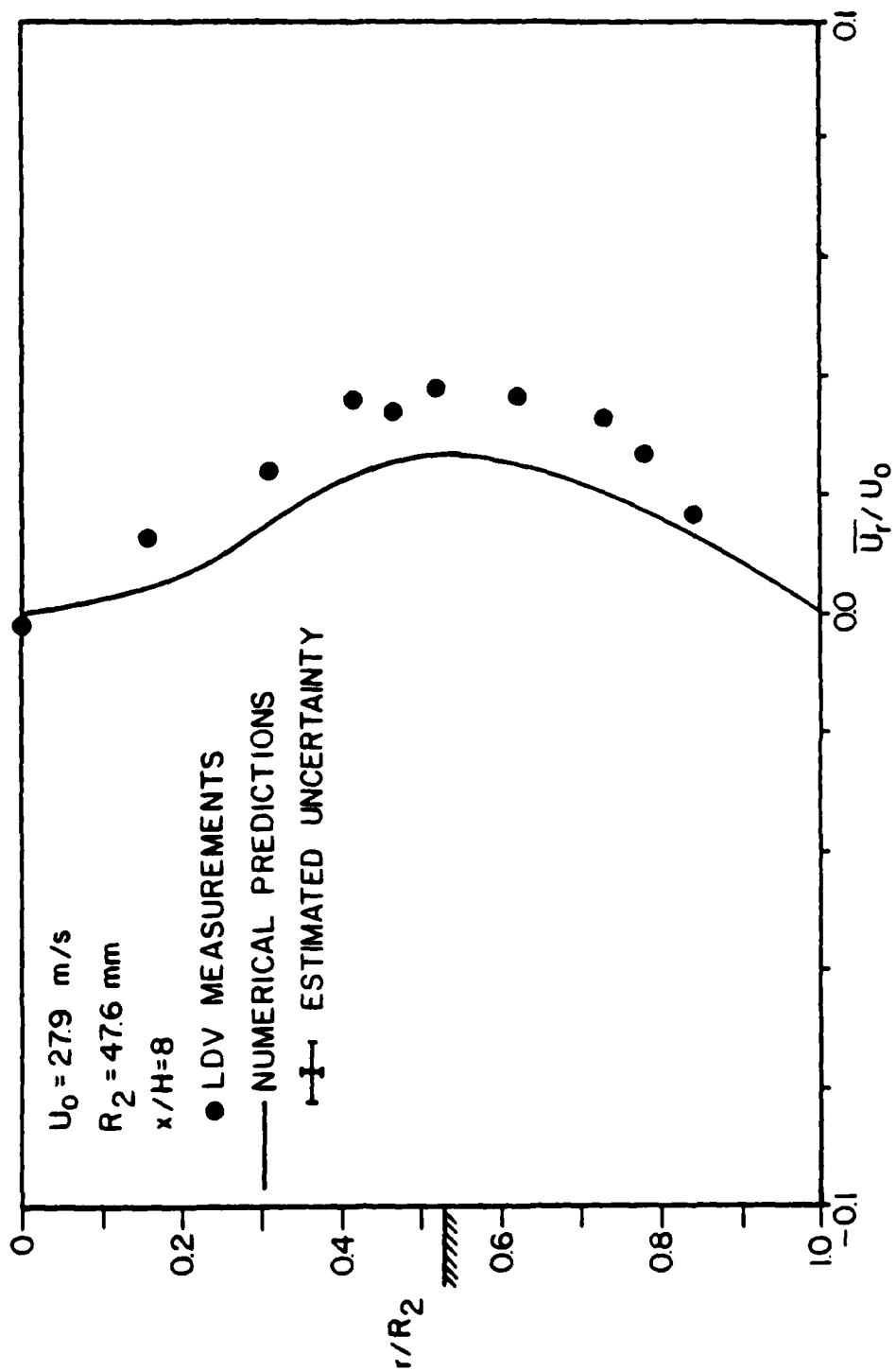


Figure 29. Predicted and Measured Radial Mean Velocity Profile in the 1.90:1 Sudden Expansion at $x/H = 8$

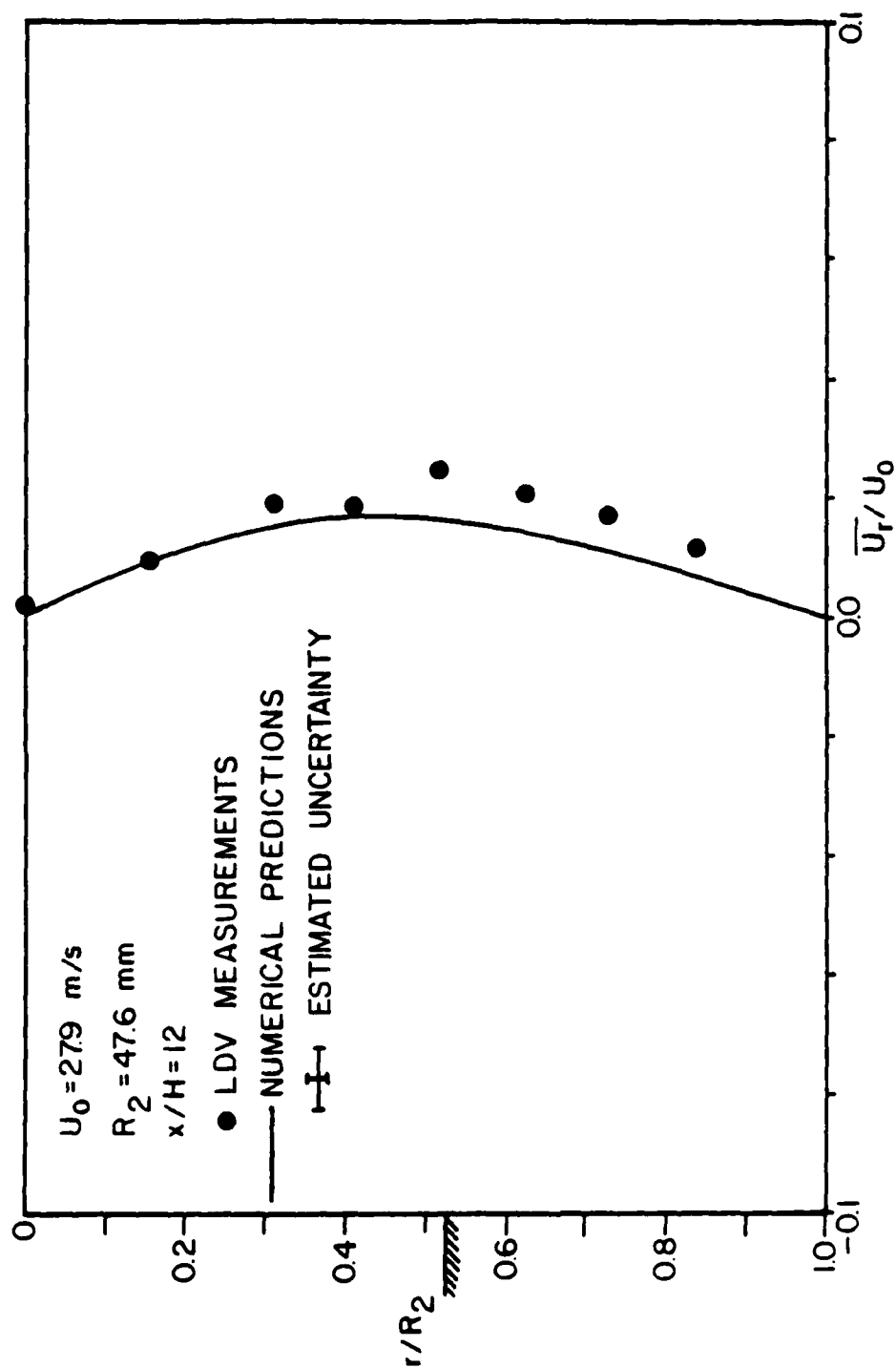


Figure 30. Predicted and Measured Radial Mean Velocity Profile in the 1.90:1 Sudden Expansion at $x/H = 12$

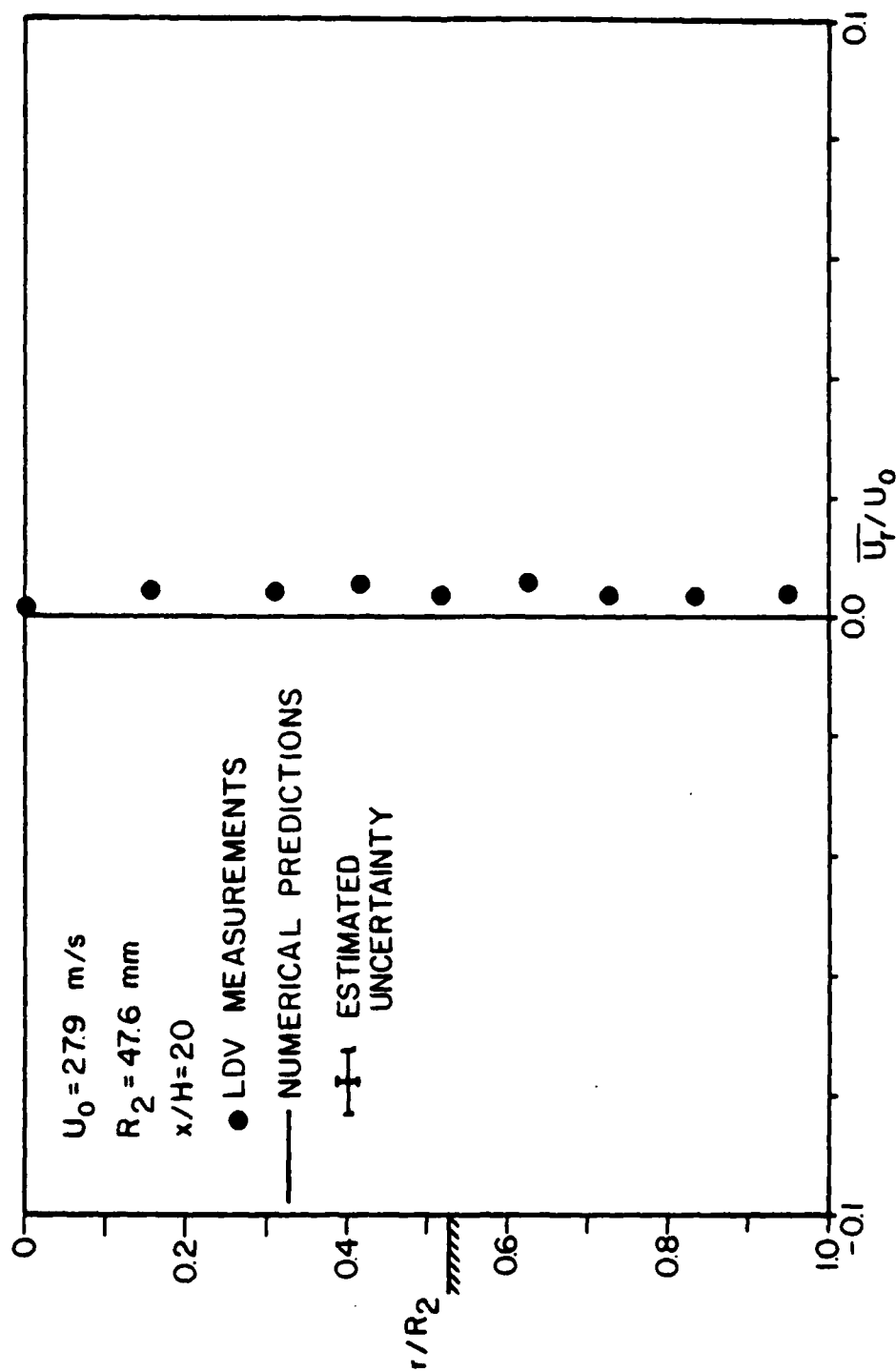


Figure 31. Predicted and Measured Radial Mean Velocity Profile in the 1.90:1 Sudden Expansion at $x/H = 20$

b. TURBULENCE PARAMETERS

Four separate measurements of turbulence intensity were made at each point in the flow field. The measurements were made at probe volume orientations of 0, +45, -45, and 90 degrees with respect to the tube axis. From the four measurements the axial turbulence intensity, radial turbulence intensity, Reynolds stress, and turbulence kinetic energy were computed. No turbulence parameters were measured in the inlet "jet" flow since only pitot probe measurements were made at this location. By observing the measurements in the core region at $x/H = 2$ though, a good estimate would be that the inlet turbulence intensity is probably less than 2% of the mean flow for both the axial and radial directions.

Figures 32 through 37 show the turbulence kinetic energy profiles normalized with twice the inlet centerline velocity squared. Two values of kinetic energy are plotted at each radial location. The circular symbols represent a "partial" TKE consisting of only the axial and radial turbulence components. This is the quantity that was actually measured in this investigation and most of the 2-D sudden expansion data in the literature give values for this partial TKE. The triangular symbols are an approximation of the total TKE. These values were determined by assuming the tangential turbulence intensity to be approximately equal to the radial turbulence intensity. The values represented by

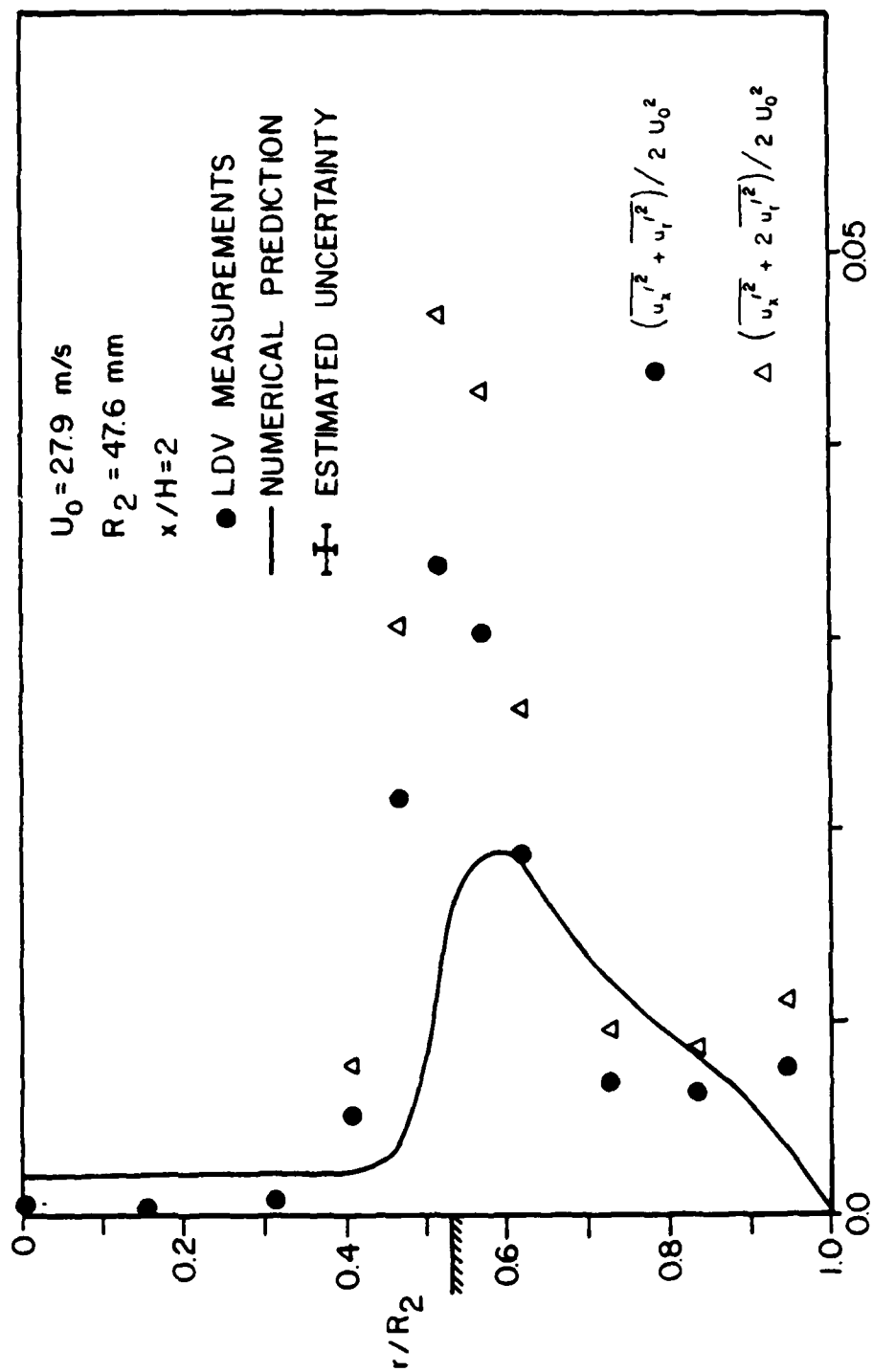


Figure 32. Predicted and Measured Turbulence Kinetic Energy Profile in the 1.90:1 Sudden Expansion at $x/H = 2$

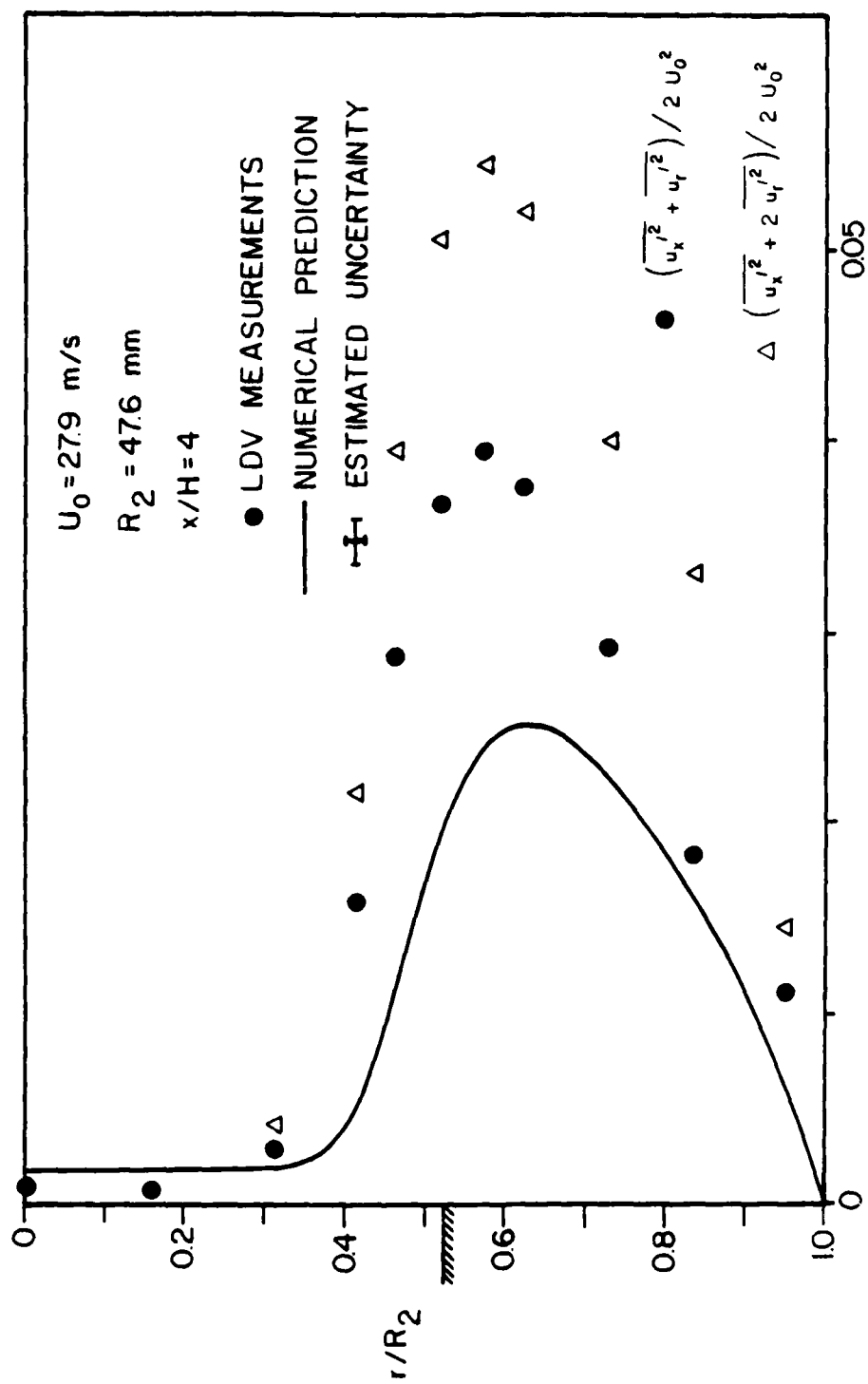


Figure 33. Predicted and Measured Turbulence Kinetic Energy Profile in the 1.90:1 Sudden Expansion at $x/H = 4$

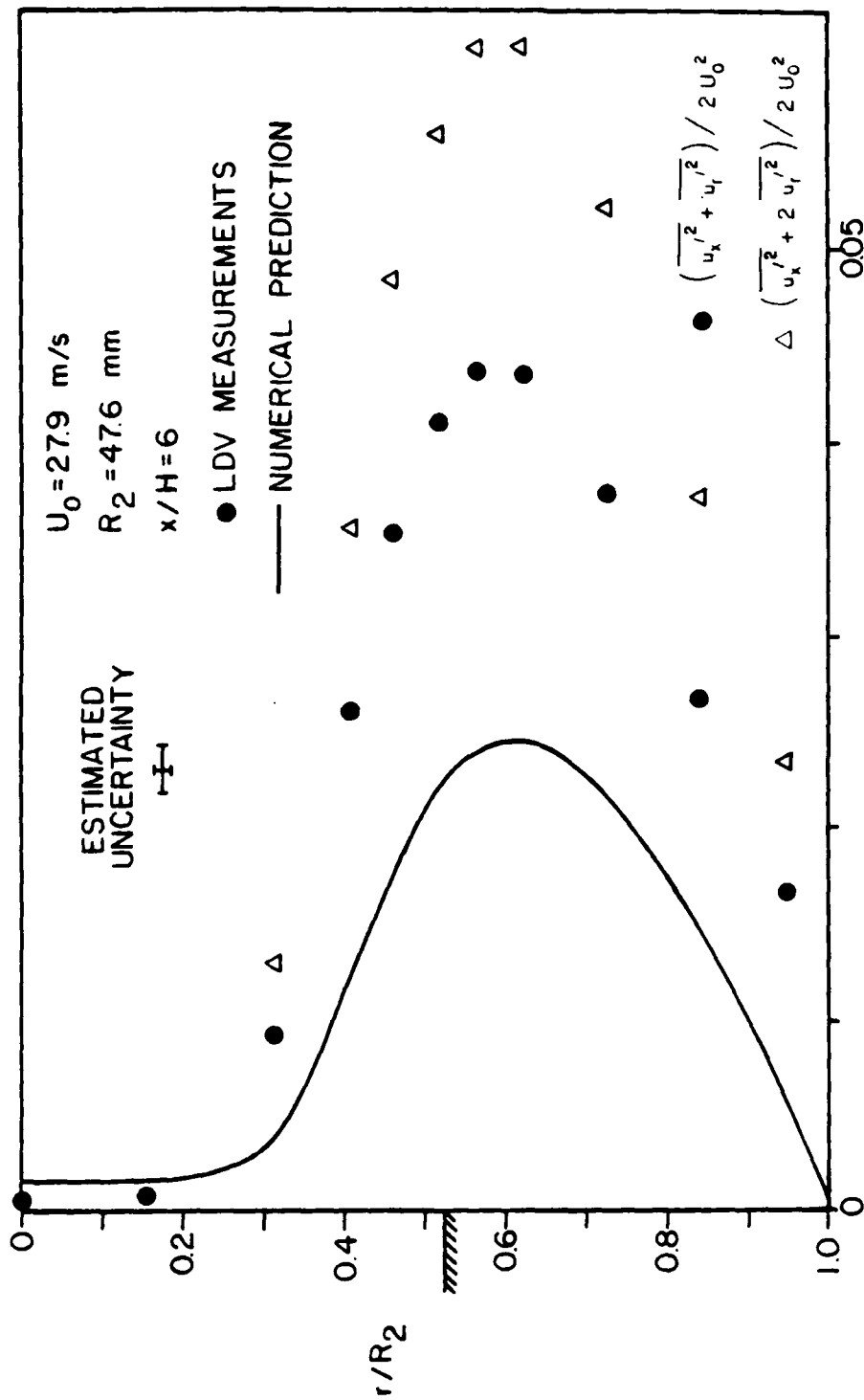


Figure 34. Predicted and Measured Turbulence Kinetic Energy Profile in the 1.90:1 Sudden Expansion at $x/H = 6$

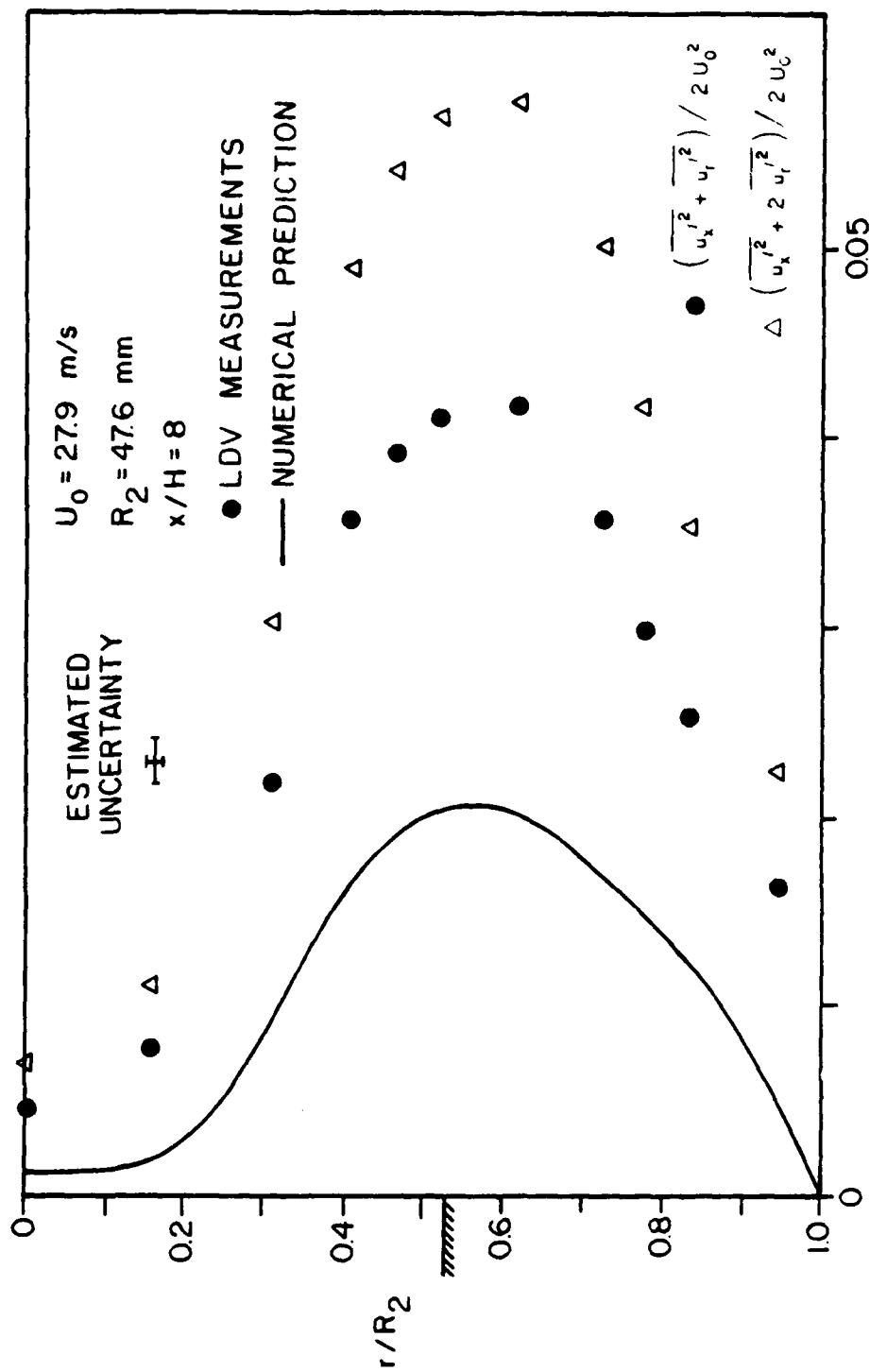


Figure 35. Predicted and Measured Turbulence Kinetic Energy Profile in the 1.90:1 Sudden Expansion at $x/H = 8$

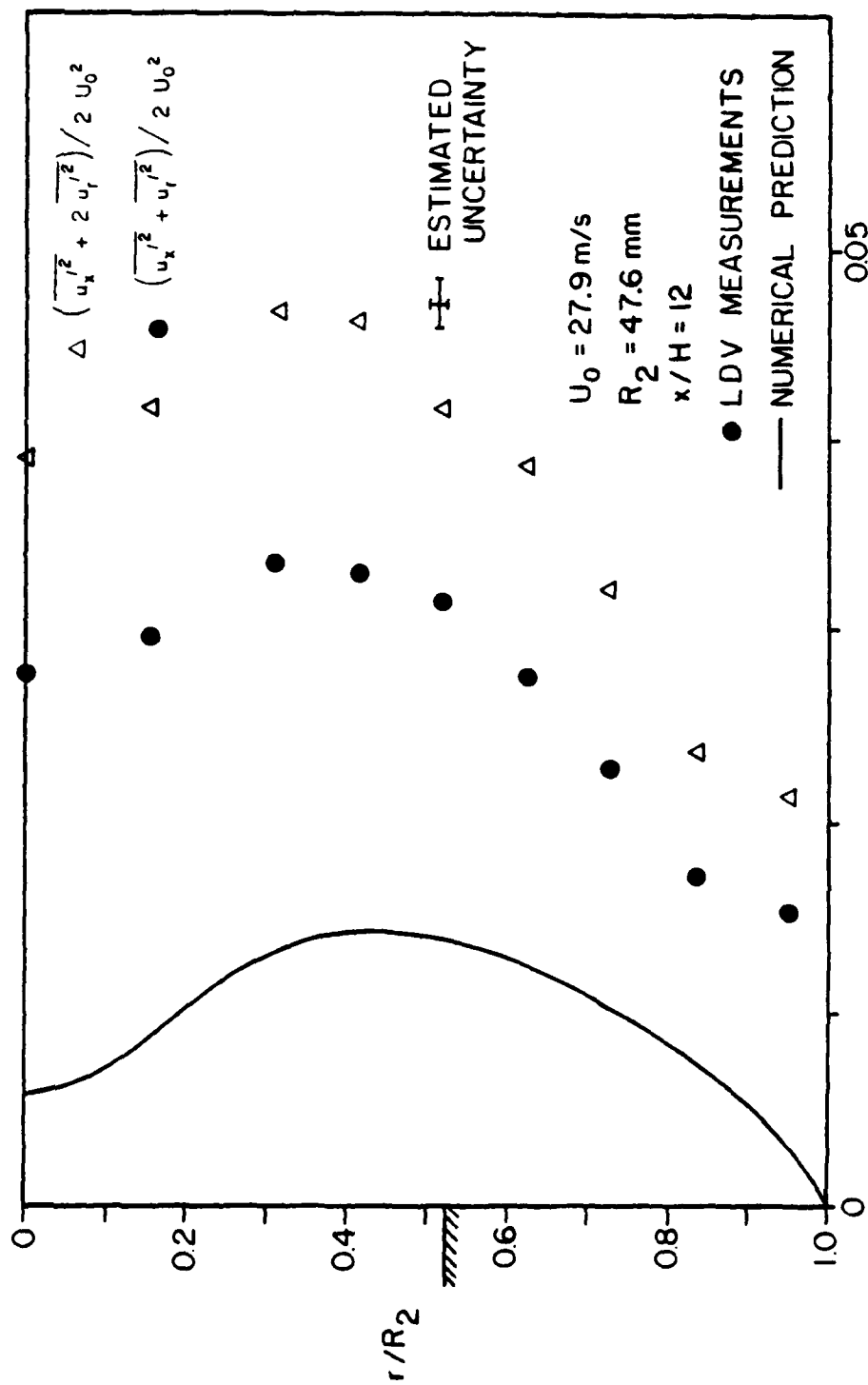


Figure 36. Predicted and Measured Turbulence Kinetic Energy Profile in the 1.90:1 Sudden Expansion at $x/H = 12$

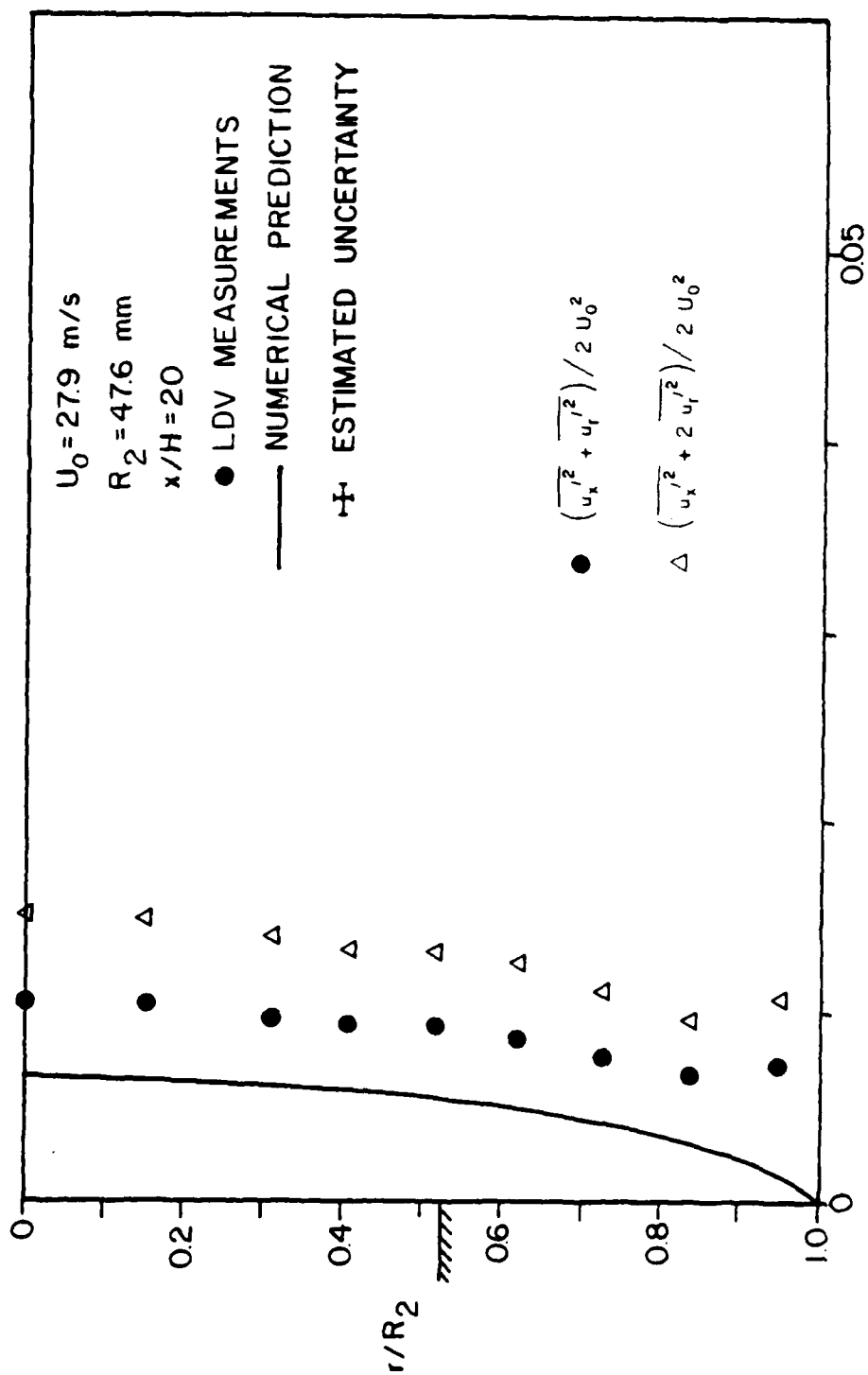


Figure 37. Predicted and Measured Turbulence Kinetic Energy Profile in the 1.90:1 Sudden Expansion at $x/H = 20$

the triangular figures then are $\overline{u'^2_x} + 2 \overline{u'^2_r}$. They are presented in order to provide a comparison to the numerical predictions.

The profiles at the first four locations all show a peak in the kinetic energy distribution which broadens as the mixing zone spreads in the downstream direction. By comparing these plots to the axial mean velocity profiles, it can be seen that the width of these peaks at each location is roughly equal to the width of the mixing layer region as would be expected. The peaks in the kinetic energy profiles identify the regions of highest shear and mixing. In the separated flow region, prior to reattachment, the location of this maximum coincides with the dividing streamline. As reattachment is approached, the location of the maximum moves out away from the wall and remains there as the boundary layer redevelops.

As discussed in Eaton and Johnston [36], the turbulence kinetic energy is seen to increase steadily through the separated region of the flow, similar to the characteristics of a free shear layer. After reattachment, the kinetic energy decreases rapidly as the flow redevelops. The maximum measured value of the normalized "partial" TKE in the flowfield was 0.043. Maximum values of the partial TKE measured in backward facing step flows are 0.031 obtained by Smyth [37], 0.025 obtained by Driver and Seegmiller [10], and 0.039 obtained by Bremner, et al. [3]. The only

turbulence kinetic energy measurement reported for an axisymmetric expansion was by Stevenson, et al. [17] who measured a value of 0.05 for the $\overline{u'^2_x} + \overline{u'^2_\theta}$ kinetic energy.

Downstream of the recirculation zone, the partial TKE profile flattens out and decreases to approximately 0.01 at $x/H = 20$. This value agrees well with the downstream kinetic energy profile measured by Luchik. Driver and Seegmiller and Smyth both found that the kinetic energy profile in a 2-D expansion was not flat at $x/H = 20$ and they measured maximum values of 0.006 and 0.015 respectively. Bremmer's measurements went only to $x/H = 9$ and could not be compared.

The turbulence kinetic energy measurements that are shown in Figures 32 through 37 were calculated from turbulence intensities measured in directions oriented at +45 and -45 degrees with respect to the axial direction as shown in Equation 10. TKE's were also calculated with the turbulence intensities measured in the axial and radial directions and these were found to agree to within the estimated uncertainty of the method.

Figures 38 through 43 show the axial and radial turbulence intensities normalized with the inlet centerline velocity and the Reynolds stresses normalized with the square of the inlet centerline velocity. Profiles are shown for the six axial locations at $x/H = 2, 4, 6, 8, 12,$ and 20 .

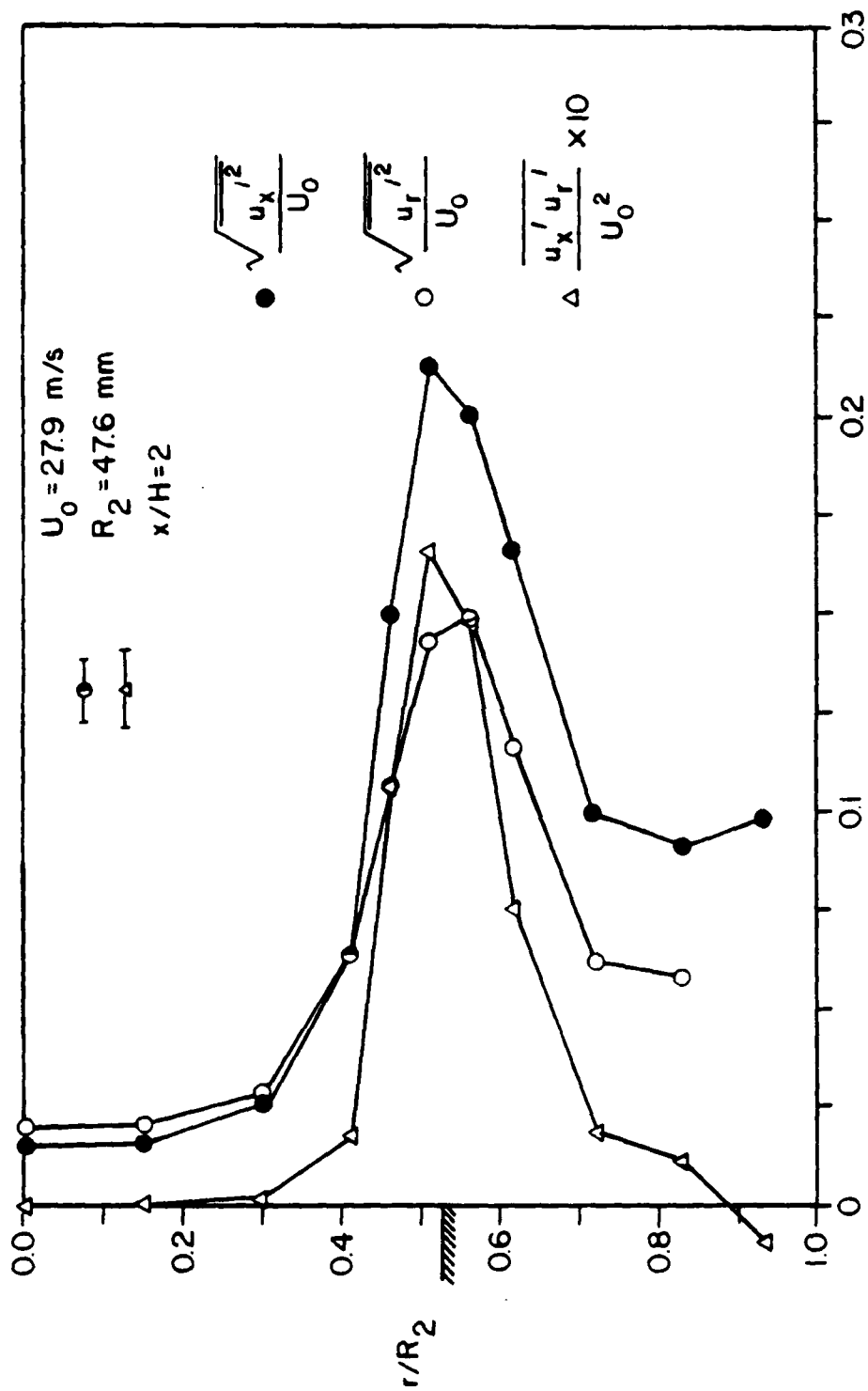


Figure 38. Measured Axial and Radial Turbulence Intensity and Reynolds Stress in the 1.90:1 Sudden Expansion at $x/H = 2$

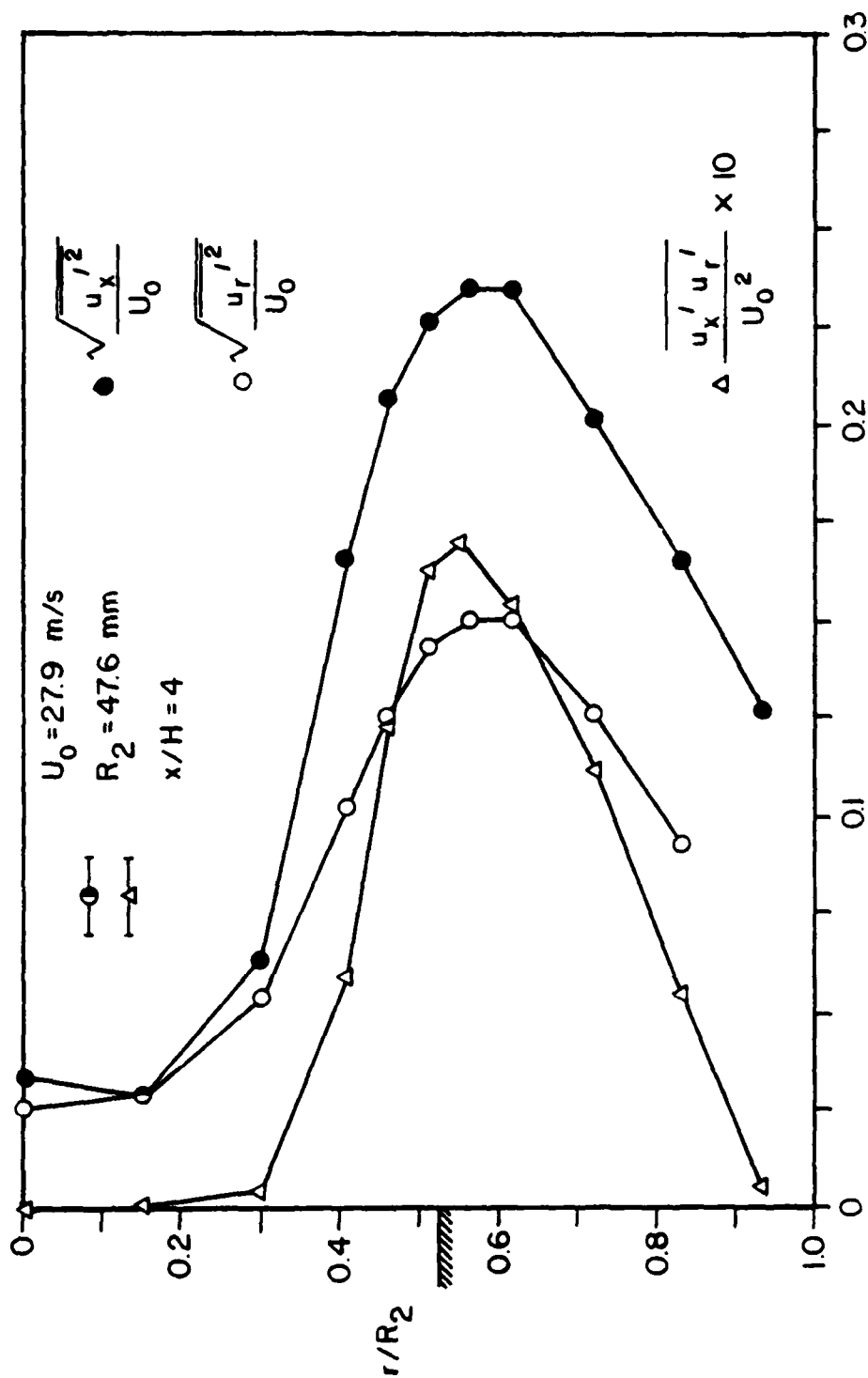


Figure 39. Measured Axial and Radial Turbulence Intensity and Reynolds Stress in the 1.90:1 Sudden Expansion at $x/H = 4$

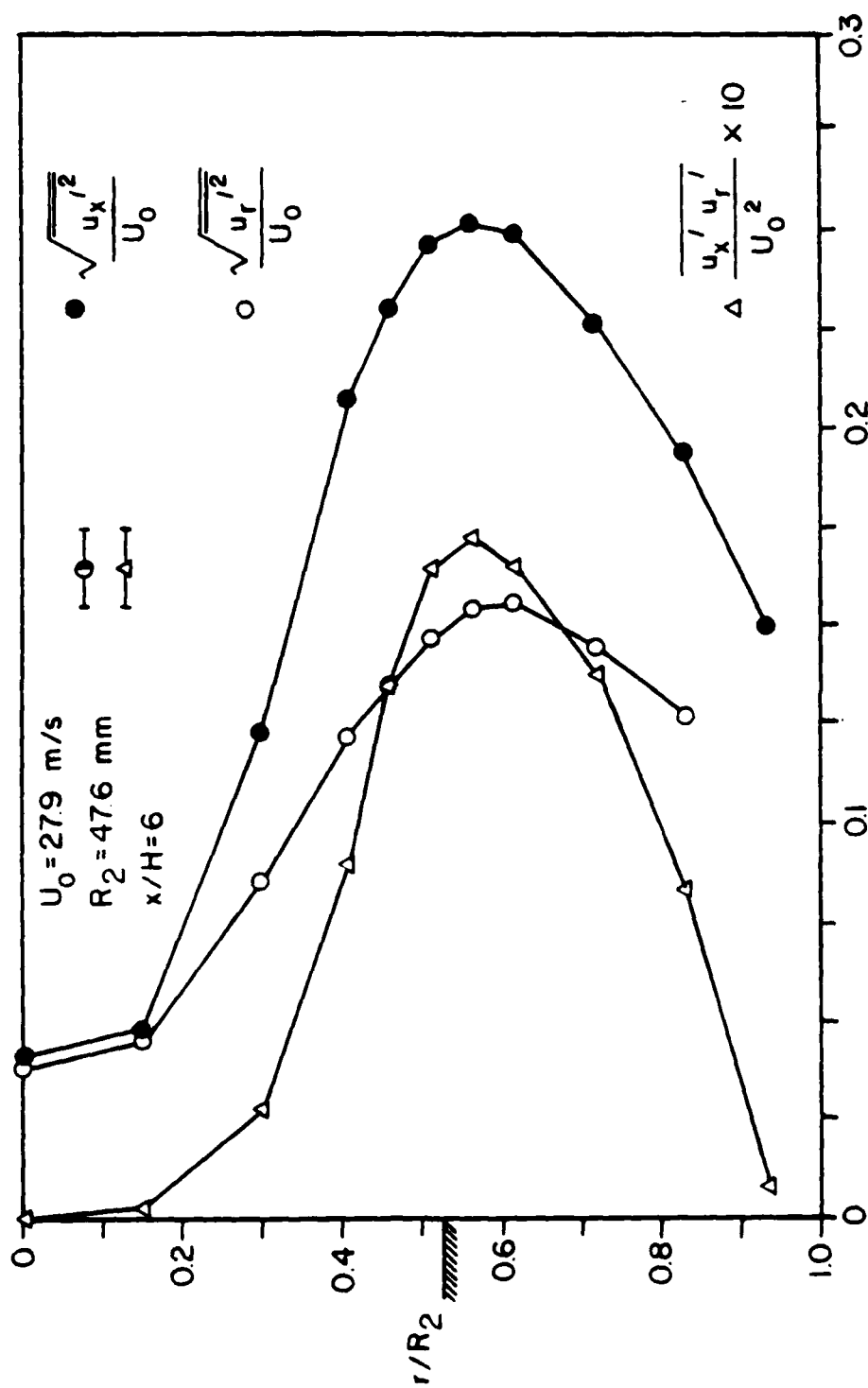


Figure 40. Measured Axial and Radial Turbulence Intensity and Reynolds Stress in the 1.90:1 Sudden Expansion at $x/H = 6$

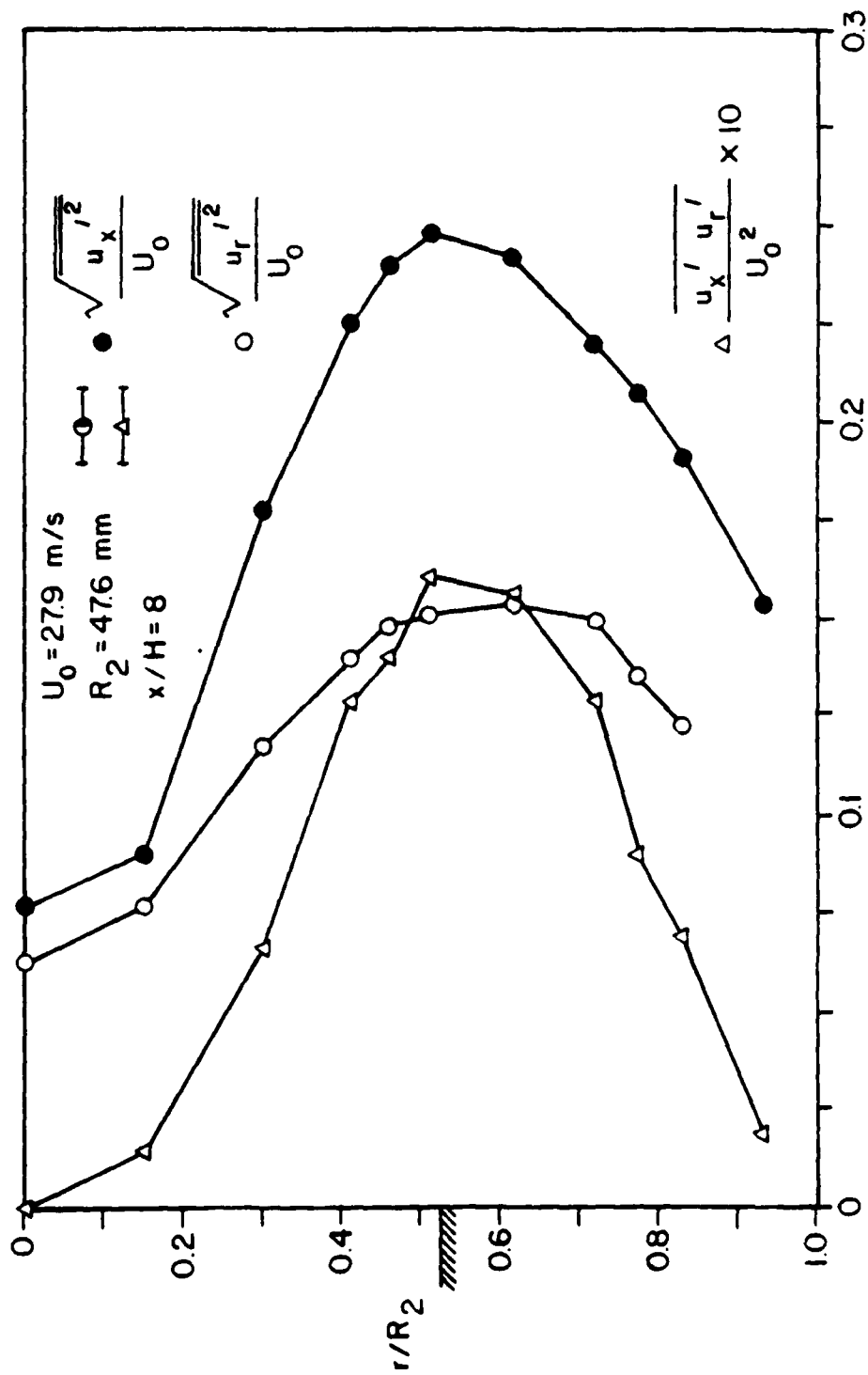


Figure 41. Measured Axial and Radial Turbulence Intensity and Reynolds Stress in the 1.90:1 Sudden Expansion at $x/H = 8$

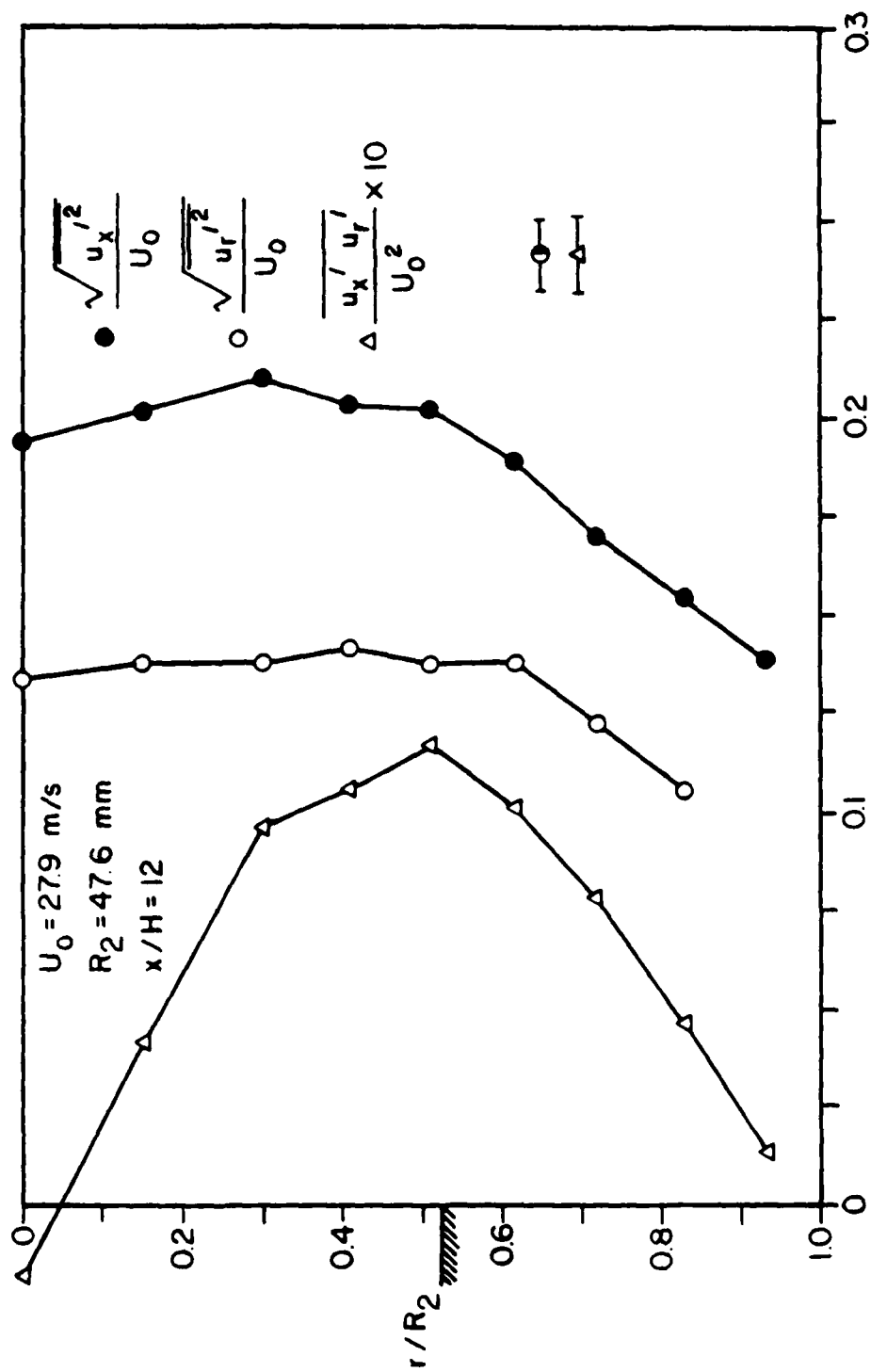


Figure 42. Measured Axial and Radial Turbulence Intensity and Reynolds Stress in the 1.90:1 Sudden Expansion at $x/H = 12$

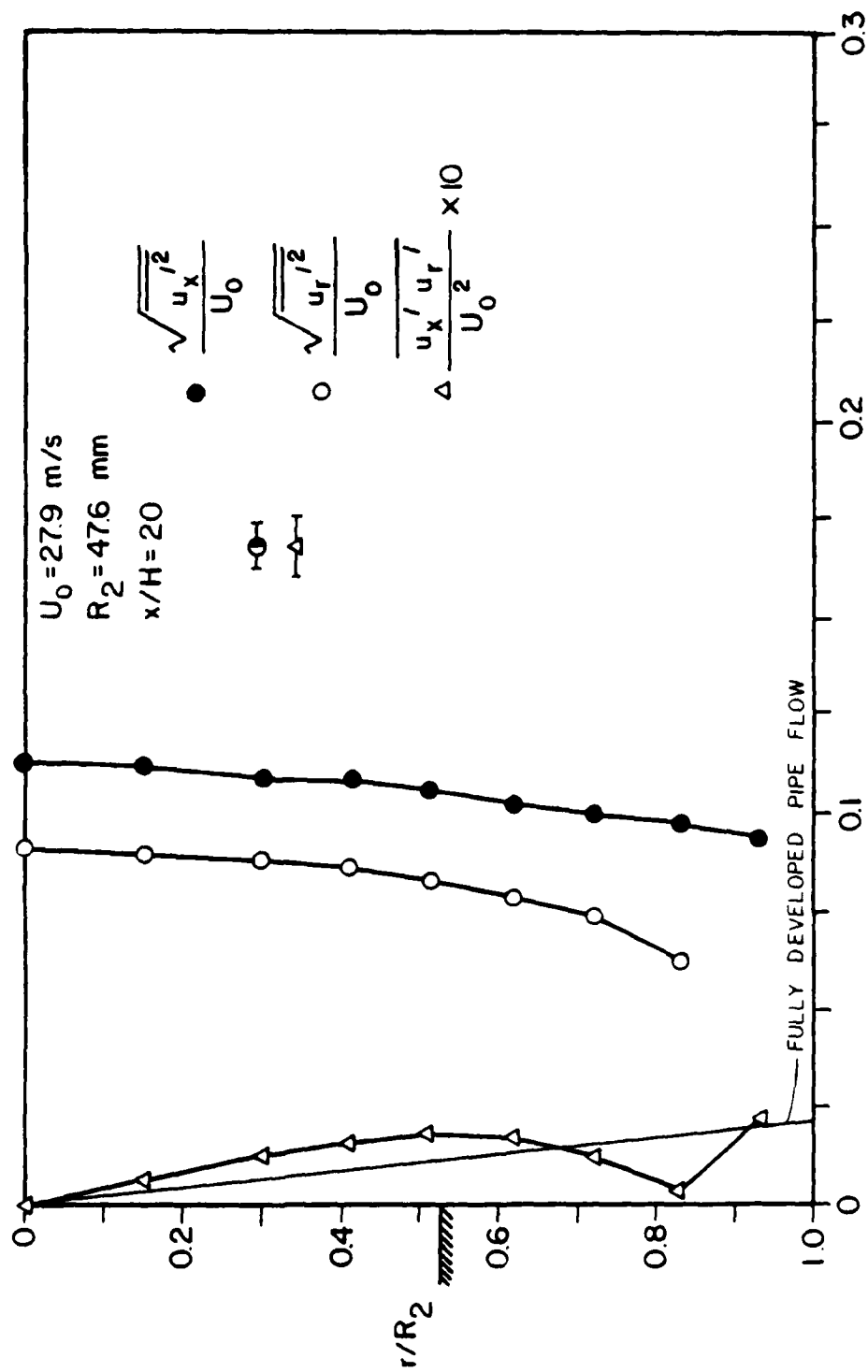


Figure 43. Measured Axial and Radial Turbulence Intensity and Reynolds Stress in the 1.90:1 Sudden Expansion at $x/H = 20$

No numerical predictions were given for these quantities because the code assumes isotropic turbulence throughout the flow. The Reynolds stresses that are shown were calculated using the turbulence intensities measured at the +45 and -45 degree orientations as described in Section V. It is also possible to calculate Reynolds stresses from the measurements made at 0 and 90 degrees plus either the +45 or -45 degree measurements. This alternate method was used to calculate values of the Reynolds stress at several points in the flowfield and the results agreed with those shown to within the estimated uncertainty of the measurements. At the point nearest the wall, $r/R = 0.93$, measurements could only be made in the axial direction and in the +45 and -45 degree directions. For that reason, only axial turbulence intensities and Reynolds stresses are shown at this location.

The profiles of the axial and radial turbulence intensity show the same trends as the profiles of the turbulence kinetic energy as would be expected since the kinetic energy is just a sum of the squares of the turbulence intensities. In the recirculation zone, the axial turbulence intensities are roughly twice as large as the radial turbulence intensities. This shows that the turbulence is not isotropic in this region.

No tangential measurements were made for this investigation, but comparison with the tangential measurements made

by Stevenson, et al. [17] in this same facility shows that the tangential component of the turbulence has a magnitude slightly higher than but very close to the magnitude of the radial turbulence intensity.

Downstream of reattachment as the flow redevelops, the axial and radial turbulence intensity profiles flatten out and the turbulence levels are much closer together. The turbulence intensity data of [17] show that the tangential component behaves very similarly, the profiles flattens out and the intensity level is approximately the same as for the other two components, 110%. Kim, Kline, and Johnston [7] suggest that downstream of reattachment where the fluid near the wall is being accelerated, strong longitudinal strain rates, $\frac{\partial u}{\partial x}$, near the wall cause an increase in $\overline{u'^2_r}$ and a decrease in $\overline{u'^2_x}$. This causes the difference in magnitude between $\overline{u'^2_x}$ and $\overline{u'^2_r}$ to decrease in this region. Both their data, which was taken in a 2-D backward facing step flow, and the present data tend to substantiate that hypothesis.

The maximum normalized streamwise turbulence intensities were found to be 25% for this study. By comparison, maximum values of normalized streamwise turbulence intensity reported for other axisymmetric sudden expansion flows are 24% by Stevenson, et al. [17], 18% by Freeman [14], and 22% by Stevenson, et al. [5]. In backward facing step flows, Bremmer, et al. [3] reported a value of 19%, Kim, Kline, and

Johnston [7], 17%, and Smyth [37], 20%. All three of these backward facing step flows also reported cross stream turbulence intensities, and in all these cases the trends were similar to the measurements made in the present study.

In the recirculation zone, the Reynolds stress trends are similar to the other turbulence quantities. The maximum Reynolds stress occurs at the edge of the recirculation zone on the dividing streamline. The width of the peak in the shear stress profile is roughly the same width as the mixing layer as it spreads downstream of the step. As reattachment is approached the peak moves out away from the wall and remains there as the flow redevelops downstream.

In the region between 12 and 20 step heights, the Reynolds stress decreases by approximately a factor of 5. On the profile at 20 step heights, Figure 43, a solid line is drawn that represents the shear stress distribution that was calculated from the wall shear stress for the straight pipe flow investigation. Since the flowrate for this test is approximately the same as the flowrate used for the straight pipe test, this line approximates a "fully developed" shear stress distribution for this flow. By comparing the experiential data to this line it can be seen that the Reynolds stress levels are very close to their fully developed values at 20 step heights downstream from the sudden expansion while the axial and radial turbulence intensity levels

are still roughly twice the accepted values for a fully developed pipe flow.

The maximum Reynolds stress levels measured in this study were 17×10^{-3} at 4 and 6 step heights. Other reported values of Reynolds stress, all in 2-D backward facing step flows, are -15×10^{-3} by Smyth [37], -10×10^3 by Kim, Kline, and Johnston [7], and -11×10^3 by Driver and Seegmiller [10].

The maximum values of axial turbulence intensity and Reynolds stress obtained in the mixing layer region of the flowfield were compared to the maximum values of these quantities measured in a round free jet as reported in Hinze [33]. In a free jet, the profiles at each axial location are practically similar if the velocities are normalized with the centerline mean velocity at that location. For the present study, when the axial turbulence intensities measured in the mixing layer were normalized with the local centerline velocity, the peak value was found to be 25% to 27% at each location from $x/H = 4$ to 8. In comparison, the free jet data in [33] showed a peak axial turbulence intensity of approximately 28%. The Reynolds stress values obtained in this study showed peak values of 0.018 to 0.020 at all locations from $x/H = 4$ to 8. In comparison, the free jet data showed a peak of approximately 0.017. The peak turbulence intensity and Reynolds stress at $x/H = 2$ was slightly lower than at the other locations.

One of the advantages to making velocity measurements on a traverse perpendicular to the optical axis for a flow of this type is that the LDV probe volume is aligned so that its "short" axis is parallel to the radial direction and thus aligned with the largest velocity gradients. Because of the finite size of the LDV probe volume, measurement inaccuracies can occur in regions where there is a steep velocity gradient. The presence of a velocity gradient across the probe volume will not affect the mean velocity measurements, but the turbulence intensity measurements will be affected. For the present study, the velocity profile at $x/H=2$ can be used to calculate the velocity gradient across the shear layer which is found to be $\frac{\partial u}{\partial r} : 3100 \text{ s}^{-1}$. In this study, the probe volume diameter was approximately $130 \mu\text{m}$; thus there would be a velocity gradient of $: 0.4 \text{ m/sec}$ across the probe volume for this worst case situation. Using the procedure described by Karpuk and Tiederman [38] which assumes a cylindrical probe volume and a linear velocity gradient, the maximum error in the turbulence intensity due to this phenomenon was found to be less than 1%. This error is insignificant and thus velocity gradient error does not affect the measurements.

c. THE STREAM FUNCTION AND REATTACHMENT LENGTH

Figure 44 shows the stream function contours for the flow field calculated by the method described in Section V.

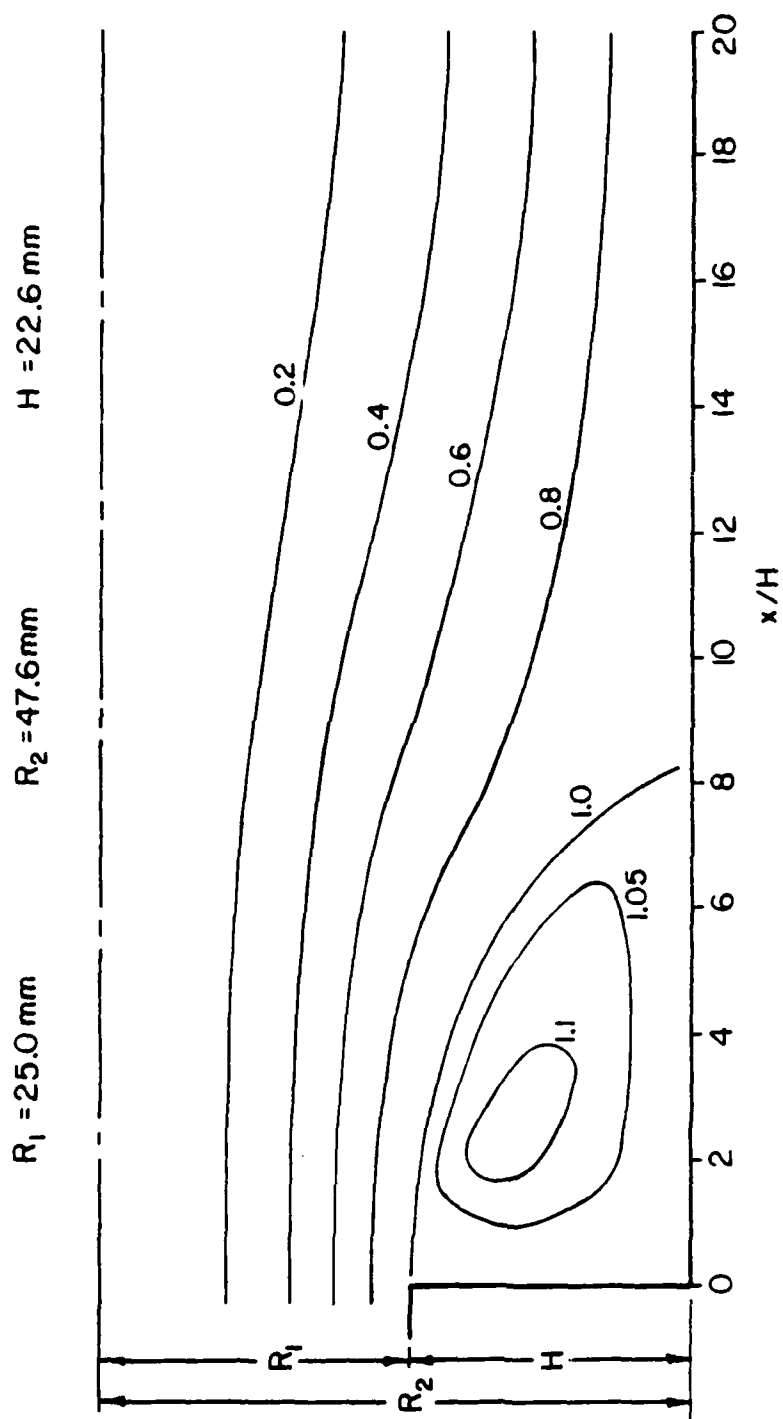


Figure 44. Normalized Stream Function Contours in the 1.90:1 Sudden Expansion

It should be noted that the axial and radial directions are scaled differently in the figure. To partially compensate for the slight mass flow discrepancies due to experimental error, the stream functions are normalized at each axial location. That is, at each gridline the stream functions are scaled to increase from 0 at the centerline to 1.0 at the wall. Linear interpolation was then used to plot constant value contours of the stream function. These plots show that the center of the recirculation zone is approximately 3 step heights downstream of the step face at a radial distance $r/R = 0.72$.

The stream function values were also used to establish the reattachment length by extrapolating the $\psi = 0$ stream function contour to the wall. From these results, the mean reattachment length was found to be 8.3 step heights. This value is in good agreement (within 1/2 step height) with other results for axisymmetric expansions (Table 2).

d. COMPARISON OF NUMERICAL AND EXPERIMENTAL RESULTS

One of the reasons that sudden expansions flows are so popular is because these flows are a good test of the ability of a numerical prediction scheme. In order to provide a basis for comparison of analytically predicted and experimentally measured flow parameters, the computer code CHAMPION 2/E/FIX of Pun and Spalding [35] was run for this flow

geometry. The numerical predictions that are shown here were obtained in a previous study by Stevenson, et al. [17] for this same flow situation. Details of the program and its operation are given in [17], only results will be presented here.

The predictions of mean axial velocity are shown in Figures 19 through 24. The numerical predictions show fair agreement with the measured flow values through the middle part of the profile at all locations except at $x/H = 2$ and 20. At these two locations the predicted values are higher than the experimental values. At the first four axial locations, the width of the mixing layer and the velocities in the mixing layer agree, although at $x/H = 2$ and 4 the location of the mixing layer is slightly different. The main discrepancies between the predicted and measured values occurred along the centerline and near the wall. Along the centerline, the numerical predictions are lower than the measured values up to the point of reattachment. From this point on, the opposite is true and at the last profile a substantially higher mean streamwise velocity is predicted. In [17] the authors observed the same results and mention that a possible explanation for this is that the exit boundary condition in the numerical analysis assumes there is no streamwise velocity gradient when in fact the experiment shows this is not the case. In the recirculation zone, the predicted and experimental profiles differ substantially at

$x/H = 2$. The predicted profile shows high velocity very near the wall and a steep velocity gradient. This velocity gradient would predict a high value of wall shear stress at this location which disagrees with the experimental findings of Driver and Seegmiller [10]. The numerical and experimental profiles are in better agreement at $x/H = 4$ and 6.

The predictions of mean radial velocity are shown in Figures 26 through 31. The scatter in these measurements that was discussed previously is apparent when comparisons are made to numerical predictions, but the overall agreement of the predicted and measured radial velocities is fair. At $x/H = 2$, both the numerical and experimental values show a region of positive and a region of negative velocities. The numerical predictions are lower in both regions, but the crossover from positive to negative velocities occurs at approximately the same radial location. The radial measurements near the centerline at this location were much larger than would be expected. This is probably due to a misalignment of the probe volume orientation so that a component of the axial velocity, which is very large at this location, is being measured. At $x/H = 4, 6, 8$, and 12, the trends of the numerical and experimental velocities agree. The numerical predictions are lower than the measured velocities at all locations except $x/H = 4$. The reason for this switch at only one location is unknown. The difference in magnitude between the numerical predictions and the experimental meas-

urements that is seen in these plots is probably not due to a component of the axial velocity because the difference is not proportional to the axial velocity across the profile. Also, at $x/H = 20$, all numerical predictions of radial velocity are zero because this was the exit boundary condition.

In the comparison of turbulence kinetic energy profiles, Figures 32 through 37, once again, the trends exhibited by the numerical predictions and the experimental results are similar, but the numerical values are much lower in all cases. This is the case in spite of the fact that the inlet turbulence kinetic energy specified in the program corresponds to 5% turbulence intensity in both the axial and radial directions. The measured values of turbulence intensity were less than 2% for each direction at the inlet. This same result was also observed in [17] for the kinetic energy comparison. That study showed that changing the inlet turbulence kinetic energy in the program by a factor of five had only a marginal effect on TKE values downstream and no effect on the mean velocity field. As discussed previously, the TKE values measured in this study were higher than most other measurements in the literature, however no experimental data was found that showed TKE values as low as those predicted by this code.

The axial mean velocity measurements obtained in this investigation were also used to evaluate the similarity analysis of Lokrou and Shen [23]. One of the problems with

this method is that the length scale used for the nondimensionalization is the width of the mixing layer at the given point. This width, δ_0 in Figure 2, must be approximated at each axial location by inspecting the data, thus leading to some ambiguity in its value. Regardless of this, when the axial velocities in the mixing layer at $x/H = 2, 4, 6$, and 8 were normalized (see Figure 2 for definition of parameters) the results in Figure 45 were obtained. The similarity between the velocity profiles at the different axial locations is seen to be quite good, even though they do not agree with either of the predictions. In their paper, Lokrov and Shen compared their predictions to the axisymmetric data of Chaturvedi [39] which fell slightly above the constant eddy viscosity prediction shown in Figure 45.

4. SUDDEN EXPANSION FLOWFIELD ($R_2/R_1 = 2.70$)

As discussed previously, the purpose of this phase of the study was to attempt to locate and measure the secondary recirculation zone. The inlet velocity for this sudden expansion geometry was chosen such that the Reynolds number based on inlet velocity and nozzle exit diameter would be as close as possible to the Reynolds number for the 1.90:1 diameter ratio sudden expansion runs.

Figures 46 and 47 show the axial and radial mean velocity profiles at $x/H = 0.1, 0.3, 0.5, 0.75, 1.0, 1.25$, and

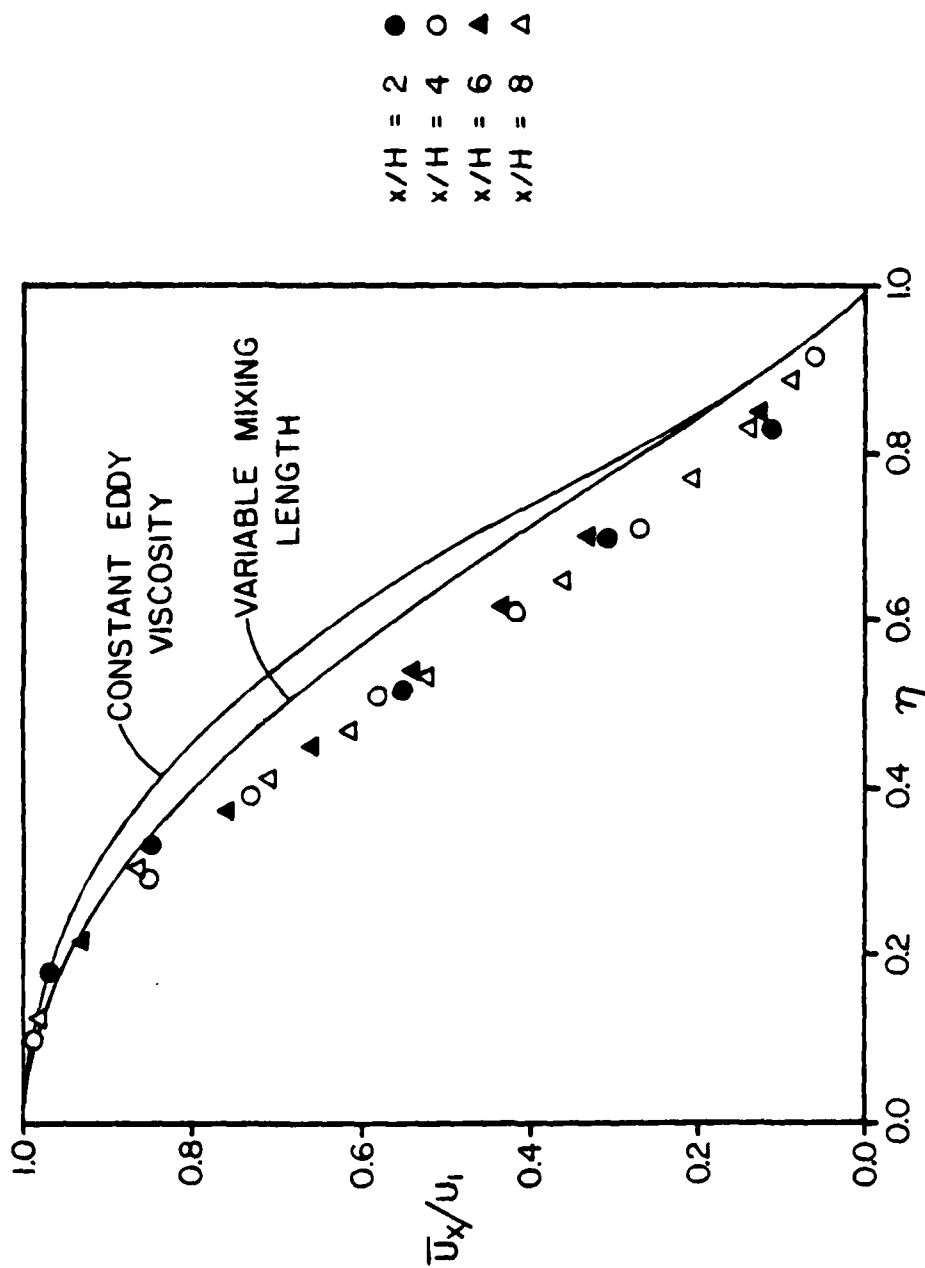
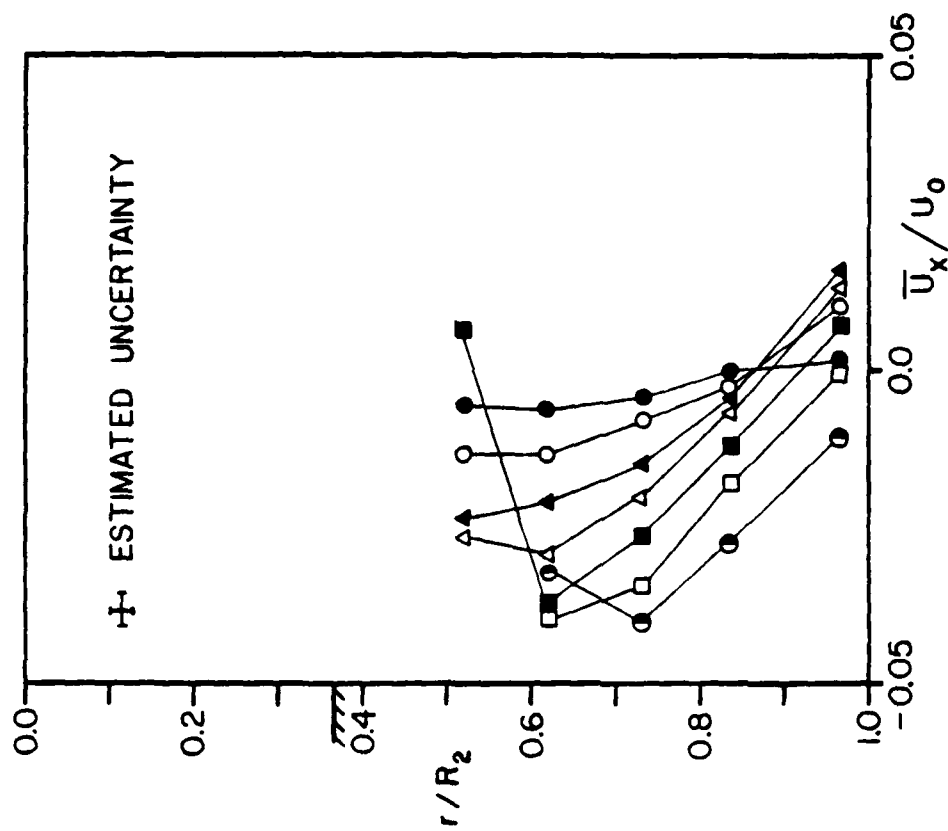


Figure 45. Axial Mean Velocity Profiles in the 1.90:1 Sudden Expansion Normalized with Similarity Parameter (from Ref. [23])



$U_0 = 39.5 \text{ m/s}$
 $R_2 = 47.6 \text{ mm}$
 $H = 30.0 \text{ mm}$

$x/H = 0.1$ ●
 $x/H = 0.3$ ○
 $x/H = 0.5$ ▲
 $x/H = 0.75$ △
 $x/H = 1.0$ ■
 $x/H = 1.25$ □
 $x/H = 1.5$ ○

Figure 46. Measured Axial Mean Velocity Profiles in the 2.70:1 Sudden Expansion

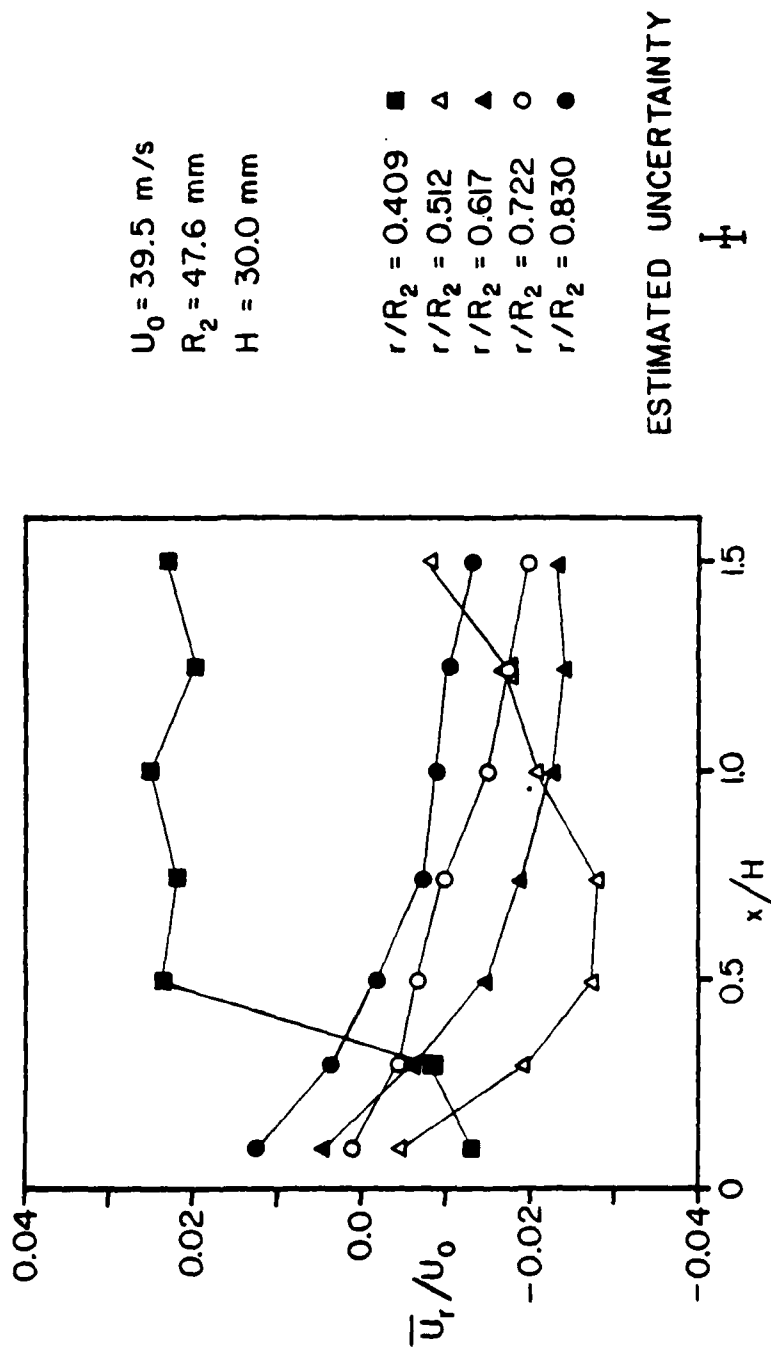


Figure 47. Measured Radial Mean Velocity Profiles in the 2.70:1 Sudden Expansion

1.5. The axial velocities are plotted with radial location as one of the axes and the radial velocities are plotted with axial location as one of the axes. Because these locations are all very close together compared to the spacing in the previous sudden expansion, the profiles do not show as much difference from one grid line to the next and this method of presenting the data results in more clarity. The axial velocity profiles, Figure 46, show that a region of "reverse" flow is present in the outer 10% of the tube. Actually this is not a region of reverse flow, but a region of forward flow within the larger reverse flow region. The profiles that show a forward flow region "cross over" zero velocity at $r/R \approx 0.85$ to 0.90 indicating that the center of the secondary recirculation zone is at this radius. In a similar manner, the radial velocity profile at $r/R = 0.83$ shows velocity changing from positive to negative at $x/H \approx 0.4$ thus indicating the axial location of the center of the secondary recirculation zone.

The same method of determining stream functions that was used in the previous section was also used with these velocity measurements. The stream functions were calculated and constant value contours were drawn as described previously. Since measurements were only made at locations where $r/R > 0.4$, the stream functions could not be normalized from the centerline to the wall as with the other expansion. Figure 48 shows the stream function contours for the flow

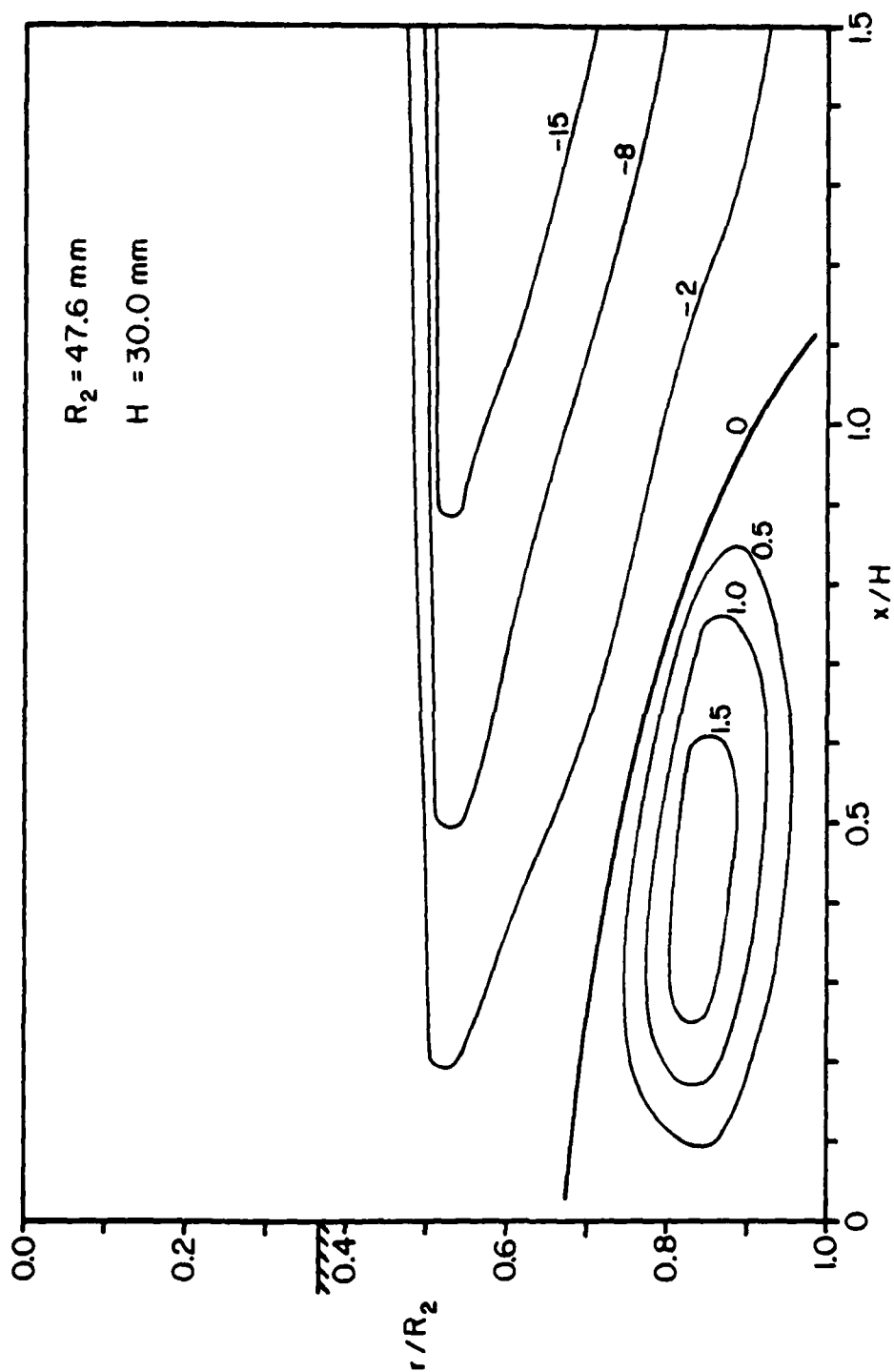


Figure 48. Stream Function Contours in the 2.70:1 Sudden Expansion

field. This figure shows the secondary recirculation zone in much better detail than could be discerned from the velocity plots alone. The secondary recirculation zone is seen to extend from $r/R = 0.7$ out to the wall in the radial direction and from $x/H = 0$ to 1.2. The value of $x/H = 1.2$ for the "secondary reattachment" point is in agreement with the wall shear stress findings of Kangovi & Page [13], Driver & Seegmiller [10], and de Brederode & Bradshaw [20]. The secondary recirculation zone is seen to be centered at $x/H = 0.4$, $r/R = 0.85$ in agreement with the velocity profiles, and small in size in relation to the primary recirculation zone.

Figures 49 and 50 show the axial and radial turbulence intensities in the region of the secondary recirculation zone. These turbulence intensity profiles are nothing like the turbulence intensity profiles across the primary recirculation zone. There is no peak in the profile at the dividing streamline, instead the turbulence intensity is relatively constant across the secondary recirculation zone at each axial location and increases in the axial direction. Once again the axial and radial measurements are plotted differently for clarity.

In order to find some relationship between the strengths of the primary and secondary recirculation zones, vorticity values were calculated throughout both. The main vorticity component in an axisymmetric geometry is defined

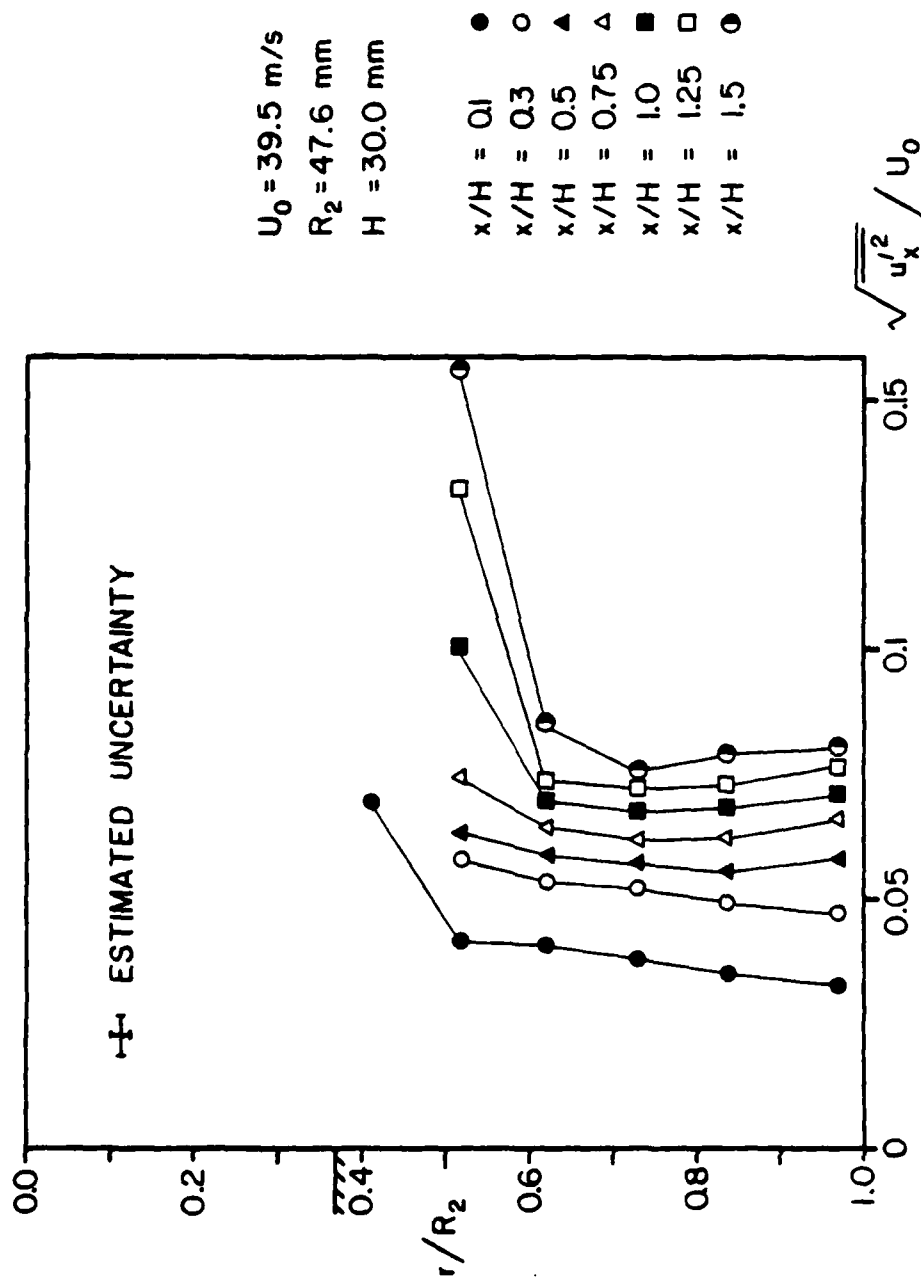


Figure 49. Measured Axial Turbulence Intensity in the 2.70:1 Sudden Expansion

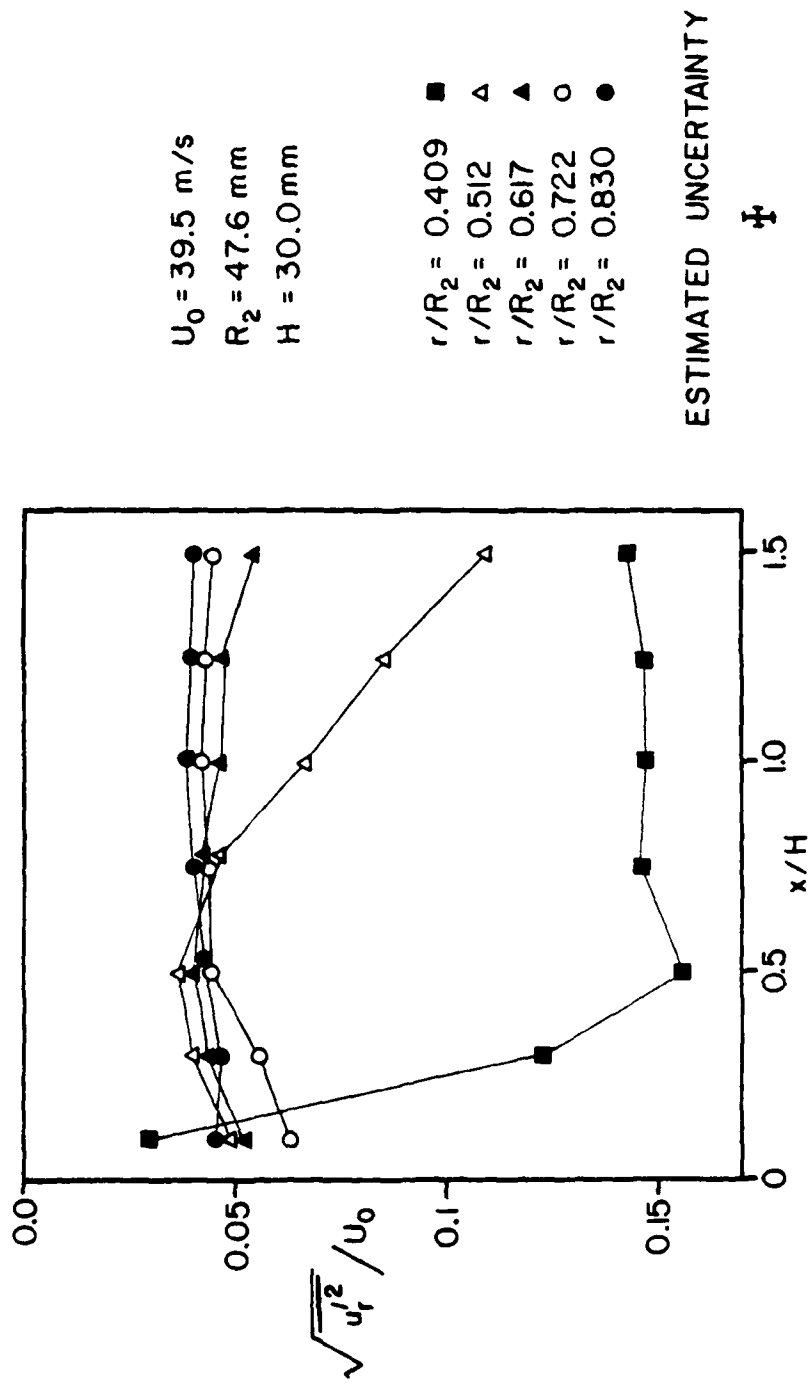


Figure 50. Measured Radial Turbulence Intensity in the 2.70:1 Sudden Expansion

as;

$$\eta_{\theta} = \frac{\partial U_r}{\partial x} - \frac{\partial U_x}{\partial r} \quad (14)$$

A centered finite difference scheme was used to calculate approximate vorticity values throughout the flowfield. Constant value contours of the vorticity were then plotted in a similar fashion to the stream functions and these contours are shown for the two different sudden expansions in Figures 51 and 52. In Figure 51, the 1.90:1 sudden expansion, the vorticity is seen to be near zero at the centerline of the duct as would be expected due to symmetry. The vorticity values increase in the radial direction reaching a maximum value of -7000 s^{-1} just downstream of the separation point and showing a region of high values in the shear layer. The vorticity values then decrease for radial locations beyond the shear layer and a contour of zero vorticity occurs along the outside of the recirculation zone, near the wall. Beyond this contour, the vorticity values change sign and there is a region of positive vorticity near the wall and in the corner. This region indicates the presence of a region of counter-rotating fluid, namely the secondary recirculation zone.

Figure 52 shows the vorticity contours measured in the region of the secondary recirculation zone in the 2.70:1

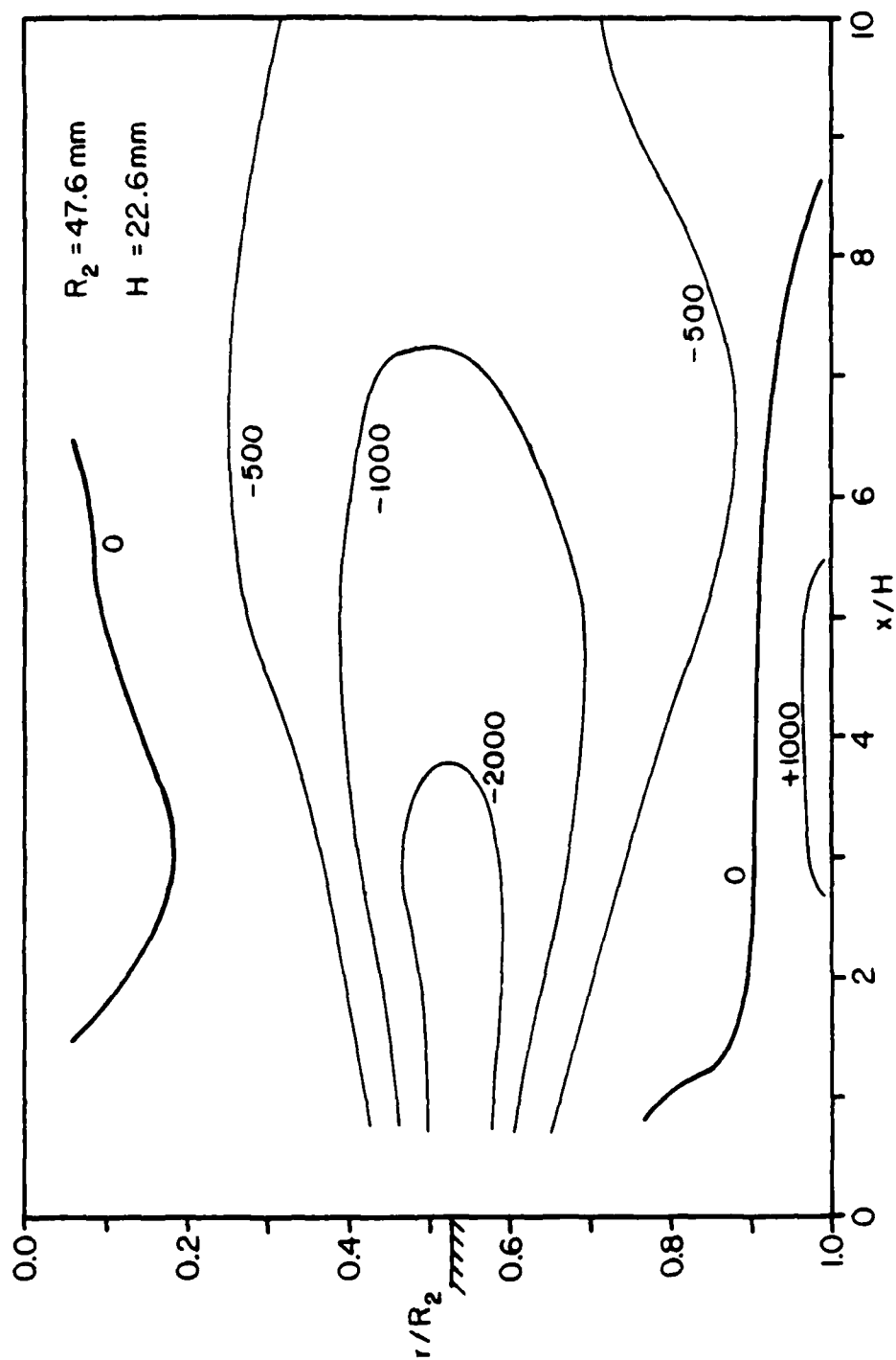


Figure 51. Vorticity Contours in the 1.90:1 Sudden Expansion

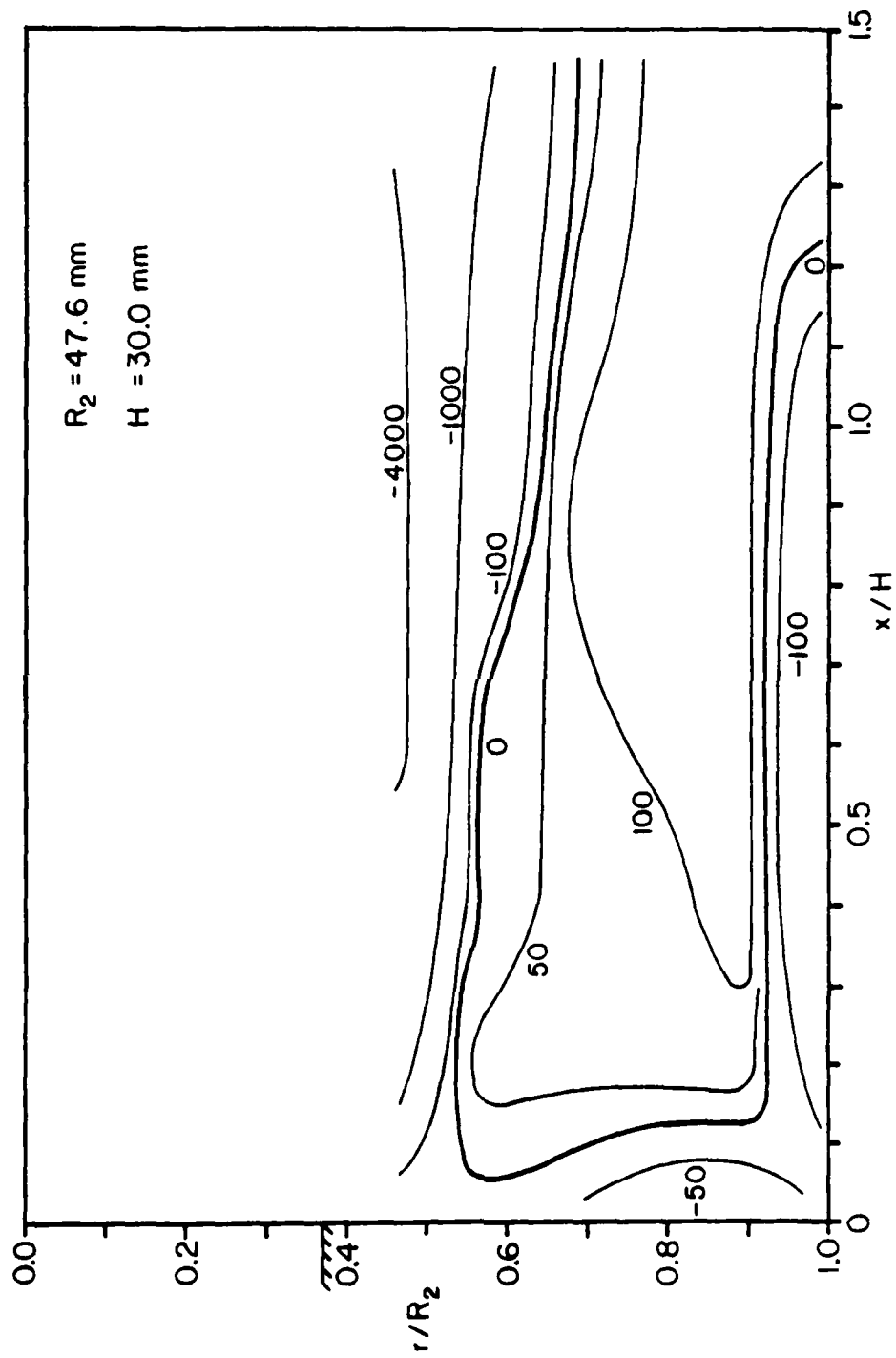


Figure 52. Vorticity Contours in the 2.70:1 Sudden Expansion

sudden expansion. This plot shows similar trends to the primary zone plot. A region of high negative vorticity is observed at the inner radius which is a part of the primary recirculation zone. A zero vorticity contour occurs near the edge of the primary zone and then the vorticities change sign and the secondary zone is marked by a region of positive vorticity. The difference in the vorticity in the edge of the primary zone ($>4000\text{s}^{-1}$) and the vorticity in the secondary zone ($\approx 100\text{s}^{-1}$) indicates that the strength of the primary zone is probably two or three orders of magnitude higher than the strength of the secondary zone. Another fascinating feature of this plot is that there is once again a zero vorticity contour near the wall and the sign changes showing a region of negative vorticity in the corner. This region could possibly indicate the presence of a third recirculation zone located within one-tenth of a step height and driven by the secondary recirculation zone. It should be noted that for both of the vorticity plots, the zero vorticity contour intersects the wall at the same location as the dividing streamline; $x/H \approx 8.3$ for the primary zone and $x/H \approx 1.2$ for the secondary zone.

SECTION VII

CONCLUSIONS AND RECOMMENDATIONS

This investigation showed that it is possible to use a rather simple correction lens system to negate many of the adverse effects of a cylindrical tube wall on laser velocimeter measurements. For a one component LDV the lens system reduces the realignment necessary when moving from one radial location to another and also reduces probe volume distortion and enlargement. For a two component system the lens system significantly reduces alignment problems associated with maintaining the two probe volumes at the same location. In both cases the aberration of the probe volume image at the photomultiplier pinhole is minimized, thus enhancing signal quality. It is probable that a more sophisticated correction lens design could be developed using multiple elements. A lens of this type might be easier to use, but the radius limitations seen with the present lens would still be a problem.

The data obtained in the turbulent pipe flow emphasized a fundamental problem in LDV measurements. In this study it was seen that the coarse velocity resolution resulting from the short N-cycle time caused grouping of the data and

errors in the measured turbulence intensities. Because of this, it is necessary to consider the particular situation under study when setting up an LDV system and choosing the system parameters. For example, if the frequency shift had been reduced or eliminated during this phase of the study, the effect of the data grouping would have been negligible. The turbulent pipe flow measurements also showed that the method used to compute the Reynolds stresses has a large relative uncertainty if the Reynolds stresses are low. Since the flow did not appear to be fully developed, it is difficult to draw any conclusions about the values of the measurements.

In the 1.90:1 diameter ratio sudden expansion, the mean velocities predicted by the 2/E/FIX computer code were in fair agreement with the measured values. The predicted values agreed with the measurements best in the region from $x/H = 4$ to 12. The agreement of the mean velocities was not as good near the inlet and outlet boundaries. The predicted values of turbulence kinetic energy were approximately half the measured values throughout the entire flowfield. Since the measured values agree with other measurements, especially free jet measurements, the numerical predictions are probably in error.

Measurements in the 2.70:1 diameter ratio sudden expansion confirm the existence of a secondary recirculation zone and show that its center is at $r/R = 0.90$ and $x/H = 0.4$.

Calculated values of mean vorticity in the secondary recirculation zone are two orders of magnitude lower than in the primary recirculation zone.

There are, of course, some areas which could be investigated further to better understand these results. They are:

1. To compare direct measurements of Reynolds stress and turbulence kinetic energy made with a two-component LDV with the results obtained by the method used in this study.
2. A more in-depth analysis of vorticity in the flow field.
3. Changes in the 2/E/FIX computer code to improve the predictions of turbulence kinetic energy or comparison to a code with a more sophisticated turbulence model.
4. A more in-depth uncertainty analysis and a further investigation of some of the possible sources of error found in this study.

APPENDICES "A" - "D"

APPENDIX A - Correction Lens Design Program

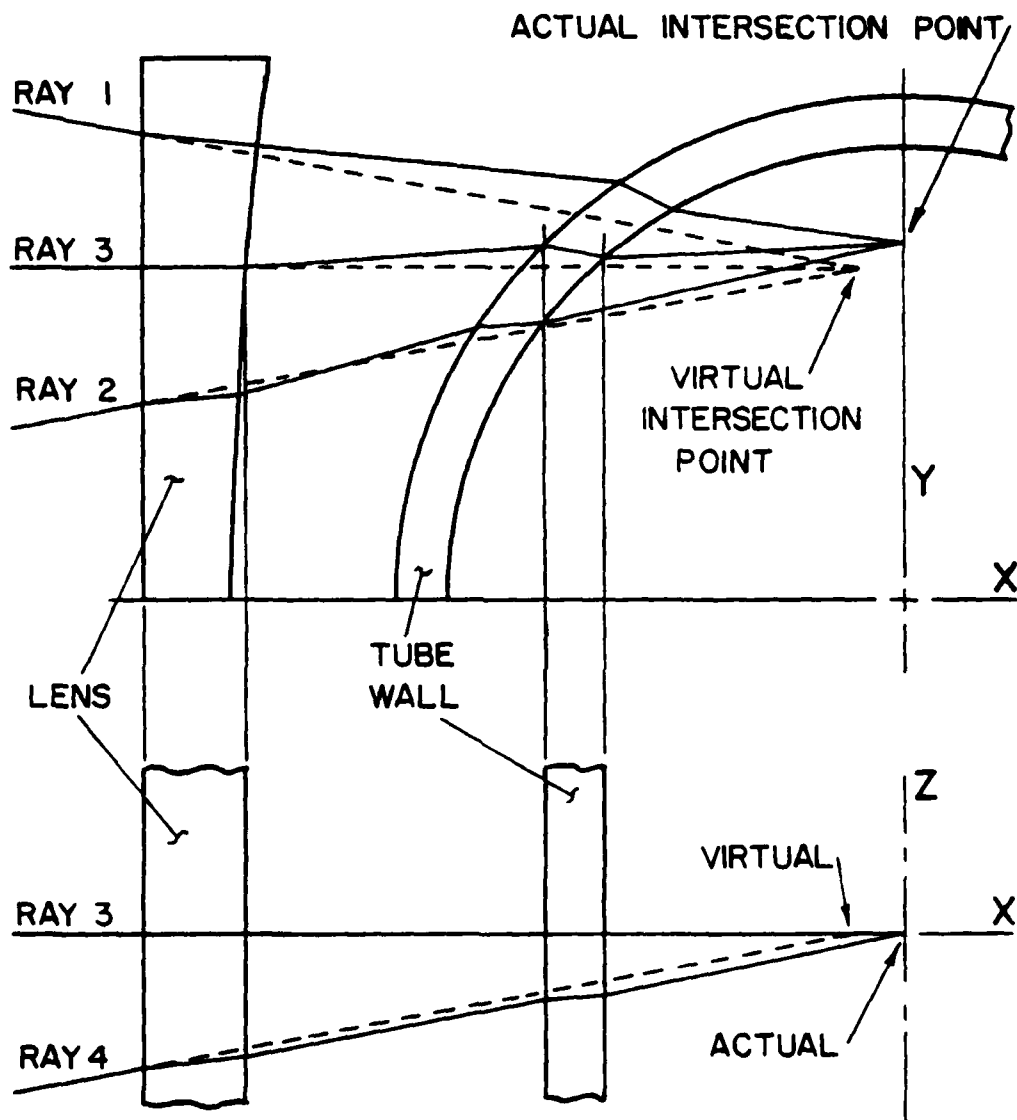
APPENDIX B - Correction Lens Fabrication

APPENDIX C - Uncertainty Analysis

APPENDIX D - Experimental Data

APPENDIX A: CORRECTION LENS DESIGN PROGRAM

The computer program used to design the correction lenses utilizes a simple analytical ray tracing scheme to calculate the paths taken by two pairs of rays and the intersection points of the two pairs. These pairs of rays represent the two LDV beam pairs used to measure the axial and radial velocity components. The intersection point of each pair of rays, which corresponds to the LDV probe volume location, is calculated independently. The distance between these two intersections is then computed to determine if the optical configuration used in that particular trace is acceptable. The algorithm begins with the following parameters given: virtual ray intersection point, ray half angle, tube dimensions and refractive index, and the lens configuration, location and refractive index. The virtual intersection point is defined as the point at which the rays would intersect in the absence of the tube wall and correction lens as shown in Figure A1. Using this point and the ray half angle, the location and orientation of the incoming rays (equivalent to the LDV transmitted beams) can be calculated.



A.1. Ray Traces Performed by the Lens Design Program

The algorithm traces four rays through the optical system, as shown in Figure A1 and described in the program documentation. Rays 1 and 2 represent the two beams that are used to measure a radial velocity component. Ray 1 is the upper ray, ray 2 is the lower, and the plane defined by these two rays is perpendicular to the tube axis. (Referred to as the vertical axis in the program documentation.) Ray 3 is parallel to the x axis and is the bisector of rays 1 and 2. This third ray does not correspond to any beam used for LDV measurements, its purpose is to determine the vertical deflection (in the x-y plane) of an incoming beam in a plane perpendicular to the y axis. Because of the cylindrical geometry, any beam in this plane will experience the same vertical deflections upon passing through the cylindrical optical elements. Ray three is therefore used to determine the vertical deflections experienced by the beams used to measure an axial velocity component since these beams lie in the plane perpendicular to the y axis, the horizontal plane referred to in the program documentation. Another way to describe the purpose of ray 3 is to notice that the ray trace for the radial velocity component is a two dimensional problem, i.e. the rays stay in the plane perpendicular to the tube axis. The ray trace for the axial velocity component, however, is a three dimensional problem because the beams are refracted out of the plane defined by the incoming beam pair as well as being refracted within that plane. The three dimensional problem can be broken down into a pair of

two dimensional problems. First, ray 3 is traced to determine the deflections of the incoming horizontal plane containing the beams used for the axial velocity measurement. The the x and y values of each surface intersection point that are calculated for ray 3 will also apply for ray 4. Ray 4 is then traced in the horizontal plane defined by ray 3 using the known x values of the surface intersection points. The trace of ray 4 computes the z value of each surface intersections point completing the three dimensional trace. Ray 4 represents one of the beams used for the axial measurement, it is oriented such that ray 3 again forms a bisector. Only one ray trace is necessary for the horizontal beam orientation because of symmetry.

The four rays are "backed out" to determine their incoming orientations as described previously. As the ray trace proceeds through the correction lens surfaces, there are separate calculation schemes depending on whether the lens surface is flat or cylindrical. By choosing an appropriate value for the parameter "LTYPE", the program execution is directed to the proper calculation scheme.

After all four rays have been traced through the transmitting correction lens and the incoming tube wall, the intersection points for the vertical and horizontal traces are determined. The difference between these two intersection points is then computed and this difference is checked against a specified tolerance. The differences in the x

direction (the long axis of the probe volume) and the y direction (the short axis of the probe volume) are calculated separately and a separate tolerance is specified for each direction. The tolerances used in the design were approximately 10% of the probe volume dimensions in the respective directions. Upon checking the calculated differences against the specified tolerances, if the tolerances are not satisfied, then nothing is printed out and the program proceeds to the next iteration. If the tolerances are satisfied, all of the vital parameters for the optical arrangement are printed out.

At this point, the program will either proceed to the next iteration or continue the ray trace out the other side of the tube depending on the value of the parameter "MODE". If a backscatter LDV arrangement is being used, there is no reason to continue the trace. Also, in the initial stages of lens design, computer time can be saved by finding a lens configuration that satisfies the probe volume location criteria before proceeding on to the receiving optics.

The second half of the ray trace, if it is performed, is similar to the first half except that the trace proceeds from the inside out. After the four rays are traced out of the system and the exiting beam orientations are known, a virtual origin for the ray pairs is calculated. This vertical origin is defined as the point which the ray pair would emanate from in the absence of the tube wall and receiving

correction lens similar to the virtual intersection point. A separate origin is calculated for the vertical and horizontal ray traces. These virtual origins are used to determine the adjustments that will be required to the receiving optics.

Three parameters may be iterated during the run, they are the y location of the virtual intersection point, the distance from the tube wall to the lens, and the x location of the virtual intersection point. By iterating these three parameters, a run of the program will evaluate the performance of a lens configuration over the radius of the tube. Since the iteration loops for the three parameters are nested, the program can generate a large amount of output and the iteration parameters should be chosen accordingly.


```

C
C CORRECTION LENS DESIGN PROGRAM
C WRITTEN BY RICH GOULD AND RUSS DURRETT, PURDUE UNIV. 1983
C
C THIS PROGRAM CALCULATES THE REAL LOCATION OF THE RAY INTER-
C SECTION POINT FOR A GIVEN UNOBSTRUCTED (VIRTUAL) INTERSECTION
C (X0 & Y0) WHILE ITERATING THE 3 PARAMETERS X0, Y0, AND L2
C THE LENSES ARE SPECIFIED WITH THE PARAMETERS LTYPE, RFRONT,
C RBACK, RIL, THK1, AND THK2. THE LENSES MUST BE OF THE SAME TYPE,
C HOWEVER THE THICKNESSES OF THE LENSES MAY BE DIFFERENT
C THE DATA AT THE END OF THE PROGRAM GIVES A SAMPLE RUN FOR THE
C CASE OF A PLANO-CONCAVE LENS WITH A RADIUS OF CURVATURE (RBACK)
C OF 47 INCHES AND A 4 INCH O.D., 3.75 INCH I.D. PIPE
C
C IMPORTANT SINCE THE ITERATION LOOPS FOR Y0, L2, AND X0
C ARE NESTED, THIS PROGRAM CAN GENERATE A LOT OF OUTPUT
C CHOOSE THE PARAMETERS NYSTEP, NLSTEP, AND NXSTEP
C ACCORDINGLY
C
C 0000      000000000      0000
C 0000      0000 1 0000      0000
C 0000      000 1 000      0000
C 000      00 1 00      000
C 000      00 1(+Y) 00      000
C 00      00 1 00      00
C 00      00 1 00      00
C 00      00 1 00      00
C 00      00 1 00      00
C 00      00 1 00      00
C 00      00 1 00      00
C 000      00 1 00      000
C 000      00 1 00      000
C 0000      000 1 0000      0000
C 0000      0000 1 0000      0000
C 0000      000000000      0000
C 11      1      11
C 11      1      11
C 11----- L2 -----1.3-----11
C 1----- L1 -----1-----L4-----1
C
C LEFT SIDE IS TRANSMITTING OPTICS
C
C NOTE ALL LENGTH DIMENSIONS CAN BE IN ANY UNITS AS
C LONG AS YOU ARE CONSISTENT THROUGHOUT THE PROGRAM
C
C *** DESCRIPTION OF INPUT PARAMETERS *****
C
C MODE- IF 1 THEN RAY TRACE PROCEEDS TO BEAM INTERSECTION POINT
C AND STOPS, ONLY TAKES TRANSMITTING OPTICS INTO ACCOUNT
C IF 2 THEN RAY TRACE CONTINUES THROUGH BEAM INTERSECTION
C POINT AND OUT THROUGH THE RECEIVING OPTICS
C
C LTYPE- 1 PLANO-CONCAVE OR PLANO-CONVEX LENS
C 2 CONCAVE-PLANO OR CONVEX-PLANO LENS
C 3 BOTH LENS SURFACES CYLINDRICAL
C LTYPE DESCRIBES THE TRANSMITTING LENS. THE RECEIVING
C LENS IS SIMILAR BUT SYMMETRICALLY OPPOSITE
C
C R2-OUTSIDE RADIUS OF TUBE
C R3-INSIDE RADIUS OF TUBE
C AL0-BEAM CONVERGENCE HALF ANGLE (DEGREES)
C R1A-REFRACTIVE INDEX OF AIR
C R1L-REFRACTIVE INDEX OF CORRECTION LENS

```

```

C      RIT-REFRACTIVE INDEX OF TUBE
C      RIC-REFRACTIVE INDEX OF GAS INSIDE TUBE
C      THK1 AND THK2 ARE THICKNESSES OF LENSES 1 AND 2
C      RFRONT AND RBACK ARE THE RADII OF THE FIRST AND SECOND SURFACES
C      OF THE TRANSMITTING LENS. THE SIGN CONVENTION USED IS THAT
C      THE RADIUS IS POSITIVE IF THE CENTER OF CURVATURE IS TO THE
C      RIGHT OF THE VERTEX OF THE SURFACE. IF A SURFACE IS PLANAR,
C      THIS IS TAKEN INTO ACCOUNT BY THE CHOICE OF LTYPE AND ANY
C      VALUE MAY BE ENTERED FOR THAT SURFACE
C      L1-X LOCATION OF THE VERTEX OF THE FIRST SURFACE
C      OF THE CORRECTION LENS (THIS WILL ALWAYS BE NEGATIVE)
C      L2-X LOCATION OF THE VERTEX OF THE SECOND SURFACE OF THE
C      CORRECTION LENS
C      XO-INITIAL X LOCATION OF UNOBSTRUCTED LASER BEAM
C      YO-INITIAL Y LOCATION OF UNOBSTRUCTED LASER BEAM
C      XDIFF-X DIFFERENCE IN LOCATION OF PROBE VOLUMES FOR HORIZ
C      AND VERTICAL RAY TRACES
C      YDIFF-Y DIFFERENCE
C      XTOL AND YTOL ARE X AND Y PRINTOUT TOLERANCES FOR XDIFF & YDIFF
C      ORIENT-ANGLE BETWEEN THE X AXIS AND THE BISECTOR OF THE BEAMS
C      FOR THE VERTICAL RAY TRACE
C      HANG-ACTUAL HALF ANGLE OF THE INTERSECTION FOR THE VERT TRACE
C      VERT VIRT AND HORIZ. VIRT IN THE PRINTOUT ARE THE VIRTUAL
C      INTERSECTION POINTS OF THE BEAMS EXITING THE SECOND LENS
C      NXSTEP, NYSTEP, AND NLSTEP ARE THE NUMBER OF STEPS IN THE
C      ITERATION LOOPS FOR XO, YO, AND L2
C      XSTEP, YSTEP, AND LSTEP ARE THE SIZE OF THE STEPS
C      DELL- A DELTA L VALUE THAT IS USED TO VARY THE LOCATION OF
C      THE RECEIVING CORRECTION LENS WHILE THE TRANSMITTING
C      CORRECTION LENS REMAINS STATIONARY
C
C DATA SHOULD BE ENTERED AS FOLLOWS
C LINE 1 (3F10 0, 4F5 0), TUBE O.D., TUBE I.D., BEAM HALF ANGLE
C      IN DEGREES, RI AIR, RI LENS, RI TUBE, RI MEDIUM
C LINE 2 (5F10 0), LENS 1ST SURFACE RADIUS, LENS 2ND SURFACE
C      RADIUS, INITIAL VALUE OF L2, LENS 1 THICKNESS, LENS 2
C      THICKNESS
C LINE 3 (2I5, 2F10 0), MODE, LTYPE, X INITIAL, Y INITIAL
C LINE 4 (3I10, F10 0), NUMBER OF Y STEPS, Y STEP SIZE,
C      NUMBER OF LENS STEPS, LENS STEP SIZE, NUMBER OF X STEPS,
C      X STEP SIZE
C LINE 5 (4F10 0), X TOLERANCE FOR INTERSECTION, Y TOLERANCE,
C      DELL
C
C      DIMENSION X(9,4), Y(9,4), Z(9,4), AL(9,4), TAL(9,4), TH(6,4),
C      * PHI(3,4), B(3), B1(3), B2(3), B3(3), XSTART(4), YSTART(4)
C      REAL L1, L2, L1INIT, L2INIT, L31, L32, L4, LSTEP
C
C      READ IN AND WRITE OUT INITIAL PARAMETERS
C
C      READ (5,320) R2,R3,ALD,RIA,RIL,RIT,RIC
C      READ (5,330) RFRONT,RBACK,L2,THK1,THK2
C      READ (5,340) MODE,LTYPE,XO,YO
C      READ (5,400) NYSTEP,YSTEP,NLSTEP,LSTEP,NXSTEP,XSTEP
C      READ (5,410) XTOL,YTOL,DELL
C      RADIANT = 57.29577951
C      L1 = L2-THK1
C      XOINIT = XO
C      RBINIT = RBACK
C      L1INIT = L1

```

```

L2INIT = L2
RR2 = 2.0*R2
RR3 = 2.0*R3
INDEX = 0
WRITE (6,230)
WRITE (6,240) RR2,RIA,RIL
WRITE (6,250) RR3,RIT,RIC
WRITE (6,260) ALD,RFRONT,RBACK
WRITE (6,270) THK1,THK2,L2,X0,Y0
WRITE (6,300) NYSTEP,YSTEP,NLSTEP,ALOR,RADIAN,ALOR*180/PI
IF (LTYPE.EQ.1) WRITE (6,420)
IF (LTYPE.EQ.2) WRITE (6,430)
IF (LTYPE.EQ.3) WRITE (6,440)
IF (MODE.EQ.1) WRITE (6,450)
IF (MODE.EQ.2) WRITE (6,460)
WRITE (6,310)
WRITE (6,290)
ALOR = ALD/RADIAN

C
C   INITIALIZE CONVERGENCE BEAM HALF ANGLE
C
AL(1,1) = -ALOR
AL(1,2) = ALOR
AL(1,3) = 0.0
AL(1,4) = -ALOR

C
C   STEP IN UNOBSTRUCTED BEAM Y LOCATION
C
DO 220 JY = 1,NYSTEP
  ISAV = 1
  IF (JY.EQ.1) GO TO 10
  YO = YO+YSTEP
10  CONTINUE

C
C   STEP X LOCATION OF SECOND CORRECTION LENS
C
DO 200 J = 1,NLSTEP
  IF (J.EQ.1) GO TO 20
  L2 = L2+LSTEP
  IF (ABS(L2).LT.R2) GO TO 200
20  CONTINUE
  L1 = L2-THK1

C
C   INITIALIZE X LOCATION OF BEAM INTERSECTION
C
DO 30 NR = 1,3
  XSTART(NR) = L1*2.0
30  X(1,NR) = L1

C
C   STEP IN UNOBSTRUCTED BEAM X LOCATION
C
DO 170 I = 1,NXSTEP
  IF (I.EQ.1) GO TO 40
  XD = XD+XSTEP
40  CONTINUE

C
C   VERTICAL RAY TRACING THROUGH ALL OPTICAL ELEMENTS
C   BEAM INTERSECTION POINT FOR RADIAL BEAM
C   NR-RAY NUMBER
C   NR=1 TOP RAY OF CONVERGENT BEAMS IN BEAM

```

```

C NR=2 BOTTOM RAY OF CONVERGENT BEAMS IN VERT TRACE(POS SLOPE)
C NR=3 CENTER RAY OF CONVERGENT BEAMS (ZERO SLOPE, TO BE USED
C IN THE HORIZ RAY TRACE
C
C THE FIRST NUMBER IN EACH ARRAY, SUCH AS IN X(4,NR) IS A LOCATION
C NUMBER THE LOCATIONS ARE
C
C 1 FIRST SURFACE OF TRANSMITTING CORRECTION LENS
C 2 SECOND SURFACE OF TRANSMITTING CORRECTION LENS
C 3 OUTSIDE TUBE WALL, INCOMING SIDE
C 4 INSIDE TUBE WALL, INCOMING SIDE
C 5 BEAM INTERSECTION POINT
C 6 INSIDE TUBE WALL, OUTGOING SIDE
C 7 OUTSIDE TUBE WALL, OUTGOING SIDE
C 8 FIRST LENS SURFACE, RECEIVING CORRECTION LENS
C 9 SECOND LENS SURFACE, RECEIVING CORRECTION LENS
C 10 VIRTUAL POINT OF ORIGIN FOR BEAMS LEAVING SURFACE 9
C
C DO 90 NR = 1,3
C IF (LTYPE.NE.1) GO TO 50
C Y(1,NR) = Y0+(X(1,NR)-X0)*TAN(AL(1,NR))
C
C WRITE (6,350) X(1,NR),Y(1,NR)
C
C AL(2,NR) = ASIN(RIA/RIL*SIN(AL(1,NR)))
C GO TO 60
50 YSTART(NR) = Y0+(XSTART(NR)-X0)*TAN(AL(1,NR))
C TAL(1,NR) = TAN(AL(1,NR))
C BB = YSTART(NR)+(L1-XSTART(NR)+RFRONT)*TAL(1,NR)
C CURVE = -1.0
C IF (RFRONT LT 0.0) CURVE = 1.0
C CALL STCR1 (TAL(1,NR),BB,RFRONT,CURVE,XX,YY,IS)
C X(1,NR) = XX+RFRONT+L1
C Y(1,NR) = YY
C
C WRITE (6,350) X(1,NR),Y(1,NR)
C
C PHI1 = -ASIN(Y(1,NR)/RFRONT)
C TH1 = PHI1-AL(1,NR)
C TH2 = ASIN(RIA/RIL*SIN(TH1))
C AL(2,NR) = PHI1-TH2
60 CONTINUE
C
C WRITE (6,360) AL(2,NR)
C
C TAL(2,NR) = TAN(AL(2,NR))
C IF (LTYPE.NE.2) GO TO 70
C X(2,NR) = L2
C Y(2,NR) = Y(1,NR)+(X(2,NR)-X(1,NR))*TAL(2,NR)
C
C WRITE (6,350) X(2,NR),Y(2,NR)
C
C AL(3,NR) = ASIN(RIL/RIA*SIN(AL(2,NR)))
C GO TO 80
70 B1(NR) = Y(1,NR)-(L1-L2-RBACK)*TAL(2,NR)
C CURVE = -1.0
C IF (RBACK LT 0.0) CURVE = 1.0
C CALL STCR1 (TAL(2,NR),B1(NR),RBACK,CURVE,XX,YY,IS)
C
C X AND Y LOCATION OF REAL BEAM INTERSECTION WITH 2ND SURFACE

```

```

C
C      X(2,NR) = XX+L2+RBACK
C      Y(2,NR) = YY
C
C      WRITE (6,350) X(2,NR),Y(2,NR)
C
C      PHI(1,NR) = -ASIN(Y(2,NR)/RBACK)
C      TH(1,NR) = PHI(1,NR)-AL(2,NR)
C      U = RIL/RIA*SIN(TH(1,NR))
C      AU = ABS(U)
C
C      CHECK TO SEE IF THERE IS TOTAL INTERNAL REFLECTION
C
C      IF (AU GT 1.0) GO TO 190
C      TH(2,NR) = ASIN(RIL/RIA*SIN(TH(1,NR)))
C      AL(3,NR) = PHI(1,NR)-TH(2,NR)
C      CONTINUE
C
C      WRITE (6,360) AL(3,NR)
C
C      TAL(3,NR) = TAN(AL(3,NR))
C      B2(NR) = Y(2,NR)-X(2,NR)*TAL(3,NR)
C      CALL STCR1 (TAL(3,NR),B2(NR),R2,-1.0,XX,YY,IS)
C
C      CHECK TO SEE IF BEAM WILL INTERSECT QD OF TUBE
C
C      IF (IS EQ 1) GO TO 190
C
C      X AND Y LOCATION OF REAL BEAM INTERSECTION WITH 3RD SURFACE
C
C      X(3,NR) = XX
C      Y(3,NR) = YY
C
C      WRITE (6,350) X(3,NR),Y(3,NR)
C
C      PHI(2,NR) = -ASIN(Y(3,NR)/R2)
C      TH(3,NR) = PHI(2,NR)-AL(3,NR)
C      U1 = RIA/RIT*SIN(TH(3,NR))
C      AU1 = ABS(U1)
C
C      CHECK FOR TOTAL INTERNAL REFLECTION
C
C      IF (AU1 GT 1.0) GO TO 190
C      TH(4,NR) = ASIN(RIA/RIT*SIN(TH(3,NR)))
C      AL(4,NR) = PHI(2,NR)-TH(4,NR)
C
C      WRITE (6,360) AL(4,NR)
C
C      TAL(4,NR) = TAN(AL(4,NR))
C      B3(NR) = Y(3,NR)-X(3,NR)*TAL(4,NR)
C      CALL STCR1 (TAL(4,NR),B3(NR),R3,-1.0,XX,YY,IS)
C
C      CHECK TO SEE IF BEAM WILL INTERSECT ID OF TUBE
C
C      IF (IS EQ 1) GO TO 190
C      X(4,NR) = XX
C      Y(4,NR) = YY
C
C      WRITE (6,350) X(4,NR),Y(4,NR)

```

```

C      PHI(3,NR) = -ASIN(Y(4,NR)/R3)
C      TH(5,NR) = PHI(3,NR)-AL(4,NR)
C      U2 = RIT/RIC*SIN(TH(5,NR))
C      AU2 = ABS(U2)
C
C      CHECK FOR TOTAL INTERNAL REFLECTION
C
C      IF (AU2 GT 1.0) GO TO 190
C      TH(6,NR) = ASIN(RIT/RIC*SIN(TH(5,NR)))
C      AL(5,NR) = PHI(3,NR)-TH(6,NR)
C
C      WRITE (6,360) AL(5,NR)
C
C      TAL(5,NR) = TAN(AL(5,NR))
90      B(NR) = Y(4,NR)-X(4,NR)*TAL(5,NR)
C
C      REAL X AND Y LOCATION OF INTERSECTING BEAMS OF VERTICAL TRACE
C
C      XV = (B(2)-B(1))/(TAL(5,1)-TAL(5,2))
C      YV = XV*TAL(5,1)+B(1)
C      ANG = (TAL(5,1)+TAL(5,2))/2.0
C      DIVTAN = ABS(TAL(5,1))+ABS(TAL(5,2))
C
C      ANGLE WRT X AXIS OF THE BISECTOR OF THE TWO BEAMS
C
C      ORIENT = RADIAN*ATAN(ANG)
C
C      ACTUAL HALF ANGLE OF INTERSECTING BEAMS
C
C      HANG = RADIAN*ATAN(DIVTAN)/2.0
C
C      END VERTICAL RAY TRACE
C      STARTING HORZ RAY TRACE
C
C      Z(1,4) = Y0-Y(1,2)
C      AL(2,4) = ASIN(RIA/RIL*SIN(AL(1,4)))
C      TAL(2,4) = TAN(AL(2,4))
C      Z(2,4) = Z(1,4)+TAL(2,4)*(X(2,3)-X(1,3))
C      AL(3,4) = ASIN(RIL/RIA*SIN(AL(2,4)))
C      TAL(3,4) = TAN(AL(3,4))
C      Z(3,4) = Z(2,4)+TAL(3,4)*(X(3,3)-X(2,3))
C      AL(4,4) = ASIN(RIA/RIT*SIN(AL(3,4)))
C      TAL(4,4) = TAN(AL(4,4))
C      Z(4,4) = Z(3,4)+TAL(4,4)*(X(4,3)-X(3,3))
C
C      WRITE (6,380) Z(1,4), Z(2,4), Z(3,4), Z(4,4)
C
C      AL(5,4) = ASIN(RIT/RIC*SIN(AL(4,4)))
C      TAL(5,4) = TAN(AL(5,4))
C
C      REAL X AND Y LOCATION OF BEAM INTERSECTION IN HORZ TRACE
C
C      X(5,3) = X(4,3)-Z(4,4)/TAL(5,4)
C      X(5,4) = X(5,3)
C      Y(5,3) = Y(4,3)+TAL(5,3)*(X(5,3)-X(4,3))
C      Y(5,4) = Y(5,3)
C      XM = X(5,4)
C      YM = Y(5,4)
C
C      END HORIZONTAL RAY TRACE

```

```

C      XDIFF = XV-XH
C      YDIFF = YV-YH
C      AXD = ABS(XDIFF)
C      AYD = ABS(YDIFF)
C      INDEX = INDEX+1
C
C      VERTICAL AND HORZ RAY TRACE INTERSECTION TOLERANCE FOR PRINTOUT
C
C      IF (AXD LE XTOL AND AYD LE YTOL) GO TO 100
C      IF (I EQ 1 AND ISAV EQ 1) GO TO 180
C      IF (I EQ NXSTEP AND ISAV EQ 2) GO TO 210
C
C      THE ABOVE TWO IF STATEMENTS USING THE VARIABLE ISAV ARE
C      FOR THE PURPOSE OF ELIMINATING ITERATIONS THAT ARE KNOWN
C      TO BE NO GOOD THIS STREAMLINING MAY BE ELIMINATED BY
C      COMMENTING THESE TWO STATEMENTS TO MAKE THEM NON-EXECUTABLE
C
C      GO TO 170
100  WRITE (6,370) XQ,YQ,XV,YV,XH,YH,XDIFF,YDIFF,
      *      L2,ORIENT,HANG
C      IF (I EQ NXSTEP) ISAV = 2
C      IF (MODE EQ 1) GO TO 170
C
C      BEGIN SECOND HALF OF RAY TRACE
C      THE SECOND HALF OF THE RAY TRACE IS A SIMILAR CALCULATION
C      TO THE FIRST HALF EXCEPT THAT THE RAY TRACE PROCEEDS
C      OUTWARD INSTEAD OF INWARD
C
C      DO 110 NR = 1,3
C      BB = Y(4,NR)-TAL(5,NR)*X(4,NR)
C      CALL STCRI (TAL(5,NR),BB,R3,1 0,X(6,NR),Y(6,NR),IS)
C      CALL CRUNCH (X(6,NR),Y(6,NR),R3,AL(5,NR),RIC,RIT,
      *      AL(6,NR),TAL(6,NR))
C      BB = Y(6,NR)-TAL(6,NR)*X(6,NR)
C      CALL STCRI (TAL(6,NR),BB,R2,1 0,X(7,NR),Y(7,NR),IS)
C      CALL CRUNCH (X(7,NR),Y(7,NR),R2,AL(6,NR),RIT,RIA,
      *      AL(7,NR),TAL(7,NR))
110  CONTINUE
C      Z(6,4) = Z(4,4)+TAL(5,4)*(X(6,3)-X(4,3))
C      AL(6,4) = ASIN(RIC/RIT*SIN(AL(5,4)))
C      TAL(6,4) = TAN(AL(6,4))
C      Z(7,4) = Z(6,4)+TAL(6,4)*(X(7,3)-X(6,3))
C      AL(7,4) = ASIN(RIT/RIA*SIN(AL(6,4)))
C      TAL(7,4) = TAN(AL(7,4))
C      L31 = -L2-DELL
C      IF (L31 LT R2) L31 = -L2
C      L32 = -L2+DELL
C      WHILE (L31 LE L32) DO
C      DO 160 NR = 1,3
C      IF (LTYPE NE 2) GO TO 120
C      X(8,NR) = L31
C      Y(8,NR) = Y(7,NR)+TAL(7,NR)*(X(8,NR)-X(7,NR))
C
C      WRITE (6,350) X(8,NR),Y(8,NR)
C
C      AL(8,NR) = ASIN(RIA/RIL*SIN(AL(7,NR)))
C
C      WRITE (6,360) AL(8,NR)
C

```



```

180      XO = X0INIT
190      CONTINUE
C
C      INITIALIZE RBACK
C
      RBACK = RBINIT
      CONTINUE
200      CONTINUE
C
C      INITIALIZE L1 AND L2
C
210      L1 = L1INIT
      L2 = L2INIT
220      CONTINUE
      WRITE (6,280) INDEX
      STOP
C
C      FORMAT STATEMENTS
C
230      FORMAT ('1',10X,'TUBE DIAMETERS ',20X,'REFRACTIVE INDEX ')
240      FORMAT (10X,'OD=',F10 4,22X,'AIR=',F5 3,5X,'LENS=',F5 3)
250      FORMAT (10X,'ID=',F10 4,22X,'TUBE=',F5 3,4X,'COMB=',F5 3)
260      FORMAT (/10X,'BEAM HALF ANGLE ALPHA/2=',F6 4,' DEG ',10X,
      * 'LENS FIRST SURFACE RADIUS=',F8 2,5X,
      * 'LENS SECOND SURFACE RADIUS=',F8 2)
270      FORMAT (/10X,'THK1=',F7 4,5X,'THK2=',F7 4,5X,'L2 INIT =',
      * F7 3,5X,'X INIT=',F7 3,5X,'Y INIT=',F7 3)
280      FORMAT (////10X,'TOTAL NUMBER OF ITERATIONS PERFORMED ',110)
290      FORMAT (4X,'X0',9X,'Y0',8X,'XV',8X,'YV',8X,'XH',8X,'YH',8X,
      * 'XDIFF',5X,'YDIFF',8X,'L2',4X,'ORIENT',4X,'HALF ANG ')
300      FORMAT (/10X,'NYPSTEP=',I3,5X,'YSTEP=',F6 3,5X,'NLSTEP=',I3,
      * 5X,'LSTEP=',F6 3,5X,'NXSTEP=',I3,5X,'XSTEP=',F6 3,5X,
      * 'X TOLERANCE=',F7 4,5X,'Y TOLERANCE=',F7 4)
310      FORMAT (////1X,'UNOBSTRUCTED BEAM',7X,'VERTICAL TRACE',5X,
      * 'HORIZONTAL TRACE',7X,'DIFFERENCES',9X,'LENS',5X,
      * 'BEAM INTERSECTION (DEG)')
320      FORMAT (3F10 0,4F5 0)
330      FORMAT (5F10 0)
340      FORMAT (2I5,3F10 0)
350      FORMAT (10X,2F12 6)
360      FORMAT (15X,1F12 6)
370      FORMAT (2F10 3,6F10 5,F10 3,2F10 5)
380      FORMAT (4F12 6)
390      FORMAT (10X,'VERT VIRT X=',F10 5,' Y=',F10 5,8X,
      * 'HORIZ VIRT X=',F10 5,' Y=',F10 5,8X,'AT L3=',F8 3)
400      FORMAT (3(I10,F10 0))
410      FORMAT (4F10 0)
420      FORMAT (/10X,'LTYPE = 1. THE LENS IS A PLANO-CYLINDRICAL TYPE ')
430      FORMAT (/10X,'LTYPE = 2. THE LENS IS A CYLINDRICAL-PLANO TYPE ')
440      FORMAT (/10X,'LTYPE = 3. THE LENS IS A DOUBLE CYLINDRICAL TYPE ')
450      FORMAT (/10X,'MODE = 1. THE RAY TRACE WILL PROCEED ONLY TO ',
      * 'THE TUBE CENTERLINE ')
460      FORMAT (/10X,'MODE = 2. THE RAY TRACE WILL PROCEED PAST THE ',
      * 'CENTERLINE AND OUT THE SECOND SIDE ')
      END
C
C      THIS SUBROUTINE CALCULATES THE INTERSECTION OF A LINE AND
C      CIRCLE WITH ITS CENTER AT(0,0)
C

```

```

SUBROUTINE STCR1 (XM, XB, XR, POMR, X, Y, ISIGN)
AA = XM*XM+1
BB = XM*XB/AA
CC = (XB*XB-XR*XR)/AA
DD = BB*BB-CC
C
C DETERMINE IF LINE WILL INTERSECT WITH CIRCLE
C
IF (DD LT 0 0) GO TO 10
X = -BB+POMR*SQRT(BB*BB-CC)
Y = XM+X*XB
ISIGN = 0
GO TO 20
10 ISIGN = 1
20 RETURN
END
C
C SUBROUTINE FOR SECOND HALF OF RAY TRACE
C
SUBROUTINE CRUNCH (X1, Y1, R, AL1, RI1, RI2, AL2, TAL)
WRITE (6, 10) X1, Y1
PHI1 = ASIN(Y1/R)
TH1 = PHI1-AL1
U = RI1/RI2*SIN(TH1)
AU = ABS(U)
C
C CHECK FOR TOTAL INTERNAL REFLECTION
C
IF (AU GT 1 0) STOP
TH2 = ASIN(U)
AL2 = PHI1-TH2
WRITE (6, 20) AL2
TAL = TAN(AL2)
10 FORMAT (10X, 2F12 6)
20 FORMAT (15X, F12 6)
END
#EOR

```

APPENDIX B: CORRECTION LENS FABRICATION

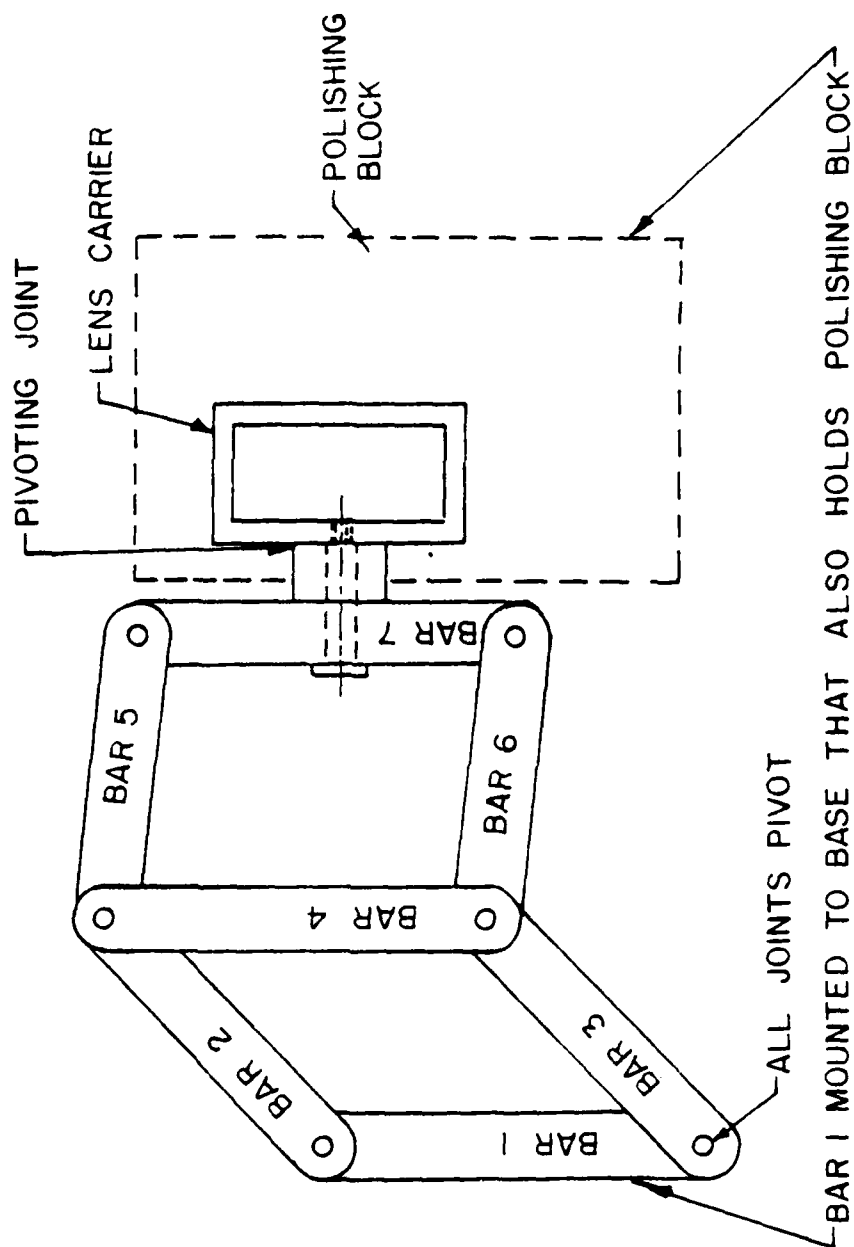
The size and focal length of the correction lenses were such that they were not available as stock items from suppliers. Since the lens shape needed was relatively simple (a plano-concave cylindrical type), the decision was made to fabricate them in-house. Due to the untested design it was desirable to make the grinding and polishing procedure as easy as possible while still maintaining good optical quality. Acrylic plastic was chosen as the lens material because it is softer and easier to work with than glass and will polish much quicker. The finish obtainable is nearly as good as with glass, although plastic lenses are more subject to damage from scratches. This was of little concern for the present application.

The radius of curvature of the required concave surface (47 inches) was relatively large. Several possibilities were considered for grinding and polishing this surface such as a pivoted swinging arm 47 inches long, the free end of which would trace out an arc of the desired radius. Another option was to use a wheel with a smaller radius than the desired radius of the lens, tilt the wheel at an angle, and then use the edge of the wheel so that a larger radius is

approximated. This method does not generate a true circular arc, but the curve that is generated (a portion of an ellipse) would probably be accurate enough in many cases. However, the method finally chosen was to use a numerically controlled milling machine to make a "master" steel block with a convex surface of the proper radius. The lens could then be ground and polished on this block. Using a master block offers the advantages of being faster, easier and more consistent than any of the other methods.

The master block was made twice the dimensions of the lens (4" x 8") to allow room to move the lens in a circular motion for polishing. A circular motion is desired when polishing a lens in order to provide uniform abrasion in all directions instead of one or two preferred directions. When polishing a flat surface or a spherical surface, maintaining a circular motion is easy since the lens can be moved in any direction on the polishing block and the lens can be rotated to any orientation. A cylindrical lens, on the other hand, can be moved in any direction on the polishing block, but lens orientation must be maintained so that the cylindrical axes of the lens and the block are kept parallel.

Maintaining the lens parallel to the polishing block was accomplished with the linkage mechanism shown in Figure B1. The mechanism consists of seven bars, each of the same length, that are attached together with pivoting joints in such a way that when bar 1 is secured, bar 7 is free to move



B.1 Cylindrical Lens Grinding and Polishing Mechanism

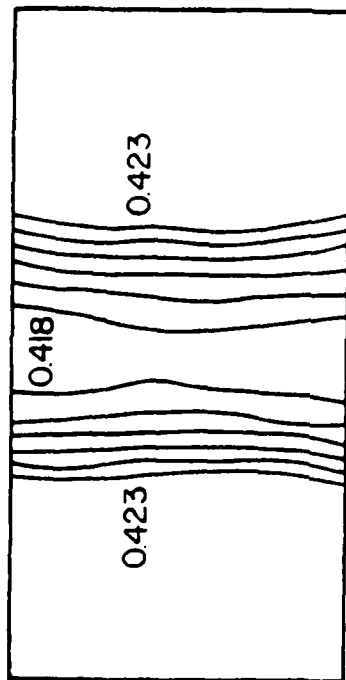
in any direction in a plane but is always kept parallel to bar 1. Bar 1 was fastened to a large plate on which the polishing block was mounted. A carrier fastened to bar 7 held the lens as it was moved over the surface of the polishing block. The carrier was attached by means of a pivoting joint that allowed the carrier and lens to rotate around the cylindrical axis of the lens blank as it was moved over the surface of the block. The inner dimensions of the carrier were slightly larger than the lens providing a slip fit between the lens and carrier. This was done so that the carrier would not interfere with the polishing process as the lens was moved over the polishing block by hand. This apparatus proved to work very well with few difficulties.

Grinding and polishing took place in several steps working from coarse abrasives to fine. The first abrasive used was #240 grit wet sandpaper. This step accounted for most of the material removal from the lens blank. At the end of this step the concave surface of 47 inch radius had been formed.

The second abrasive was #400 grit wet sandpaper. In this intermediate step only a small amount of material was removed, but the size of the abrasions in the surface of the plastic was reduced. This step was completed when all of the larger abrasions from the #240 grit sandpaper had been removed and the entire surface showed only uniform abrasions of smaller depth.

For the third step, #600 grit wet sandpaper was used. This was also an intermediate step to reduce the size of surface abrasions, but since this was the last operation in which a significant amount of material could be removed, the shape of the concave surface was also checked and corrected as necessary. Surface shape was determined by using a dial indicator set up on a surface plate. The flat side of the lens was placed on the surface plate and by moving the lens under the dial indicator the thickness of the lens could be measured at various points and contour lines drawn on the concave lens surface. For a perfectly cylindrical lens, the contour lines would be parallel to one another. The actual surface contours of a lens are shown in Figure B2. This was one of the most tedious steps in the process.

The operations described so far were grinding steps in which essentially all of the material was removed to form the concave surface. In the remaining polishing steps, a negligible amount of material was removed. For the grinding steps, the different grades of sandpaper were fastened directly to the master block. However, since all of the polishes used were either in paste or powder form, a piece of denim was fastened to the block and the polish placed on the denim. As the polishing progressed to finer abrasives, a new piece of denim was placed on the block in order to insure that all of the coarser abrasive was eliminated.



LENS THICKNESSES IN INCHES

B.2 Contour Plot for Concave Lens Surface Near the Vertex

Automotive rubbing compound was initially used for the first polishing operation. The rubbing compound was not fine enough to begin to clear the surface and this step was later determined to be unnecessary. The next abrasive used was toothpaste (Crest gel), followed by jeweller's rouge for the final polishing of the concave surface. Finally, a denim pad was fastened to a flat plate and the planar surface of the lens was polished with toothpaste and then jeweller's rouge to clean up any scratches incurred during the grinding and polishing of the concave side.

The total time required to grind and polish a lens was approximately twelve hours. Most of this time was devoted to developing the proper surface shape - in particular it was difficult to make sure that the lens was of constant thickness at each section parallel to the axis. If a large number of lens elements was to be made it might be worthwhile to design a more sophisticated lens carrier to simplify this part of the process.

APPENDIX C: UNCERTAINTY ANALYSIS

INTRODUCTION

When estimating limits of uncertainty for LDV data, it is important that all sources of uncertainty in the measurements be accounted for, even though many of the sources are not directly related. For the present investigation, three main sources of uncertainty were considered. First, there is the statistical uncertainty due to having a finite set of data samples. Secondly, there is a flow system uncertainty due to drift in the mean flowrate during a run. Finally, there is the uncertainty in the accuracy of the LDV in measuring the flow. The uncertainty in the final results were then estimated by addition in quadrature of the three uncertainties described above. The uncertainties that are quoted correspond to a 95% confidence level wherever possible.

RANDOM AND SYSTEMATIC ERRORS

Uncertainties are classified into two groups: random uncertainties and systematic uncertainties. Random uncertainties are defined as those that can be revealed by repeating the experiment and systematic uncertainties are

defined as those that cannot be revealed in this way. Statistical methods are used to determine random uncertainty and the value of the uncertainty is a function of the number of times the measurement is repeated and the standard deviation of the distribution of measured values. Systematic uncertainties are harder to evaluate and some knowledge of the experiment is usually required in order to detect them [40].

For the present investigation, there is some difficulty in distinguishing between the random and systematic uncertainties. This difficulty comes about because the uncertainty analysis for a single velocity measurement at a given point is different than the analysis for a group of velocity measurements throughout the flow field in the following way. At a given point, the random uncertainty is due mostly to the turbulent fluctuations in the flow and this uncertainty is revealed and analyzed by repeated measurements; in this case 4500 at each point. For the series of point measurements that are required to map out the flow field, however, there is the random uncertainty at each point just described, plus there is a random uncertainty from point to point due to variations in the parameters of the experiment that are too slow to detect with a single point measurement or variations that are caused by the act of moving from one point to the next. Since these last two sources of error vary only from point to point and are essentially constant

during each individual measurement, they constitute a systematic error at a point and are not revealed by the statistics that are performed on the measurements at each point. For this experiment, the mean flow rate through the system was observed to fluctuate, with the time scale of the fluctuations being much longer than the time required to make a velocity measurement. Also, the beam intersection angle was found to vary slightly from point to point due to imperfections in the tube walls. At a given point, these factors constitute a systematic error, but from point to point they are random. Theoretically, it would be possible to measure the "instantaneous" flow rate through the system when each measurement was made and to measure the local beam intersection angle at each point. Each point measurement could then be normalized with the parameters at that point and the uncertainty caused by the point to point fluctuations would be reduced. However, since all of the velocity measurements in this investigation were normalized with the same parameters, the random uncertainty from point to point must be included in the analysis.

STATISTICAL UNCERTAINTY

A statistical error analysis for LDV measurements is given by Yanta [41]. In his paper, Yanta presents plots for the statistical error prediction for the mean velocity and standard deviation computed from an ensemble of LDV data.

The plots are derived from a Student t-distribution for the mean velocity and from a chi-squared distribution analysis for the standard deviation.

The values obtained from the plots show that for an ensemble of 4500 samples, the uncertainty in the mean velocity is less than 0.5%, even for turbulence intensities of 25%. The statistical error prediction for the standard deviation yields an uncertainty of approximately 2.5%.

FLOW SYSTEM UNCERTAINTY

Because of the relatively long time that was required to measure each profile (approximately 2 to 3 hours), it was inevitable that there would be some "drift" in the mean flowrate during the run. Long term fluctuations in the flowrate were suspected because at least 30 to 45 minutes was required for the system to reach steady state after startup. Also, very slow fluctuations were noted in the manometer attached to the pitot probe shown in Figure 8. Obtaining a precise value for the uncertainty in the flowrate is impossible because of the many sources that contribute error. These include variations in atmospheric conditions, air currents in the laboratory, unsteadiness in the blower, and uncertainty in the manometer used to monitor the flowrate to name but a few. By observing the fluctuations of the manometer during a given run and noting the amount of

re-calibration required after the runs, an estimate of the flow system uncertainty was judged to be on the order of $\pm 2\%$ of the mean velocity for both the fully developed pipe flow experiment and the axisymmetric sudden expansion flow experiments. This represents a moderately conservative estimate and is probably within the 95% confidence level.

LDV SYSTEM UNCERTAINTY

First, we shall calculate the possible error for each individual LDV velocity realization. The frequency of a single realization is computed with the equation (from Ref. [30]),

$$f = \frac{N \times 10^8}{D_m \times 2^{n-2}} \quad (C.1)$$

where N (cycles/burst) and n (exponent) are presumed to be exact. The only possible source of error comes from D_m (digital mantissa). Now using the relationship

$$\omega_R = \left[\left(\frac{\partial R}{\partial x_1} \omega_1 \right)^2 + \left(\frac{\partial R}{\partial x_2} \omega_2 \right)^2 + \dots + \left(\frac{\partial R}{\partial x_n} \omega_n \right)^2 \right]^{1/2} \quad (C.2)$$

where R is the functional relationship.

x_1, \dots, x_n are the independent variables.

$\omega_1, \dots, \omega_n$ are uncertainties.

For this case,

$$\omega_f = \left[\left[\frac{\partial f}{\partial D_m} \omega_{D_m} \right]^2 \right]^{1/2} = \frac{\partial f}{\partial D_m} \omega_{D_m} \quad (C.3)$$

since we assume $\omega_N = \omega_n = 0$, i.e. the digital output of the LDV processor is exact. Taking the derivative, we obtain,

$$\omega_f = \frac{N \times 10^8}{D_m^2 \times 2^{n-2}} \omega_{D_m} \quad (C.4)$$

For a typical run in the axisymmetric sudden expansion investigation,

$N = 16$ cycles/burst

$n = 0$

$D_m = 3800$ seconds/burst

$\omega_{D_m} = 8$

hence,

$\omega_f = 3550$ cycles/second.

The equation for the velocity of a particle is:

$$u = [f - f_s] F_R \quad (C.5)$$

and the uncertainty is,

$$\omega_u = \left[\left(F_R \omega_f \right)^2 + \left(-F_R \omega_{fs} \right)^2 + \left([f - f_s] \omega_{F_R} \right)^2 \right]^{1/2} \quad (C.6)$$

where $f = 16,840,000$

$f_s = 10,000,000$

$F_R = 4.15 \times 10^{-6}$

$\omega_f = 3550$

$\omega_{fs} = 1000$

$\omega_{F_R} = 0.10 \times 10^{-6}$

Solving,

$$\omega_u = 0.68 \text{ m/sec}$$

and it is found that this uncertainty is almost entirely due to the uncertainty in the fringe spacing, ω_{F_R} . The value of the uncertainty is approximately 2% of the mean flowrate. This same analysis was performed using parameters that were typical of the fully developed pipe flow and similar results were obtained for the uncertainty, 2% of the mean flow. This is because in both cases, practically all of the uncertainty was due to ω_{F_R} . The uncertainty in the fringe spacing was due to imperfection in the correction lens and the tube wall.

UNCERTAINTY DUE TO GROUPING OF DATA

As mentioned previously, it was assumed that most of the experimental uncertainty was accounted for in the three categories that were discussed. Inevitably there is some source of error that may not be accounted for in the standard uncertainty analysis. One such error that is not taken into account by the statistical analysis is the error caused by grouping of the samples in the velocity histogram. With LDV measurements, grouping of the data occurs because the LDV signal processor is a discrete instrument. The time measurement that is used to calculate the Doppler frequency is made with a digital clock. The resolution of the time measurement depends on the length of the clock cycles. In an ideal situation, the N-cycle time that the processor measures is several orders of magnitude longer than the clock cycle and the resolution of the time measurement is negligible. In some cases, however, the N-cycle time may be short enough that the clock resolution will cause the data to be grouped. For example, if an LDV is operating with a 10 MHz frequency shift, a fringe spacing of $\approx 4.2 \mu\text{m}$ and measuring a flow with a mean velocity of $\approx 8 \text{ m/s}$ (this was the situation for the straight pipe flow tests), the measurement resolution of a TSI model 1980 processor with a 2ns clock resolution is approximately 0.08 m/s. In this case, the resolution of the LDV system is about 1% of the mean flow velocity and is the same order as the standard devia-

tion of the velocity. The effect of this coarse resolution is that the data is grouped into discrete bands in the velocity histogram. The grouping will cause an error when the moments of the data are calculated with the ordinary methods.

There are a couple of ways to correct for grouping of the data. The best way is obviously to improve the resolution of the LDV measurement by reducing the frequency shift and consequently increasing the N-cycle time. Another method is Sheppard's correction for grouped data. This method states that the grouped data approximation to the variance may be improved by adding Sheppard's correction, $-c^2/12$, where c is the resolution of the measurement. There are also corrections for the higher statistical moments.

This correction scheme was applied to the data that were taken in the fully developed turbulent pipe flow and the effect of the correction was negligible. Even though Sheppard's correction failed to change the variances that were measured in the fully developed pipe flow, it was still felt that these values were too high. At this point the following measurements that were made on the centerline of a fully developed pipe flow for another purpose were observed.

| <u>N-cycle count</u> | <u>resolution</u> | <u>std. dev.</u> |
|----------------------|-------------------|------------------|
| 16 | 0.08 | 0.49 |
| 8 | 0.15 | 0.57 |
| 4 | 0.30 | 0.83 |
| 2 | 0.60 | 1.41 |

All measurements were made at the same point in the flow; only the number of cycles counted on the LDV processor was changed between runs. It is easy to see that for these four runs, the measured standard deviation and hence the variance, increased as the measurement resolution got coarse. A correction scheme similar to Sheppard's correction was assumed:

$$\text{actual variance} = \text{grouped data variance} - Ac^2 \quad (\text{C.7})$$

where C is the resolution of the measurement and A is some constant (1/12 for Sheppard's correction). The measured values of grouped data variances and measurement resolution were plotted to determine a value for A. Using a least squares fit method, the value of A was found to be approximately 5.

This correction was then applied to the measurements in the turbulent pipe flow. The turbulence intensity measured in the sudden expansion flows was much higher than in the fully developed flow. Because of this, the standard deviation of the velocity was much larger than the resolution of

the LDV and the effect of the data grouping was found to be negligible.

UNCERTAINTY IN THE RESULTS

Calculating the root mean square of the individual uncertainties gives the following results. For the mean velocity

$$\frac{\omega_{U_o}}{U_o} = [0.005^2 + 0.02^2 + 0.02^2]^{1/2} \quad (C.8)$$

and the estimated uncertainty is $\pm 3\%$ of the mean centerline velocity. The result for the turbulence intensity is

$$\frac{\omega_{u'}}{u'} = [0.025^2 + 0.02^2 + 0.02^2]^{1/2} \quad (C.9)$$

This predicts an uncertainty of $\pm 4\%$ in these measurements.

This estimate of the turbulence intensity uncertainty may then be used to calculate the uncertainty in the Reynolds stress and Turbulence kinetic energy. Applying the uncertainty equation [C.2] to Logan's method for calculating Reynolds stress

$$2\overline{u'v'} = \sigma_{+45}^2 - \sigma_{-45}^2 \quad (9)$$

AD-A146 206

LASER VELOCIMETER MEASUREMENTS AND ANALYSIS IN
TURBULENT FLOWS WITH COMBU..(U) PURDUE UNIV LAFAYETTE
IN SCHOOL OF MECHANICAL ENGINEERING

3/3

UNCLASSIFIED

H D THOMPSON ET AL. JUL 84

F/G 20/5

NL

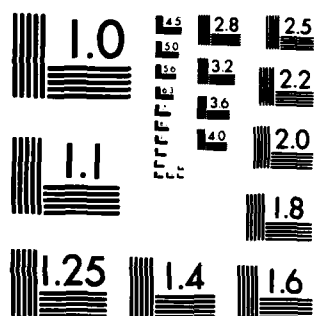
END

DATE

FILED

11 84

DTIC



MICROCOPY RESOLUTION TEST CHART
NATIONAL BUREAU OF STANDARDS-1963-A

$$\omega_R = \left[\left\{ \sigma_{+45} \omega_\sigma \right\}^2 + \left\{ -\sigma_{-45} \omega_\sigma \right\}^2 \right]^{1/2} \quad (C.10)$$

Since we have estimated the uncertainty in the standard deviation to be 4%, this can be reduced to

$$\omega_R = \left[\left\{ 0.04 \sigma_{+45}^2 \right\}^2 + \left\{ 0.04 \sigma_{-45}^2 \right\}^2 \right]^{1/2} \quad (C.11)$$

For the fully developed pipe flow, a typical value of $\sigma = 0.55$ yields a non-dimensionalized value of

$$\frac{\omega_R}{U_o^2} \times 1000 = 0.3$$

Observing the experimental results it can be seen that many of the values differ from the theoretical Reynolds stress profile by more than this amount.

The values of turbulence intensity that were measured in the sudden expansion varied over a wide range from less than 2% to over 25%. This will cause the uncertainty to vary from point to point, but for a worst case the normalized uncertainty is estimated to be

$$\frac{\omega_R}{U_o^2} \times 10 = 0.015$$

Finally, an estimate for the uncertainty in the Turbulence kinetic energy measurements is carried out in the same manner. Logan's equation for TKE:

$$\overline{u'^2} + \overline{v'^2} = \sigma_{+45}^2 + \sigma_{-45}^2 \quad (10)$$

Applying Equation C.2;

$$\omega_{TKE} = \left[\left(2\sigma_{+45} \omega_{\sigma} \right)^2 + \left(2\sigma_{-45} \omega_{\sigma} \right)^2 \right]^{1/2} \quad (C.12)$$

and substituting $\omega_{\sigma} = 0.04\sigma$

$$\omega_{TKE} = \left[\left(0.08 \sigma_{+45}^2 \right)^2 + \left(0.08 \sigma_{-45}^2 \right)^2 \right]^{1/2} \quad (C.13)$$

This gives an uncertainty for the sudden expansion measurements of approximately

$$\frac{\omega_{TKE}}{2U_o^2} = 0.002$$

Turbulence kinetic energy was not reported for the fully developed flow.

APPENDIX D: EXPERIMENTAL DATA

Table D1. Experimental Data from the
Turbulent Pipe Flow.

| Radius (mm) | Angle | Velocity | |
|-------------|-------|----------|----------|
| | | mean | std.dev. |
| -38.0 | 0.0 | 6.331 | 0.695 |
| -36.0 | 0.0 | 6.618 | 0.673 |
| -32.0 | 0.0 | 6.879 | 0.656 |
| -28.0 | 0.0 | 7.261 | 0.619 |
| -24.0 | 0.0 | 7.590 | 0.583 |
| -20.0 | 0.0 | 7.766 | 0.552 |
| -16.0 | 0.0 | 7.954 | 0.500 |
| -12.0 | 0.0 | 8.123 | 0.451 |
| -8.0 | 0.0 | 8.183 | 0.435 |
| -4.0 | 0.0 | 8.289 | 0.405 |
| 0.0 | 0.0 | 8.294 | 0.418 |
| 4.0 | 0.0 | 8.215 | 0.402 |
| 8.0 | 0.0 | 8.252 | 0.449 |
| 12.0 | 0.0 | 8.055 | 0.504 |
| 16.0 | 0.0 | 7.792 | 0.562 |
| 20.0 | 0.0 | 7.506 | 0.576 |
| 24.0 | 0.0 | 7.401 | 0.583 |
| 28.0 | 0.0 | 7.125 | 0.599 |
| 32.0 | 0.0 | 6.955 | 0.623 |
| 36.0 | 0.0 | 6.677 | 0.695 |
| 38.0 | 0.0 | 6.449 | 0.721 |
| 0.0 | 90.0 | -0.129 | 0.346 |
| 4.0 | 90.0 | -0.119 | 0.333 |
| 8.0 | 90.0 | -0.127 | 0.361 |
| 12.0 | 90.0 | -0.085 | 0.332 |
| 16.0 | 90.0 | -0.080 | 0.367 |
| 20.0 | 90.0 | -0.109 | 0.379 |
| 24.0 | 90.0 | -0.114 | 0.388 |
| 28.0 | 90.0 | -0.124 | 0.381 |
| 32.0 | 90.0 | -0.125 | 0.414 |
| 36.0 | 90.0 | -0.225 | 0.392 |

The following were measured on the horizontal axis
to check the flow symmetry.

| | | | |
|------|-----|-------|-------|
| 0.0 | 0.0 | 8.294 | 0.418 |
| 4.0 | 0.0 | 8.168 | 0.441 |
| 8.0 | 0.0 | 8.081 | 0.455 |
| 12.0 | 0.0 | 8.055 | 0.465 |
| 16.0 | 0.0 | 7.897 | 0.511 |
| 20.0 | 0.0 | 7.784 | 0.509 |
| 24.0 | 0.0 | 7.670 | 0.553 |
| 28.0 | 0.0 | 7.470 | 0.606 |
| 32.0 | 0.0 | 7.147 | 0.637 |
| 36.0 | 0.0 | 6.843 | 0.680 |

Table D1. Continued

| Radius (mm) | Angle | Velocity | |
|-------------|-------|----------|----------|
| | | mean | std.dev. |
| 0.0 | 45.0 | 5.638 | 0.356 |
| 4.0 | 45.0 | 5.619 | 0.425 |
| 8.0 | 45.0 | 5.555 | 0.445 |
| 12.0 | 45.0 | 5.496 | 0.499 |
| 16.0 | 45.0 | 5.284 | 0.564 |
| 20.0 | 45.0 | 5.165 | 0.585 |
| 24.0 | 45.0 | 4.923 | 0.591 |
| 28.0 | 45.0 | 4.770 | 0.527 |
| 32.0 | 45.0 | 4.636 | 0.595 |
| 36.0 | 45.0 | 4.467 | 0.629 |
| 0.0 | -45.0 | 5.865 | 0.373 |
| 4.0 | -45.0 | 5.848 | 0.369 |
| 8.0 | -45.0 | 5.732 | 0.357 |
| 12.0 | -45.0 | 5.638 | 0.382 |
| 16.0 | -45.0 | 5.409 | 0.409 |
| 20.0 | -45.0 | 5.314 | 0.414 |
| 24.0 | -45.0 | 5.121 | 0.417 |
| 28.0 | -45.0 | 5.049 | 0.436 |
| 32.0 | -45.0 | 4.968 | 0.466 |
| 36.0 | -45.0 | 4.659 | 0.489 |
| 0.0 | 45.0 | 5.799 | 0.365 |
| 4.0 | 45.0 | 5.794 | 0.404 |
| 8.0 | 45.0 | 5.691 | 0.438 |
| 12.0 | 45.0 | 5.581 | 0.492 |
| 16.0 | 45.0 | 5.458 | 0.550 |
| 20.0 | 45.0 | 5.274 | 0.571 |
| 24.0 | 45.0 | 5.107 | 0.575 |
| 28.0 | 45.0 | 4.966 | 0.557 |
| 32.0 | 45.0 | 4.824 | 0.568 |
| 36.0 | 45.0 | 4.708 | 0.620 |
| 0.0 | -45.0 | 5.903 | 0.372 |
| 4.0 | -45.0 | 5.792 | 0.364 |
| 8.0 | -45.0 | 5.775 | 0.350 |
| 12.0 | -45.0 | 5.681 | 0.380 |
| 16.0 | -45.0 | 5.532 | 0.393 |
| 20.0 | -45.0 | 5.378 | 0.403 |
| 24.0 | -45.0 | 5.182 | 0.418 |
| 28.0 | -45.0 | 5.110 | 0.437 |
| 32.0 | -45.0 | 4.889 | 0.538 |
| 36.0 | -45.0 | 4.775 | 0.531 |

Table D1. Continued

The following were measured prior to the addition of the plenum chamber.

| Radius (mm) | Angle | Velocity | |
|-------------|-------|----------|----------|
| | | mean | std.dev. |
| 0.0 | 45.0 | 5.863 | 0.334 |
| 4.0 | 45.0 | 5.866 | 0.353 |
| 8.0 | 45.0 | 5.827 | 0.391 |
| 12.0 | 45.0 | 5.791 | 0.473 |
| 16.0 | 45.0 | 5.633 | 0.538 |
| 20.0 | 45.0 | 5.357 | 0.582 |
| 24.0 | 45.0 | 5.036 | 0.577 |
| 28.0 | 45.0 | 4.705 | 0.555 |
| 32.0 | 45.0 | 4.444 | 0.564 |
| 36.0 | 45.0 | 4.206 | 0.578 |
| 0.0 | -45.0 | 5.816 | 0.418 |
| 4.0 | -45.0 | 5.918 | 0.380 |
| 8.0 | -45.0 | 5.750 | 0.356 |
| 12.0 | -45.0 | 5.807 | 0.385 |
| 16.0 | -45.0 | 5.544 | 0.382 |
| 20.0 | -45.0 | 5.351 | 0.371 |
| 24.0 | -45.0 | 5.158 | 0.407 |
| 28.0 | -45.0 | 4.877 | 0.382 |
| 32.0 | -45.0 | 4.588 | 0.421 |
| 36.0 | -45.0 | 4.318 | 0.445 |
| 0.0 | 45.0 | 5.907 | 0.282 |
| 4.0 | 45.0 | 5.953 | 0.308 |
| 8.0 | 45.0 | 5.951 | 0.351 |
| 12.0 | 45.0 | 5.800 | 0.408 |
| 16.0 | 45.0 | 5.679 | 0.486 |
| 20.0 | 45.0 | 5.379 | 0.538 |
| 24.0 | 45.0 | 5.079 | 0.553 |
| 28.0 | 45.0 | 4.817 | 0.549 |
| 32.0 | 45.0 | 4.551 | 0.527 |
| 36.0 | 45.0 | 4.272 | 0.545 |
| 0.0 | -45.0 | 5.747 | 0.396 |
| 4.0 | -45.0 | 5.795 | 0.356 |
| 8.0 | -45.0 | 5.787 | 0.327 |
| 12.0 | -45.0 | 5.705 | 0.325 |
| 16.0 | -45.0 | 5.590 | 0.351 |
| 20.0 | -45.0 | 5.330 | 0.386 |
| 24.0 | -45.0 | 5.089 | 0.396 |
| 28.0 | -45.0 | 4.830 | 0.409 |
| 32.0 | -45.0 | 4.578 | 0.419 |
| 36.0 | -45.0 | 4.306 | 0.426 |

Table D2. Experimental Data from the
1.90:1 Axisymmetric Sudden Expansion.

| Axial location: 2 step heights | | Probe Volume Orientation | | | |
|--------------------------------|----------|--------------------------|--------|---------|---------|
| Radius (mm) | | 0 deg | 90 deg | +45 deg | -45 deg |
| 0. | mean | 27.872 | -1.038 | 20.092 | 18.841 |
| | std.dev. | 0.431 | 0.548 | 0.678 | 0.518 |
| -7.20 | | 27.931 | -0.727 | 19.561 | 19.667 |
| | | 0.458 | 0.585 | 0.516 | 0.555 |
| -14.40 | | 27.893 | -0.635 | 19.476 | 20.009 |
| | | 0.747 | 0.818 | 0.726 | 0.866 |
| -19.20 | | 27.138 | -0.863 | 18.503 | 19.411 |
| | | 1.799 | 1.755 | 1.646 | 2.328 |
| -21.60 | | 23.793 | -1.336 | 15.526 | 16.309 |
| | | 4.185 | 2.944 | 2.916 | 4.982 |
| -24.00 | | 15.426 | -1.114 | 10.238 | 10.814 |
| | | 5.935 | 3.976 | 3.648 | 6.241 |
| -26.40 | | 8.763 | -0.784 | 5.340 | 5.430 |
| | | 5.588 | 4.149 | 3.478 | 5.887 |
| -28.80 | | 3.119 | 0.034 | 1.915 | 1.239 |
| | | 4.627 | 3.238 | 2.929 | 4.504 |
| -33.60 | | -1.423 | 0.786 | -0.536 | -1.602 |
| | | 2.783 | 1.738 | 1.966 | 2.618 |
| -38.40 | | -1.820 | 0.629 | -0.875 | -1.775 |
| | | 2.523 | 1.609 | 2.008 | 2.407 |
| -43.20 | | -1.703 | 0. | -0.883 | -1.171 |
| | | 2.722 | 0. | 2.587 | 2.277 |
| Axial location: 4 step heights | | | | | |
| 0. | mean | 27.484 | 0.336 | 19.241 | 19.440 |
| | std.dev. | 0.929 | 0.722 | 0.871 | 0.821 |
| -7.20 | | 27.685 | -0.045 | 19.230 | 19.784 |
| | | 0.803 | 0.838 | 0.749 | 0.823 |
| -14.40 | | 27.346 | -0.146 | 18.840 | 19.546 |
| | | 1.765 | 1.519 | 1.380 | 1.633 |
| -19.20 | | 23.272 | -0.664 | 16.346 | 17.661 |
| | | 4.626 | 2.882 | 2.770 | 4.093 |
| -21.60 | | 19.989 | -0.613 | 13.869 | 14.997 |
| | | 5.763 | 3.497 | 3.561 | 5.640 |
| -24.00 | | 15.957 | -0.653 | 10.910 | 11.783 |
| | | 6.344 | 4.016 | 3.971 | 6.397 |
| -26.40 | | 11.561 | -0.803 | 8.118 | 8.906 |
| | | 6.557 | 4.199 | 4.170 | 6.606 |
| -28.80 | | 7.541 | -0.598 | 5.323 | 6.248 |
| | | 6.535 | 4.199 | 4.156 | 6.398 |
| -33.60 | | 1.679 | -0.299 | 1.126 | 1.446 |
| | | 5.617 | 3.513 | 3.737 | 5.592 |
| -38.40 | | -1.837 | -0.084 | -1.338 | -1.330 |
| | | 4.602 | 2.586 | 3.154 | 4.285 |
| -43.20 | | -3.540 | 0. | -2.327 | -2.664 |
| | | 3.560 | 0. | 2.866 | 2.999 |

Table D2. Continued

| Axial location: 6 step heights | | Probe Volume Orientation | | | |
|--------------------------------|----------|--------------------------|--------|---------|---------|
| Radius (mm) | | 0 deg | 90 deg | +45 deg | -45 deg |
| 0. | mean | 26.341 | 0.282 | 18.496 | 18.611 |
| | std.dev. | 1.157 | 1.089 | 1.178 | 1.118 |
| -7.20 | | 26.541 | -0.150 | 18.319 | 19.017 |
| | | 1.345 | 1.277 | 1.199 | 1.367 |
| -14.40 | | 24.581 | -0.537 | 16.938 | 18.246 |
| | | 3.434 | 2.381 | 2.235 | 3.057 |
| -19.20 | | 20.093 | -0.805 | 13.942 | 15.445 |
| | | 5.793 | 3.400 | 3.638 | 5.210 |
| -21.60 | | 17.311 | -0.872 | 11.933 | 13.181 |
| | | 6.422 | 3.766 | 4.094 | 6.143 |
| -24.00 | | 14.320 | -1.117 | 9.639 | 11.223 |
| | | 6.865 | 4.109 | 4.369 | 6.666 |
| -26.40 | | 11.361 | -0.976 | 7.472 | 8.870 |
| | | 7.030 | 4.310 | 4.533 | 6.869 |
| -28.80 | | 8.636 | -0.938 | 5.624 | 6.856 |
| | | 6.953 | 4.339 | 4.567 | 6.812 |
| -33.60 | | 3.385 | -0.791 | 2.168 | 3.326 |
| | | 6.332 | 4.040 | 4.261 | 6.278 |
| -38.40 | | -0.180 | 0.000 | -0.313 | 0.038 |
| | | 5.400 | 3.533 | 3.761 | 5.201 |
| -43.20 | | -2.591 | 0. | -0.973 | -1.333 |
| | | 4.187 | 0. | 3.489 | 3.675 |
| Axial location: 8 step heights | | | | | |
| 0. | mean | 24.679 | 0.052 | 17.381 | 17.448 |
| | std.dev. | 2.152 | 1.757 | 1.907 | 1.906 |
| -7.20 | | 24.301 | -0.360 | 16.836 | 17.283 |
| | | 2.531 | 2.156 | 2.215 | 2.674 |
| -14.40 | | 21.139 | -0.670 | 14.153 | 15.424 |
| | | 4.963 | 3.287 | 3.428 | 4.686 |
| -19.20 | | 17.360 | -1.012 | 11.333 | 12.766 |
| | | 6.277 | 3.907 | 4.200 | 6.132 |
| -21.60 | | 15.140 | -0.958 | 9.787 | 11.351 |
| | | 6.680 | 4.124 | 4.393 | 6.399 |
| -24.00 | | 13.073 | -1.063 | 8.215 | 9.866 |
| | | 6.911 | 4.208 | 4.399 | 6.643 |
| -28.80 | | 8.945 | -1.031 | 5.168 | 6.716 |
| | | 6.735 | 4.269 | 4.507 | 6.653 |
| -33.60 | | 5.030 | -0.915 | 3.025 | 3.966 |
| | | 6.122 | 4.055 | 4.215 | 6.136 |
| -36.00 | | 3.539 | -0.744 | 1.855 | 2.841 |
| | | 5.786 | 3.768 | 4.030 | 5.478 |
| -38.40 | | 2.187 | -0.468 | 0.860 | 2.954 |
| | | 5.323 | 3.433 | 3.783 | 4.989 |
| -43.20 | | -0.413 | 0. | -0.095 | 0.106 |
| | | 4.286 | 0. | 3.365 | 3.760 |

Table D2. Continued

| Axial location: 12 step heights | | Probe Volume Orientation | | | |
|---------------------------------|----------|--------------------------|--------|---------|---------|
| Radius (mm) | | 0 deg | 90 deg | +45 deg | -45 deg |
| 0. | mean | 16.777 | 0.062 | 11.913 | 12.128 |
| | std.dev. | 5.426 | 3.733 | 4.798 | 4.502 |
| -7.20 | | 16.407 | -0.279 | 11.391 | 11.968 |
| | | 5.640 | 3.861 | 4.451 | 5.119 |
| -14.40 | | 13.973 | -0.532 | 9.684 | 10.519 |
| | | 5.871 | 3.848 | 4.295 | 5.781 |
| -19.20 | | 12.072 | -0.515 | 8.137 | 9.117 |
| | | 5.676 | 3.959 | 4.167 | 5.814 |
| -24.00 | | 9.923 | -0.692 | 6.582 | 7.557 |
| | | 5.671 | 3.853 | 3.920 | 5.789 |
| -28.80 | | 8.133 | -0.571 | 5.394 | 6.183 |
| | | 5.289 | 3.873 | 3.671 | 5.401 |
| -33.60 | | 6.128 | -0.479 | 3.927 | 4.635 |
| | | 4.769 | 3.412 | 3.416 | 4.891 |
| -38.40 | | 4.702 | -0.325 | 3.181 | 3.403 |
| | | 4.310 | 2.933 | 3.145 | 4.128 |
| -43.20 | | 3.199 | 8.295 | 2.528 | 1.934 |
| | | 3.859 | 5.533 | 3.309 | 3.600 |
| Axial location: 20 step heights | | | | | |
| 0. | mean | 8.777 | -0.044 | 6.088 | 6.320 |
| | std.dev. | 3.165 | 2.557 | 2.858 | 2.844 |
| -7.20 | | 8.649 | -0.126 | 6.046 | 6.301 |
| | | 3.130 | 2.516 | 2.750 | 2.922 |
| -14.40 | | 8.393 | -0.127 | 5.723 | 5.988 |
| | | 3.044 | 2.468 | 2.577 | 2.938 |
| -19.20 | | 8.177 | -0.154 | 5.626 | 5.878 |
| | | 3.046 | 2.407 | 2.433 | 2.901 |
| -24.00 | | 7.845 | -0.094 | 5.327 | 5.557 |
| | | 2.980 | 2.331 | 2.405 | 2.941 |
| -28.80 | | 7.378 | -0.159 | 5.097 | 5.321 |
| | | 2.865 | 2.201 | 2.326 | 2.828 |
| -33.60 | | 7.061 | -0.113 | 4.861 | 5.028 |
| | | 2.792 | 2.063 | 2.246 | 2.633 |
| -38.40 | | 6.778 | -0.101 | 4.722 | 4.676 |
| | | 2.737 | 1.733 | 2.146 | 2.419 |
| -43.20 | | 6.138 | -0.108 | 4.234 | 4.571 |
| | | 2.601 | 1.226 | 2.009 | 2.757 |

Table D3. Experimental Data from the
2.70:1 Axisymmetric Sudden Expansion.

| Location x | (mm) r | Axial mean | (m/s) std.dev. | Radial mean | (m/s) std.dev. |
|---------------|-----------|---------------|-------------------|----------------|-------------------|
| 3.00 | -19.20 | 1.7501 | 2.7609 | 0.5152 | 1.1669 |
| 3.00 | -24.00 | -0.2098 | 1.6485 | 0.1864 | 1.9262 |
| 3.00 | -28.80 | -0.2458 | 1.6123 | -0.1777 | 2.0729 |
| 3.00 | -33.60 | -0.1585 | 1.4972 | -0.0542 | 2.4903 |
| 3.00 | -38.40 | -0.0046 | 1.3917 | -0.5030 | 1.8077 |
| 3.00 | -44.20 | 0.0738 | 1.2951 | | |
| 9.00 | -19.20 | 13.4068 | 8.7835 | 0.3149 | 4.8773 |
| 9.00 | -24.00 | -0.5201 | 2.2946 | 0.7627 | 1.5865 |
| 9.00 | -28.80 | -0.5298 | 2.1195 | 0.2022 | 1.7463 |
| 9.00 | -33.60 | -0.3146 | 2.0696 | 0.1784 | 2.2174 |
| 9.00 | -38.40 | -0.1186 | 1.9521 | -0.1507 | 1.8527 |
| 9.00 | -44.20 | 0.4220 | 1.8794 | | |
| 15.00 | -19.20 | 20.6792 | 8.4058 | -0.9438 | 6.1718 |
| 15.00 | -24.00 | -0.9347 | 2.5124 | 1.0896 | 1.5151 |
| 15.00 | -28.80 | -0.8082 | 2.3449 | 0.5770 | 1.6660 |
| 15.00 | -33.60 | -0.5762 | 2.2696 | 0.2499 | 1.7206 |
| 15.00 | -38.40 | -0.1638 | 2.2001 | 0.0637 | 1.6763 |
| 15.00 | -44.20 | 0.6464 | 2.3031 | | |
| 22.50 | -19.20 | 21.9911 | 7.8800 | -0.8729 | 5.7936 |
| 22.50 | -24.00 | -1.0420 | 2.9490 | 1.1055 | 1.8180 |
| 22.50 | -28.80 | -1.1521 | 2.5497 | 0.7382 | 1.6631 |
| 22.50 | -33.60 | -0.7903 | 2.4652 | 0.3781 | 1.7425 |
| 22.50 | -38.40 | -0.2376 | 2.4723 | 0.2753 | 1.5771 |
| 22.50 | -44.20 | 0.5275 | 2.6328 | | |
| 30.00 | -19.20 | 22.4733 | 7.7582 | -1.0033 | 5.8340 |
| 30.00 | -24.00 | 0.2630 | 3.9808 | 0.8482 | 2.6648 |
| 30.00 | -28.80 | -1.4791 | 2.7662 | 0.8957 | 1.7771 |
| 30.00 | -33.60 | -1.0184 | 2.6700 | 0.5963 | 1.7169 |
| 30.00 | -38.40 | -0.4676 | 2.7013 | 0.3460 | 1.5255 |
| 30.00 | -44.20 | 0.2963 | 2.8120 | | |
| 37.50 | -19.20 | 22.5565 | 7.9519 | -0.7835 | 5.7878 |
| 37.50 | -24.00 | 2.7235 | 5.2320 | 0.6728 | 3.5007 |
| 37.50 | -28.80 | -1.5174 | 2.9276 | 0.9552 | 1.8568 |
| 37.50 | -33.60 | -1.3414 | 2.8691 | 0.7030 | 1.7055 |
| 37.50 | -38.40 | -0.7109 | 2.8871 | 0.4039 | 1.5667 |
| 37.50 | -44.20 | -0.0078 | 3.0353 | | |
| 45.00 | -19.20 | 23.1347 | 7.9386 | -0.9181 | 5.6621 |
| 45.00 | -24.00 | 4.8518 | 6.1715 | 0.3227 | 4.3134 |
| 45.00 | -28.80 | -1.2777 | 3.3951 | 0.9375 | 2.1468 |
| 45.00 | -33.60 | -1.5848 | 3.0129 | 0.7841 | 1.7690 |
| 45.00 | -38.40 | -1.0781 | 3.1196 | 0.5249 | 1.5937 |
| 45.00 | -44.20 | -0.4228 | 3.1768 | | |

LIST OF REFERENCES

1. Eaton, J.K., and Johnston, J.P., "An Evaluation of Data for Backward-Facing Step Flow: Report prepared for the 1980/81 Conferences on Complex Turbulent Flows," Dept. of Mechanical Engineering, Stanford University, 1980.
2. Roesler, T., Stevenson, W.H., and Thompson, H.D., "Investigation of Bias Errors in Laser Doppler Velocimeter Measurements," AFWAL-TR-80-2108, December 1980.
3. Bremmer, R., Thompson, H.D., Stevenson, W.H., "An Experimental and Numerical Comparison of Turbulent Flow Over a Step," AFWAL-TR-80-2105, December 1980.
4. Stevenson, W.H., Thompson, H.D., and Roesler, T.C., "Direct Measurement of Laser Velocimeter Bias Errors in a Turbulent Flow," AIAA Journal, 1982. (To be published)
5. Stevenson, W.H., Thompson, H.D., and Gould, R.D., "Laser Velocimeter Measurements and Analysis in Turbulent Flows and Combustion," AFWAL-TR-82-2076, Part II, July 1983.
6. Bradshaw, P., and Wong, F.Y.F., "The Reattachment and Relaxation of a Turbulent Shear Layer," Journal of Fluid Mechanics, Vol. 52, Part 1, pp. 113-135, 1972.
7. Kim, J., Kline, S.J., and Johnston, J.P., "Investigation of a Reattaching Turbulent Shear Layer: Flow Over a Backward Facing Step," Journal of Fluids Engineering, Vol. 102, pp. 302-308, September 1980.
8. Macagno, E.O., and Hung, T.K., "Computational and Experimental Study of a Captive Annular Eddy," Journal of a Fluid Mechanics, Vol. 28, Part I, pp. 43-63, 12 April 1967.
9. Zemanick, P.P., and Dougall, R.S., "Local Heat Transfer Downstream of an Abrupt Circular Channel Expansion," ASME Journal of Heat Transfer, Vol. 92, pp. 53-60, February 1970.

LIST OF REFERENCES (cont'd)

10. Driver, D.M., and Seegmiller, H.L., "Features of a Reattaching Turbulent Shear Layer Subject to an Adverse Pressure Gradient," AIAA-82-1029, AIAA/ASME Third Joint Thermophysics, Fluids, Plasma and Heat Transfer Conference, St. Louis, Missouri, June 1982.
11. Back, L.H., and Roschke, E.J., "Shear-Layer Flow Regimes and Wave Instabilities and Reattachment Lengths Downstream of an Abrupt Circular Channel Expansion," ASME Journal of Applied Mechanics, Vol. 945, pp. 677-681, September 1972.
12. Moon, L.F., and Rudinger, G., "Velocity Distribution in an Abruptly Expanding Circular Duct," ASME Journal of Fluids Engineering, Vol. 99, pp. 226-230, March 1977.
13. Kangovi, S., and Page, R.H., "Subsonic Turbulent Flow Past a Downstream Facing Annular Step," ASME Journal of Fluids Engineering, Vol. 101, pp. 230-236, June 1979.
14. Freeman, A.R., "Laser Anemometer Measurements in the Recirculating Region Downstream of a Sudden Pipe Expansion," In Proceedings of the LDA Symposium Copenhagen, pp. 704-709, 1975.
15. Gosman, A.D., Khalil, E.E., and Whitelaw, J.H., "The Calculation of Two-Dimensional Turbulent Recirculating Flows," Turbulent Shear Flows I, Springer-Verlag, New York, pp. 13.35-13.45, 1977.
16. Drewry, J.E., "Fluid Dynamic Characterization of Sudden Expansion Ramjet Combustor Flowfields," AIAA Journal, Vol. 16, No. 4, pp. 313-319, 1979.
17. Stevenson, W.H., Thompson, H.D., and Lucnik, T.S., "Laser Velocimeter Measurements and Analysis in Turbulent Flows with Combustion," AFWAL-TR-82-2076, Part 1, September, 1982.
18. Eaton, J.K., Johnston, J.P., and Jeans, A.H., "Measurements in a Reattachment Turbulent Shear Layer," 2nd Symposium on Turbulent Shear Flows, Imperial College, London, 2-4 July 1979.
19. Kuehn, D.M., "Effects of Adverse Pressure Gradient on the Incompressible Reattaching Flow over a Rearward-Facing Step," AIAA Journal, Vol. 18, No. 3, pp. 343-344, March 1980.

LIST OF REFERENCES (cont'd)

20. de Brederode, V., and Bradshaw, P., "Three-Dimensional Flow in Nominally Two-Dimensional Separation Bubbles; I. Flow Behind a Rearward Facing Step," Imperial College Aero Report 72-19, August 1972.
21. Harlow, F.H., and Nakayama, P., "Transport of Turbulence Decay Rate," Los Alamos Science Laboratory, University of California Report LA-3854, 1968.
22. Launder, B.E., Morse, A., Rodi, W., and Spalding, D.B., "The Prediction of Free Shear Flows - A Comparison of the Performance of Six Turbulence Models," In: Proceedings of NASA Conference on Free Shear Flows, Langley, 1972.
23. Lokrou, V.D., and Shen, H.W., "Analysis of the Characteristics of Flow in Sudden Expansion by Similarity Approach," Journal of Hydraulic Research, Vol. 21, No. 2, pp. 119-132, 1983.
24. Martin, F., and Goucat, P., "Power Spectral Density of the Three Velocity Components in a Turbulent Flow at High Temperature," International Symposium on Applications to Fluid Mechanics, Lisbon, 1981.
25. Boadway, J.D., and Karahan, E., "Correction of Laser Doppler Anemometry Readings for Refraction at Cylindrical Interfaces," DISA Information, No. 26, 1981.
26. Bicen, A.F., "Refraction Correction for LDA Measurements in Flows with Curved Optical Boundaries," TSI Quarterly, Vol. VIII, Issue 2, April - June 1982.
27. McLaughlin, D.K., and Tiederman, W.G., "Bias Correction for Individual Realization Laser Anemometry Measurements in Turbulent Flows," Physics of Fluids, Vol. 16, No. 12, p. 2082, 1973.
28. Hecht, E., and Zajac, A., Optics, p. 168, Addison-Wesley, Reading, MA, 1974.
29. McVey, R., "The Design of a Laser Doppler Velocimeter for Use in Studying Turbulent and Mixing Flows," Master's Thesis, Purdue University, 1979.
30. Instruction Manual for TSI Model 1980 Counter, Thermo-Systems Incorporated, St. Paul, Minnesota.
31. Laufer, J., "The Structure of Turbulence in Fully Developed Pipe Flow," NACA Technical Note 2954, June 1953.

LIST OF REFERENCES (cont'd)

32. Logan, S.E., "A Laser Velocimeter for Reynolds Stress and Other Turbulence Parameters," AIAA Journal, Vol. 19, No. 7., pp. 933-935, 1972.
33. Hinze, J.O., Turbulence, McGraw Hill, New York, 1975.
34. Barbin, A.R., and Jones, J.B., "Turbulent Flow in the Inlet Region of a Smooth Pipe," Transactions of the ASME, Series D, Vol. 85, No. 1, pp. 29-34, 1963.
35. Pun, W.M., and Spalding, D.B., "A General Computer Program for Two-Dimensional Elliptic Flows," Imperial College Mechanical Engineering Department Report HTS/76/2.
36. Eaton, J.K., and Johnston, J.P., "Turbulent Flow Reattachment: An Experimental Study of the Flow and Structure Behind Backward-Facing Step," Report MD-39, Mechanical Engineering, Stanford University, 1980.
37. Smyth, R., "Turbulent Flow Over a Plane Symmetric Sudden Expansion," ASME Journal of Fluids Engineering, Vol. 101, pp. 348-353, September 1979.
38. Karpuk, M.E., and Tiederman, W.G., "Effect of Finite Size Probe Volume Upon Laser Doppler Anemometer Measurements," AIAA Journal, Vol. 14, No. 8, pp. 1099-1105, August 1976.
39. Chaturvedi, M.C., "Flow Characteristics at Axisymmetric Expansions," Ph.D. Dissertation, Department of Mechanics & Hydraulics, State University of Iowa, Ames, Iowa, 1962.
40. Taylor, J.R., An Introduction to Error Analysis, University Science Books, Mill Valley, CA, 1982.
41. Yanta, W.J., "The Use of the Laser Doppler Velocimeter in Aerodynamic Facilities," AIAA-80-0435, 1980.

DATE
ILME